



HAL
open science

Mutational analysis to explore long-range allosteric couplings involved in a pentameric channel receptor pre-activation and activation

Solène N. Lefebvre, Antoine Taly, Anaïs Menny, Karima Medjebeur,
Pierre-Jean Corringer

► To cite this version:

Solène N. Lefebvre, Antoine Taly, Anaïs Menny, Karima Medjebeur, Pierre-Jean Corringer. Mutational analysis to explore long-range allosteric couplings involved in a pentameric channel receptor pre-activation and activation. *eLife*, 2021, 10, pp.e60682. 10.7554/eLife.60682 . hal-03369647v1

HAL Id: hal-03369647

<https://hal.sorbonne-universite.fr/hal-03369647v1>

Submitted on 7 Oct 2021 (v1), last revised 9 Dec 2021 (v2)

HAL is a multi-disciplinary open access archive for the deposit and dissemination of scientific research documents, whether they are published or not. The documents may come from teaching and research institutions in France or abroad, or from public or private research centers.

L'archive ouverte pluridisciplinaire **HAL**, est destinée au dépôt et à la diffusion de documents scientifiques de niveau recherche, publiés ou non, émanant des établissements d'enseignement et de recherche français ou étrangers, des laboratoires publics ou privés.



Distributed under a Creative Commons Attribution 4.0 International License

1 **Mutational analysis to explore long-range allosteric couplings involved in a**
2 **pentameric channel receptor pre-activation and activation**

3 Solène N. Lefebvre^{1,2}, Antoine Taly^{3,4*}, Anaïs Menny^{1,2}, Karima Medjebeur¹,
4 Pierre-Jean Corringer^{1*}

5 ¹ Unité Récepteurs-Canaux, Institut Pasteur, UMR 3571, CNRS, 75015 Paris,
6 France

7 ² Sorbonne Université, Collège doctoral, 75005 Paris, France

8 ³ CNRS, Université de Paris, UPR 9080, Laboratoire de Biochimie Théorique,
9 UPR 13 9080, 13 rue Pierre et Marie Curie, F-75005, Paris, France

10 ⁴ Institut de Biologie Physico-Chimique-Fondation Edmond de Rothschild, PSL
11 Research University, Paris, France

12 *Corresponding authors: antoine.taly@ibpc.fr, pjcorrin@pasteur.fr

13 **ABSTRACT**

14 Pentameric ligand-gated ion channels (pLGICs) mediate chemical signaling
15 through a succession of allosteric transitions that are yet not completely
16 understood as intermediate states remain poorly characterized by structural
17 approaches. In a previous study on the prototypic bacterial proton-gated channel
18 GLIC, we generated several fluorescent sensors of the protein conformation that
19 report a fast transition to a pre-active state, which precedes the slower process of
20 activation with pore opening. Here, we explored the phenotype of a series of
21 allosteric mutations, using paralleled steady-state fluorescence and
22 electrophysiological measurements over a broad pH range. Our data, fitted to a 3-
23 states Monod-Wyman-Changeux (MWC) model, show that mutations at the
24 subunit interface in the extracellular domain (ECD) principally alter pre-activation,
25 while mutations in the lower ECD and in the transmembrane domain principally
26 alter activation. We also show that propofol alters both transitions. Data are
27 discussed in the framework of transition pathways generated by normal mode
28 analysis (iModFit) that suggest collective protein motions concerted with pore
29 opening. It further supports that pre-activation involves major quaternary
30 compaction of the ECD, and suggests that activation involves principally a re-
31 organization of a “central gating region” involving a contraction of the ECD β -
32 sandwich and the tilt of the channel lining M2 helix.

33 INTRODUCTION

34 Pentameric ligand gated ion channels (pLGICs) mediate fast synaptic
35 communication in the brain. In mammals, this family includes the excitatory
36 nicotinic acetylcholine (ACh) and serotonin receptors (nAChRs and 5-HT₃Rs) as
37 well as the inhibitory γ -aminobutyric acid (GABA) and glycine receptors (GABA_ARs
38 and GlyRs) (Jaiteh et al., 2016). pLGICs are also present in bacteria, notably with
39 the pH-gated channels GLIC (Bocquet et al., 2007) and sTeLIC (Hu et al., 2018),
40 the GABA-gated channel ELIC (Zimmermann and Dutzler, 2011) and the calcium-
41 modulated DeCLIC (Hu et al., 2020).

42 pLGICs physiological function is mediated by alternating between different
43 allosteric conformations in response to neurotransmitter binding. Initially, a minimal
44 4-states model could describe the main allosteric properties of the muscle-type
45 nAChR (Heidmann and Changeux, 1980; Sakmann et al., 1980). In this model, the
46 ability of ACh binding to activate the nAChR involves a resting- to active-state
47 transition, and prolonged ACh occupancy promotes a biphasic desensitization
48 process. Subsequently, kinetic analysis of the close-to-open transitions recorded
49 by single channel electrophysiology revealed multiple additional states that are
50 required to account for the observed kinetic patterns. For activation, short-lived
51 intermediate “pre-active” states named “flipped” (Lape et al., 2008) and “primed”
52 (Mukhtasimova et al., 2009) were included in the kinetic schemes of the GlyRs
53 and nAChRs, while rate-equilibrium free-energy relationship (REFER) analysis of
54 numerous mutants of the nAChR suggested passage through four brief
55 intermediate states (Gupta et al., 2017). Likewise, analysis of single-channel shut
56 intervals during desensitization are described by the sum of four or five
57 exponential components, suggesting again additional intermediate states (Elenes
58 and Auerbach, 2002). Kinetics data thus show that pLGICs go through complex
59 structural re-organizations in the course of both activation and desensitization.
60 These events are at the heart of the protein’s function, allowing coupling between
61 the neurotransmitter site and the ion channel gate which are separated by a
62 distance of more than 50 Å.

63 The past decade has seen great structural biology efforts to increase our
64 understanding of the molecular mechanisms involved in gating (Nemecz et al.,
65 2016). At least one structure of each major member of prokaryotic (Hilf and
66 Dutzler, 2008; Bocquet et al., 2009; Hu et al., 2018, 2020) and eukaryotic pLGICs

67 (Althoff et al., 2014; Du et al., 2015; Polovinkin et al., 2018; Gharpure et al., 2019;
68 Masiulis et al., 2019) have been resolved by X-ray crystallography or cryo-electron
69 microscopy (cryoEM). They highlight a highly conserved 3D architecture within the
70 family. Each subunit contains a large extracellular domain (ECD) folded in a β -
71 sandwich and a transmembrane domain (TMD) containing four α -helices, with the
72 second M2-helix lining the pore. However, the physiological relevance of these
73 structures or their assignment to particular intermediates or end-states in putative
74 gating pathways remains ambiguous and poorly studied. Conversely, it is possible
75 that intermediate conformations, disfavored by crystal packing lattice or under-
76 represented in receptor populations on cryoEM grids, are missing in the current
77 structural galleries.

78 Understanding the allosteric transitions underlying gating thus requires
79 complementary techniques, where the protein conformation can be followed in
80 near-physiological conditions, i.e. at non-cryogenic temperature on freely moving
81 protein, and over a broad range of ligand concentrations. To this aim, we previous-
82 ly developed the tryptophan/tyrosine induced quenching technique (TrIQ) on GLIC
83 (Menny et al., 2017), a proton-gated channel (Parikh et al., 2011; Laha et al.,
84 2013; Gonzalez-Gutierrez et al., 2017). In this technique, the protein is labeled
85 with a small fluorophore, the bimane, and collisional quenching by a neighboring
86 indole (tryptophan) or phenol (tyrosine) moieties is used to report on changes in
87 distance between two residues within the protein over a short distance range of 5-
88 15 Å (Mansoor et al., 2002, 2010; Jones Brunette and Farrens, 2014). Bimane-
89 quencher pairs on GLIC combined with kinetic analysis allowed us to characterize
90 pre-activation motions occurring early in the conformational pathway of activation
91 (Figure 1A). We found they occur at lower proton concentrations than pore open-
92 ing, and are complete in less than a millisecond, much faster than the rise time of
93 the active population that occurs in the 30-150 millisecond range in electrophysiol-
94 ogy recordings (Laha et al., 2013).

95 Here, to explore the conformational landscape of GLIC during pH-gating,
96 we further exploited the TrIQ approach. We performed electrophysiological and
97 fluorescence quenching experiments on a series of allosteric mutants of GLIC, as
98 well as in the presence of the general anesthetic propofol. We modeled the whole
99 dataset with a 3-states allosteric model comprising a resting, a pre-active and an
100 active state. To help interpreting the fluorescence quenching data into structural

101 terms, we built atomistic models of the various bimane-labeled proteins, and
102 computed their gating transition pathways using iMODfit. Our results indicate that
103 mutations alter the function via distinct mechanisms and differentially displace the
104 allosteric equilibria involved in fluorescence quenching and electrophysiology
105 recordings. It supports that pre-activation involves major quaternary compaction of
106 the ECD, and suggest that activation involves principally a re-organization of a
107 “central gating region” involving a contraction of the ECD β -sandwich and the tilt of
108 the channel lining M2 helix.

109 **RESULTS**

110 **Fluorescence and electrophysiological measurements**

111 **Quenching pairs used in the study**

112 In our previous fluorescence quenching experiments, a bimane fluorophore
113 was introduced on GLIC by covalent labeling on an engineered cysteine, after
114 mutation of the single endogenous cysteine C27S. A Trp or Tyr quenching residue
115 was incorporated when necessary to generate a quenching pair. We created five
116 quenching pairs (Figure 1B): 3 are located across the ECD interface and report on
117 a quaternary compaction following pH drop (Bim136-Q101W, Bim133-L103W and
118 Bim33-W160), one reports on a tertiary reorganization at the top of the ECD
119 (Bim135-W72), and one reports on the outward movement of the M2-M3 loop at
120 the ECD-TMD interface (Bim250-Y197). In the present study, we used the
121 Bim136-Q101W as sensor of the ECD compaction, along with Bim250-Y197 as a
122 sensor of the M2-M3 loop motion. We also investigated in detail Bim135-W72, but
123 the complex results for this pair precluded clear conclusions. The related data are
124 thus presented and discussed in Figure 1-Supplementary 1.

125 To accurately compare mutants, we first measured detailed pH-dependent
126 fluorescence and electrophysiological curves (Figure 1C). Fluorescence was
127 measured in steady-state conditions on detergent (DDM)-purified protein, and
128 normalized to the fluorescence intensity under denaturing conditions (1% SDS), as
129 previously described (Menny et al., 2017). GLIC allosteric transitions are
130 particularly robust in different lipid/detergent conditions (Sauguet et al., 2014;
131 Carswell et al., 2015) and DDM-purified protein yielded similar results to that of
132 azolectin-reconstituted protein (Menny et al., 2017), while allowing better
133 reproducibility. For both sensors, we confirmed that the pH-dependent
134 fluorescence changes are essentially abolished when mutating the quenching

135 partner to phenylalanine, which does not quench bimane fluorescence (Mansoor
136 et al., 2002). We also confirmed that pH-dependent quenching curves for Bim136-
137 Q101W and Bim250-Y197 display higher sensitivity (especially for Bim250-Y197)
138 and lower apparent cooperativity than the pH-dependent activation curves
139 recorded by electrophysiology (Figure 1-Supplementary 2).

140 **The quaternary compaction at the ECD top is strongly allosterically coupled**
141 **with the lower part of the ECD interface**

142 Using the Bim136-Q101W conformational sensor, we first investigated
143 allosteric mutants located at the inter-subunit interface in the lower part of the ECD
144 (Figure 2A). We previously showed that E26Q produces a decrease in pH_{50} for
145 activation (Nemecz et al., 2017), a phenotype which is conserved here on the
146 Bim136-Q101W background (Figure 2B and 2C). The fluorescence quenching
147 curve of Bim136-Q101W-E26Q also shows a decrease in pH_{50} (Figure 2D), and
148 the ΔpH_{50} between Bim136-Q101W and Bim136-Q101W-E26Q are nearly
149 identical in electrophysiology and fluorescence (- 0.59 and - 0.57 respectively;
150 Table 1). Interestingly, the Bim136-Q101W-E26Q fluorescence quenching curve
151 has a remarkable feature as compared to most mutants investigated thereafter: in
152 the pH 7-8 range, where the pH-dependent fluorescence quenching is not yet
153 observed, the fluorescence (F/F_{SDS}) is significantly lower ($F_0 = 0.53$) as compared
154 to the Bim136-Q101W alone ($F_0 = 0.71$). This suggests that substantial quenching
155 is present at neutral pH and that E26Q not only alters the allosteric transition, but
156 also modifies the conformation of the resting state itself which appears to be more
157 compact when the E26Q mutation is present.

158 Another mutation, Y28F, was reported to produce a moderate gain of
159 function on a wild-type background (Nemecz et al., 2017). Surprisingly, mutating
160 Y28F in the Bim136-Q101W (C27S) background yields a drastic loss of function
161 characterized by a slow activating receptor and a marked decrease in pH_{50} (Figure
162 2B and 2C; Table 1). However, mutating back the C27 endogenous cysteine
163 (Bim136-Q101W-Y28F (C27)) reverses the phenotype to that of Bim136-Q101W
164 (C27S) (Figure 2C & Table 1), demonstrating that this loss of function is due to the
165 combination of the C27S and Y28F mutations. In fluorescence, the quenching
166 curve of Bim136-Q101W-Y28F (C27S) also shows a large decrease in pH_{50} ,
167 associated with an apparent higher cooperativity. Again, the ΔpH_{50} are in the same
168 range in fluorescence quenching (-2.2) and in electrophysiology (more than - 1.5,

169 the plateau could not be reached with this mutant preventing accurate
170 measurement of the pH_{50}).

171 In conclusion, the quaternary compaction of the top of the ECD, monitored
172 with the Bim136-Q101W sensor, is strongly coupled in an allosteric manner with
173 the lower part of the ECD interface.

174 **Long-range allosteric coupling between the TMD and the top of the ECD**

175 To investigate whether allosteric coupling occurs with more distant regions
176 of the protein, we selected three loss of function mutations further away from the
177 Bim136-Q101W pair: D32E near the ECD-TMD interface; H235Q in the middle of
178 the TMD and E222Q, at the bottom of the TMD and lining the pore (Figure 3A)
179 (Sauguet et al., 2014; Nemezc et al., 2017).

180 Performing these mutations on the Bim136-Q101W-C27S background
181 shows overall conservation of their previously published phenotype, with a 0.7 unit
182 (D32E and E222Q) and 1.3 unit (H235Q) decreases in the pH_{50} of activation as
183 compared to Bim136-Q101W-C27S (Figure 3B and 3C; Table 1). The
184 fluorescence quenching curves are also shifted to lower pH_{50} s, with ΔpH_{50} s of 0.3-
185 0.5 (D32E and E222Q) and 0.85 (H235Q) (Figure 3D).

186 The quenching data thus reveal an allosteric coupling between both ends of
187 the protein, since the structural perturbations performed around the TMD are
188 transmitted to the top of the ECD, impairing its compaction. However, as opposed
189 to the ECD mutations E26Q and Y28F/C27S, these mutations have a stronger
190 effect on the pH_{50} of the electrophysiological response as compared to
191 fluorescence quenching. It thus suggests that both processes are not fully coupled
192 for mutations further away from the sensor site.

193 **Total loss of function mutations differentially alter ECD and TMD allosteric** 194 **motions**

195 To further explore the allosteric coupling within GLIC, we extended the
196 analysis to mutations known to strongly or completely prohibit channel opening
197 (Figure 4A & 4B). We selected three mutants: H235F, L157A and L246A which
198 show robust surface expression and no substantial current in oocytes (Figure 4C &
199 4-Supplementary 1). For those mutants, in addition to electrophysiological
200 recordings, and fluorescence quenching measurements on Bim136-Q101W and
201 Bim135-W72 (Figure 4D and Figure 1-Supplementary 1), we also monitored the
202 motion of the M2-M3 loop with Bim250-Y197 (Figure 4E).

203 Mutants L157A and L246A reveal unique quenching phenotypes. Combined
204 with Bim136-Q101W, they both show a pH-dependent quenching of fluorescence
205 with a decreased amplitude (ΔF_{\max}) associated with a significant decrease in pH_{50}
206 as compared to the Bim136-Q101W background (Table 1). In contrast, they only
207 weakly alter the motions at Bim250, which occur with a complete amplitude and
208 small changes in pH_{50} . The mutation H235F leads to a phenotype opposite to that
209 of L157A or L246A. Its Bim136-Q101W pH-dependent curve shows a nearly full
210 quenching amplitude together with a decrease in pH_{50} , while it impairs the motion
211 of the M2-M3 loop, with only a partial pH-dependent de-quenching at Bim250-
212 Y197.

213 Thus, while those mutants do not have a measurable access to the active
214 state, they still show allosteric motions as revealed by fluorescence. Unlike the
215 moderate loss of function mutants investigated above, these mutations alter the
216 amplitude of the fluorescence curves, revealing profound changes of either the
217 protein conformations and/or allosteric equilibria.

218 **Long-range allosteric coupling between the ECD top and propofol**

219 We further used the TrIQ technique to study the mechanism of action of the
220 general anesthetic propofol, an allosteric modulator of GLIC. Propofol binds to at
221 least three main sites within the TMD: one site in the pore itself near the middle of
222 the TMD, and two sites in the upper part of the TMD at intra- or inter-subunit
223 locations (Figure 5A). Propofol is an inhibitor of GLIC, but it has been shown to be
224 a potentiator of the H235Q mutant (Fourati et al., 2018). We verified that these
225 effects are conserved in the Bim136-Q101W background, with propofol decreasing
226 the pH_{50} of activation of Bim136-Q101W while increasing the pH_{50} of Bim136-
227 Q101W-H235Q (Figure 5B and C; Table 1). Fluorescence quenching experiments
228 essentially parallel the electrophysiological data. Addition of 100 μM propofol on
229 Bim136-Q101W decreases the fluorescence pH_{50} by half a unit, while it increases
230 that of Bim136-Q101W-H235Q by more than half a unit (Figure 5D). Interestingly,
231 a similar pattern is seen on sensor Bim135-W72 (Figure 1-Supplementary 1). Our
232 data thus shows that propofol does act on the global allosteric transitions by
233 displacing the equilibria of both pre-activation and activation. It is noteworthy that
234 propofol is also likely to generate local effects upon binding to modulate the
235 function, which are not investigated here. For instance, its binding into the pore
236 may sterically block ion translocation to produce inhibition (Fourati et al., 2018).

237 **Fit of the data with a 3-states MWC model**

238 To characterize the effect of mutations in a more quantitative manner, we
239 fitted the whole dataset with a Monod-Wyman-Changeux (MWC) model. Since the
240 fluorescence and electrophysiological pH-dependent curves presented here
241 underlie two major allosteric steps, pre-activation (a fast process causing the
242 changes in fluorescence as previously identified in stopped flow experiments
243 (Menny et al., 2017)) and activation (a slower process responsible for channel
244 opening), we used a 3-states model where the protein is in equilibrium between a
245 resting R state, a pre-active pA state and an active A state. Changes in
246 fluorescence, although measured here in equilibrium conditions, actually occur
247 with fast kinetics and are likely not related to desensitization. For the measure of
248 activation, we used peak currents recorded in oocytes, assuming that
249 desensitization would be negligible in these conditions. The putative slow-
250 desensitized state of GLIC was thus not included in this model.

251 In our allosteric model, we first defined a single proton binding site present
252 in five copies with intrinsic affinities for each state named K_R , K_{pA} and K_A . The
253 equilibria between the states at pH 7 are governed by isomerization constants L_{pA}
254 $= \bar{R}/\overline{pA}$ and $L_A = \overline{pA}/\bar{A}$ (see material and methods for detailed equations). For each
255 fluorescent sensor (Bim136-Q101W and Bim250-Y197), each allosteric state has
256 a defined fluorescence intensity F_R , F_{pA} and F_A . As the model involves numerous
257 parameters that cannot be fitted simultaneously given the available data, we
258 adopted a stepwise strategy (summarized in Figure 6- Supplementary 1). We
259 formulated several reasonable hypotheses to fit some parameters to the
260 experimental data which were kept fixed while others were constrained to change
261 together:

262 1/ since the changes in fluorescence occur mainly during pre-activation (Menny et
263 al., 2017), we infer that both sensors display identical fluorescence intensity in the
264 pA and A states ($F_{pA} = F_A$).

265 2/ a majority of the allosteric mutants followed with the Bim136-Q101W sensor
266 have almost identical fluorescence values at both ends of the pH curves. This
267 suggests that allosteric transitions at low and high pHs are complete and that at
268 pH 7 a majority of proteins are in the R state ($\bar{R} \approx 1$, \bar{R} representing the fraction of

269 proteins in the R state) while conversely at pH 4 $\overline{pA} + \overline{A} \approx 1$. Consequently, for the
270 Bim136-Q101W sensor, $F_{pH7} = F_R$ and $F_{pH4} = F_{pA} = F_A$.
271 3/ the mutations alter the allosteric isomerization constant between states but not
272 the intrinsic affinities for protons.

273 **Setting the pre-activation parameters using total loss of function mutants**

274 We started the fitting procedure with the total loss of function mutants,
275 which do not have access to the A state, and simplify the model to one with two
276 states (R and pA). We note that these mutants producing drastic phenotypes,
277 could profoundly alter the protein conformations, possibly including that of the R
278 and pA states and their intrinsic fluorescence. However, the H235F mutant has
279 been shown by X-ray crystallography to adopt a well folded conformation,
280 captured in the crystal in a “Locally-closed” conformation corresponding to an
281 active-like ECD and resting-like TMD conformation (Prevost et al., 2012, 2013)
282 from which we infer that the fluorescence from this mutant reports on WT-like
283 motions.

284 Fitting of the Bim136-Q101W-H235F curves is constrained by two
285 experimental values (pH_{50} and F_{max}) with three variable parameters, K_R , K_{pA} and
286 L_{pA} . In consequence, for each value of L_{pA} , the two other parameters are fully
287 constrained by the experimental data. As an illustration, we fixed $L_{pA} = 100$. After
288 manual fitting of the curves, we were able to extract $K_R = 3.6 \cdot 10^{-6}$ and $K_{pA} = 1.0 \cdot 10^{-6}$.
289 We then used these K_R and K_{pA} values to fit the fluorescence quenching curves
290 of Bim250-Y197-H235F, and sensors Bim136-Q101W and Bim250-Y197, only
291 adjusting L_{pA} (Figure 6-Supplementary 2). The model thus provides a minimal set
292 of parameters accounting for the pH_{50} s and absolute fluorescence changes of
293 these four constructs. It notably suggests that H235F causes a marked
294 stabilization of the R state over the pA state (increase in L_{pA}).

295 **Setting the activation parameters**

296 In a second step, we added the activation state in the MWC model and
297 sought to fit the pH-dependent electrophysiological response curves. Keeping the
298 pre-activation parameters defined above, we found that a 3-states model
299 comprising a single proton site could not account for the separation between the
300 fluorescence and electrophysiological curves. With a unique proton site, the model
301 doesn't allow for more than a 5-fold difference, between the curves, when in our
302 experimental data Bim250-Y197, pH_{50} s are respectively 5.83 and 4.66, more than

303 one order of magnitude difference. To fit the activation curves, we thus added a
304 second proton site (named primed, present in 5 copies), that specifically drives the
305 activation step ($K_{R'} = K_{pA'}$, $K_{pA'} > K_{A'}$), while the first proton site specifically drives
306 the pre-activation step ($K_R > K_{pA}$, $K_{pA} = K_A$). This model is reasonable since it is
307 established that several proton sites are contributing to GLIC activation (Nemecz
308 et al., 2017). Using this 3-states 2-sites model, we found a set of parameters
309 accounting for the pH-dependent curves of the sensors (Figure 6A). With the
310 Bim136-Q101W sensor (Figure 6C), variations in the first half of the fluorescence
311 curve results from the apparition of the pA state which is maximally populated (\overline{pA}
312 around 0.5) near the pH_{50} of the fluorescence curve. At lower pHs, the equilibria
313 are further displaced toward the A state, contributing to the decrease in
314 fluorescence in the second half of the curve, and to the parallel apparition of
315 current. With the Bim250-Y197 sensor (Figure 7), the mutation introduced causes
316 a destabilization of the A state over the pA state (increase in L_A), displacing the
317 pH-dependent activation curve to lower pHs. The pH-dependent fluorescence
318 curve is consequently mainly caused by the apparition of the pA state with a
319 maximal \overline{pA} value reaching more than 0.8.

320 It should be noted that while the pre-activation parameters are substantially
321 constrained by the experimental data (relying only on the assumption that $L_{pA} =$
322 100 for the H235F mutant), the activation parameters were chosen arbitrarily and
323 other combinations of affinity and isomerization constants could also fit the data. In
324 addition, the dataset itself is heterogeneous since fluorescence experiments were
325 performed on purified receptors, while electrophysiology was done on *Xenopus*
326 oocytes. Therefore, the activation parameters used here are only meant to
327 evaluate, as a proxy, the relative effect of each mutation on the activation
328 transition.

329 **Differential effects of GLIC mutants on pre-activation versus activation**

330 Based on the sensors' parameters, we fitted the various mutants by
331 adjusting the isomerization constants of pre-activation and activation (Figure 6 &
332 7). Overall, reasonable fits can be achieved in most cases. Variations in
333 isomerization constants between mutant and parent sensors were calculated as
334 multiplication factors for pre-activation and activation (L_{mutant}/L_{sensor} , Figure 6B &
335 7A). In parallel, we performed the whole set of fits with different starting values of

336 the H235F L_{pA} constants (1000 and 100,000), yielding different sets of
337 isomerization constants but in each case similar effects of the mutants (Figure 6-
338 Source data 1, all values presented below were taken from the $L_{pA} = 100$ fit unless
339 indicated otherwise). A discrepancy between data points and fits is however
340 consistently observed concerning the apparent cooperativity of most pH-
341 dependent fluorescence curves. The pH-dependent decreases in fluorescence
342 observed experimentally arise over a relatively large range of pHs, while
343 theoretical curves display sharper shapes. It is possible that the pre-activation
344 transition, modeled here by a single allosteric step, might actually involve multiple
345 steps that are not implemented here. Despite this limitation, the model allows us to
346 highlight clear-cut effects.

347 Experimentally, the most phenotypically striking mutant is Y28F, which
348 produces a two orders of magnitude shift of the pH-dependent curves, and a near
349 equalization of fluorescence and electrophysiological pH_{50s} . Y28F is readily fitted
350 by the simple assumption that the R-pA equilibrium is strongly displaced toward
351 the R state, i.e. that the R state is thermodynamically stabilized over both the pA
352 and A states, with no changes in the pA to A equilibrium. In this condition, the
353 fluorescent changes are entirely caused by the apparition of the active state, and
354 the fraction of receptors in the pA state, in these equilibrium conditions, remains
355 below 0.1% at every pH. This does not mean that this mutant does not populate
356 the pA state during activation, since the pA state may be kinetically favored and
357 actually appear in a transient manner. Mutant E26Q has a milder phenotype, but
358 its fitting also suggests it has a stronger effect on pre-activation than on activation
359 (multiplication factors of isomerization constants of 15 for pre-activation and 10 for
360 activation, Figure 6B).

361 In contrast, mutants in the lower ECD (D32E), or in the TMD (H235Q and
362 E222Q), are found to preferentially alter the activation transition, destabilizing the
363 A over the pA state, with small effects on pre-activation (multiplication factor of
364 isomerization constants for pre-activation: 2, 1.5 and 7 and for activation: 80, 40
365 and 700 respectively). In consequence, they show a large displacement of the
366 activation curve than that of the fluorescence curve when compared to the parent
367 sensor (Figure 6). On the Bim136-Q101W sensor and H235Q mutant, propofol
368 acts respectively as a negative and positive allosteric modulator (Fourati et al.,

369 2018). For both constructs, propofol is found to have a dual effect, altering
370 principally the activation transition but also the pre-activation transition.

371 Finally, for total loss of function mutants, while H235F fluorescence quench-
372 ing could be fitted reasonably well with a 2-states R-pA model (Figure 7 and 6-
373 Source data 1), the best fits of L157A and L246A were of lower quality. In particu-
374 lar, pH-dependent curves of Bim136-Q101W-L157A and Bim136-Q101W-L246A
375 are rather flat, the former being better represented by a straight line. The tentative
376 fits are thus not satisfactory, suggesting that these mutants display complex phe-
377 notypes, plausibly driving the conformations into states that are not implemented
378 in our model.

379 **Investigation of quenching pairs reorganizations using iMODfit and bimane** 380 **docking**

381 In our previous study, the various quenching pairs were designed on the
382 basis of the comparison of the X-ray structures of GLIC solved at pH 7 and pH 4,
383 selecting pairs of residues which undergo large changes in backbone C_{α} distanc-
384 es. GLIC-pH 7 is in a non-conductive conformation with a closed hydrophobic gate
385 in the upper part of the pore, consistent with a resting-like state. The GLIC-pH 4
386 structure shows in contrast an open gate compatible with a conductive conform-
387 ation (Cheng et al., 2010; Fritsch et al., 2011; Sauguet et al., 2013; Gonzalez-
388 Gutierrez et al., 2017) consistent with an active-like structure.

389 However, the orientation of bimane fluorophore and the surrounding resi-
390 dues including the main quencher is not known for Bim136-Q101W and B250-
391 Y197. Their distances should be taken into consideration to propose a more faith-
392 ful picture of the underlying molecular reorganizations. In addition, comparison of
393 crystallographic structures alone does not inform us one the time course of the
394 quenching process during the movement. For instance, at Bim136-Q101W and
395 Bim250-Y197, relatively large changes in C_{α} distance (2 to 5 Å) are observed be-
396 tween GLIC-pH 7 and GLIC-pH 4, but one can ask how the distances (and
397 quenching) evolve during these movements.

398 To investigate these issues, we computed approximate trajectories between
399 the two states using iMODfit, and then modeled on them the bimane/quencher pair
400 using a simple docking approach. iMODfit has been originally designed to fit struc-
401 tures inside electron-microscopy envelopes, notably from a very different starting
402 conformation (López-Blanco and Chacón, 2013). This flexible fitting is made via

403 the deformation of the structure using normal mode analysis (NMA) (see method
404 section). NMA approximates the surface of the conformational landscape and de-
405 composes the movements into discrete modes. It takes advantage of a simplified
406 but physically meaningful representation of the interaction between the atoms,
407 based on simple springs connecting close pairs of atoms in the native structure.
408 This method provides a time-independent equation and allows the study of slow
409 (biologically relevant) and collective conformational transitions. NMA has been
410 shown previously to allow the study of pLGIC gating mechanisms (Taly et al.,
411 2005; Bahar et al., 2010). In addition, we have shown on NMDA receptors that
412 iMODfit's NMA-based fitting process can actually visit biologically-relevant inter-
413 mediate structures (Esmenjaud et al., 2019). The aim of this study is therefore not
414 to capture the fine details of the transition pathway, but to generate plausible tra-
415 jectories capturing the main features of the conformational reorganization.

416 **Generation of two distinct conformational pathways using iMODfit**

417 Two independent trajectories were computed. Trajectory A (12 frames)
418 starts from the closed GLIC-pH 7 structure to reach the open GLIC-pH 4 structure,
419 and trajectory B (11 frames) starts from the GLIC-pH 4 structure to reach the
420 GLIC-pH 7 structure. Both trajectories are fully reversible and are equally relevant
421 to describe either activation or deactivation, since normal modes deformation can
422 be applied in the two directions. RMSD analysis between each frame and the
423 reference structure indicates gradual re-organization of GLIC across the length of
424 both simulations (Figure 8A). Both trajectories, when visualized from the resting to
425 active state, show three major re-organizations components: a quaternary twist of
426 the pentamer, a "central gating re-organization" comprising opening/closure of the
427 pore, and a quaternary compaction of the ECD.

428 In trajectory A, the twist motion occurs in the first half of the trajectory
429 (Figure 8B). This motion describes opposite rotations between ECD and TMD
430 domains, as measured by the twist angle defined by center of mass vectors of the
431 ECD and TMD (Taly et al., 2005; Calimet et al., 2013). The pore re-organization
432 happens in the second half of the trajectory and leads to the opening of its upper
433 part which contains the activation gate, as measured at Ile233 C α (also named I9';
434 Figure 9A & 9B). This motion is associated with a central gating re-organization of
435 the GLIC structure involving: 1/ a tilt of M2 toward M3 (as measured by a decrease
436 in distance between His235 nitrogen and the carbonyl backbone of Ile259; Figure

437 9A & 9C), 2/ an outward motion of the M2-M3 loop (measured as an increase in
438 distance between Pro250 C α and the phenolic oxygen of Tyr197; Figure 9A & 9D),
439 and 3/ a contraction of the β -sandwich at the bottom of the ECD (measured as a
440 decrease in distance between C α of residues Asp32 and Gly159; Figure 10A &
441 10D). In addition to these two consecutive global motions, the progressive
442 quaternary compaction of the ECD, another crucial landmark of GLIC
443 reorganization, occurs throughout the trajectory. This compaction is quantified
444 through measurement of inter-subunit distances at the top ECD (between C β
445 Asp136/Gln101 and Arg133/Leu103; Figure 10A, 10B, 10C & 10-Supplementary
446 1), and the bottom ECD (measured by a decrease in the inter-subunit distance of
447 C β Lys33/Trp160, Figure 10-Supplementary 2), indicating a progressive decrease
448 in distance throughout the frames. It is noteworthy that these inter-subunit
449 distances are highly variable, due to the asymmetric nature of the ECDs of the
450 GLIC-pH 7 structure, where each subunit β -sandwich presents a unique
451 orientation as well as relatively high B-factors (Sauguet et al., 2014). This
452 variability decreases over the frames to reach the structure of GLIC-pH 4 which is
453 compact and essentially symmetric.

454 Trajectory B shows substantially the same components but with an inverted
455 sequence of events. The central gating re-organization starts first and is
456 associated with an increase in pore radius at Ile233, followed by the twist motion in
457 the second half of the trajectory, the latter being associated with further
458 fluctuations of the pore radius. The ECD compaction is also spread over the whole
459 trajectory. In conclusion, using iMODfit we could generate two distinct trajectories
460 that are in principle equally plausible to describe a gating transition of GLIC
461 activation or deactivation.

462 **Visualization of quenching pairs on iMODfit trajectories**

463 To relate the conformational reorganizations of GLIC to our fluorescence
464 quenching data, we modeled the fluorophore/quenching pairs in both trajectories.
465 To this aim, the cysteine and quencher mutations were modeled and the bimeane
466 moiety was docked into each frame while keeping it at a covalent-bond compatible
467 distance to the sulfur atom of the cysteine. The distance between bimeane centers
468 of mass and their quenching indole/phenol moieties was then measured in each
469 frame to follow its evolution throughout the trajectories.

470 For Bim136-Q101W, the procedure shows that Bim136 and the Trp101
471 indole ring are separated in the resting-like state (first frame of both trajectories),
472 and are in close contact in the active-like state (last frames of both trajectories)
473 (Figure 10A). These observations are in good agreement with fluorescence data
474 that show a decrease in fluorescence intensity upon pH drop reporting a
475 decreased distance within the pair. The A trajectory shows a progressive decrease
476 in distance that parallels the ECD quaternary compaction movement (C_{β}
477 Asp136/Gln101). The B trajectory shows a different pattern, characterized by
478 important fluctuations followed by a sharper distance decrease only in the last
479 frames (Figure 10C).

480 For the ECD-TMD interface quenching pair Bim250-Y197, the procedure
481 shows that Bim250 is in close contact with the Tyr197 phenol ring in the resting-
482 like state, while both moieties are separated in the active-like state, the bimeane
483 moiety moving on the other side of loop 2 (Figure 9A). This is also in agreement
484 with the fluorescence data that showed an increase in fluorescence upon pH-drop
485 indicating that the Bim250 is moving away from its quencher Tyr197. Interestingly,
486 both A and B trajectories show an abrupt change in Bim250-Y197 distances,
487 corresponding respectively to a late versus early separation, and these changes
488 occur during the outward motion of the M2-M3 loop ($P250_{C\alpha}/Y197_O$ distance;
489 Figure 9D).

490 In conclusion, visualizing the quenching pairs using a simple docking pro-
491 cedure shows good agreement with fluorescence. At position P250, data also
492 show a clear switch of bimeane from one side of loop 2 to the other during the
493 quenching/dequenching process.

494 **DISCUSSION**

495 **Long-range allosteric coupling associated with pre-activation and pore-** 496 **opening processes.**

497 In this study, we revisited several fluorescent sensors by performing
498 detailed pH-dependent quenching curves and parallel iMODfit/docking
499 calculations. Our data clearly support that Bim136-Q101W and Bim250-Y197
500 sensors are *bona fide* reporters of the ECD compaction and the outward M2-M3
501 motion, respectively. In contrast, data related to the Bim135-W72 sensor
502 (presented and discussed in Figure 1-Supplementary 1 and Figure 10-
503 Supplementary 3) show complex patterns of quenching in both *in silico* and

504 fluorescence experiments. We infer that, because of the buried location of Bim135
505 within the protein, it is sensitive to subtle structural re-organizations, the
506 complexity of which precludes clear conclusions. This emphasizes that the
507 fluorescence quenching approach requires screening of multiple positions to select
508 the ones reporting on well-defined local motions.

509 Using these appropriate sensors, we found that a series of five loss-of-
510 function mutations, which shift the pH-dependent electrophysiological curves to
511 higher concentrations, also shift the pH-dependent fluorescence quenching curve
512 of ECD-compaction at the extracellular top of the protein. The ECD-compaction is
513 thus sensitive to mutations scattered along the protein structure down to the
514 opposite cytoplasmic end, indicating substantial allosteric coupling. Since the
515 conformational motions followed by fluorescence occur early in the pathway of
516 activation, it is expected that a shift in the fluorescence curve will be reflected by a
517 parallel shift in the electrophysiological curve. Mutations in the ECD E26Q and
518 Y28F/C27S both present such a phenotype with similar ΔpH_{50} in electrophysiology
519 and fluorescence, suggesting that those mutations would mainly impact the pre-
520 activation transition. In contrast, D32E, E222Q and H235Q lead to a stronger pH_{50}
521 shift in electrophysiology than in fluorescence suggesting that these mutations
522 would alter not only the pre-activation, but also the downstream pore-opening
523 transitions leading to an additive effect on the pH_{50} .

524 **Discriminating pre-activation versus activation phenotypes through** 525 **allosteric modeling**

526 To interpret the mutant phenotypes in a more quantitative manner, we fitted
527 the whole series of data using a 3-states 2-sites model. We had to implement two
528 proton binding sites to account for the separation of the fluorescence and
529 electrophysiological curves of most constructs. This idea is supported by a
530 mutational analysis that showed that several proton activation sites, located at
531 multiple loci, contribute to activation (Nemecz et al., 2017). In addition, chimeric
532 receptors made up of the GLIC_{ECD} fused to the TMDs of various pLGICs (Duret et
533 al., 2011; Ghosh et al., 2017; Laverty et al., 2017) or of the ELIC_{ECD} fused to the
534 GLIC_{TMD} (Schmandt et al., 2015) all preserve a proton-gated ion channel function,
535 with the $\text{GLIC}_{\text{ECD}}\text{-GABA}_{\text{pTMD}}$ chimera showing a markedly biphasic pH-dependent
536 activation curve (Ghosh et al., 2017). This suggests that the proton activation
537 sites, whose loci are not known, are scattered throughout the GLIC structure, in

538 both the ECD and the TMD. In our model, we arbitrarily tuned the affinity constants
539 of site 1 to drive the pre-activation transition, and of site 2 to drive the activation
540 transition, to minimize the number of parameters involved.

541 We also postulated that the various mutants only alter the isomerization
542 constants between states. However, the dataset does not allow for the
543 discrimination between effect on binding affinity versus isomerization constants.
544 The effects of mutations on the isomerization constants are thus used here to
545 evaluate the global effect of the mutations on pre-activation versus activation, but
546 it is possible that they actually report on alteration of isomerization constants,
547 affinity constants, or both. Among the various mutations investigated here, E26Q,
548 E222Q, H235F/Q neutralize the charge of titratable amino acids. It is thus possible
549 that in these cases the mutation eliminates a proton binding site. However, a local
550 impact of a mutation on a proton binding site, or on a set of inter-residues
551 interactions altering the allosteric equilibria, will be equally valid in assigning local
552 structural alterations to pre-active/active phenotypes.

553 The pattern of effect on L_{pA} versus L_A among the various mutants allows us
554 to dissect their allosteric impact. As anticipated from measured ΔpH_{50} , the fits
555 illustrate that Y28F and E26Q principally alter the pre-activation transition and that
556 Bim250, D32E, H235Q and E222Q principally alter the activation transition, while
557 propofol alters similarly both processes (Figure 11). Concerning the total loss of
558 function mutants, we found that they do preserve pre-activation-like allosteric
559 motions, although with an impaired sensitivity and amplitude of the fluorescence
560 curves. H235F is acceptably fitted according to a R-pA model, suggesting that this
561 mutant isomerizes to a pre-active-like state but cannot isomerize further to the
562 active state. L257A and L246A show a more complex phenotype, but fluorescence
563 data show at least partial pre-active-like motions.

564 **Structural reorganizations associated with pre-activation versus activation**

565 Comparison of the GLIC-pH 7 and GLIC-pH 4 X-ray structure highlighted
566 key reorganizations involved in gating (Sauguet et al., 2014), notably a quaternary
567 compaction of the ECD, a tertiary compaction of the β -sandwich in the lower part
568 of the ECD, an outward motion of the M2-M3 loop, and a tilt of the M2 helix toward
569 the M3 helix. Our combined electrophysiological and fluorescence study untangles
570 evaluating the contribution of these specific motions to the pre-activation versus
571 activation transitions.

572 The ECD quenching pairs at Bim136, Bim133 and Bim33 already showed
573 that pre-activation involves a major quaternary compaction of the whole ECD. We
574 strengthen further this idea further by showing that E26Q and Y28F/C27S, that are
575 also located at the subunit interface in the lower part of the ECD, strongly impair
576 the pre-activation process with weaker effects on activation. In addition, the
577 quenching pair at Bim250 showed that the pre-activation involved a key outward
578 movement of the M2-M3 loop. Our data indicate that pre-activation also includes
579 motions of the TMD, since mutation H235Q, as well as propofol binding, are
580 shown to significantly alter pre-activation.

581 For the activation, our mutational analysis points to a key role of the lower
582 inner part of the ECD β -sandwich (D32E), the M2-M3 loop (P250Bim) and the
583 TMD (H235F/Q and E222Q). Interestingly, D32E is involved in strong interactions
584 between sheets in the lower part of the β -sandwich though a salt bridge with R192
585 (Figure 3A). Mutations D32E, elongating the side chain by one carbon atom is thus
586 predicted to disfavor the β -sandwich compaction. In addition, at the middle of the
587 TMD, H235 from M2 interacts with the main-chain carbonyl of I259 from M3
588 through an H-bond favoring the interaction between both helices (Prevost et al.,
589 2012; Rienzo et al., 2014) (Figure 3A). Its mutation into Q and F is predicted to
590 weaken or abolish this interaction and disfavor the tilt of M2 toward M3. This
591 assumption is consistent with the X-ray structure of the H235F and H235Q
592 mutants which shows a “locally closed conformation” where M2 and M3 are
593 separated (Prevost et al., 2012; Fourati et al., 2018). Our data thus provide
594 evidence that the compaction of the β -sandwich and the tilt of M2 are principally
595 involved in the activation process.

596 The mutational analysis also shows for most mutations mixed effects on the
597 isomerization constants of activation and pre-activation, suggesting that both
598 processes involve overlapping regions. The Bim250 position is noteworthy in this
599 respect, since the bimane, reporting an outward motion of the M2-M3 loop,
600 monitors pre-activation, while the modification itself (P250C mutation plus reaction
601 with bimane) principally alters the activation process. It is thus plausible that the
602 M2-M3 loop could move in two successive steps, a first one during pre-activation
603 conditioning dequenching and a second one during activation. In either case, our
604 data further highlight a central role for this loop in ECD-TMD coupling.

605 **Speculative interpretation of the mutant phenotypes in the context of**
606 **computational trajectories**

607 The transition pathway of GLIC has been previously studied by atomic-level
608 molecular dynamics simulations in an explicit membrane environment. While the
609 timescale of the transition greatly exceeds that of even the longest possible
610 simulations, two studies addressed this issue. The first one started from the GLIC-
611 pH 4 structure and instantly set it to neutral pH, followed by a 1 μ s simulation
612 (Nury et al., 2010), yielding concomitant closing of the pore and twist of the whole
613 structure. The second one is based on the string method, using the “swarms of
614 trajectories” approach, computing a trajectory between GLIC-pH 7 and GLIC-pH 4
615 (Lev et al., 2017). The trajectory shows a sequence of events starting from the
616 closed to the open conformation. A first major reorganization involves the opening
617 of the pore, its hydration, and the compaction of the lower part of the ECD β -
618 sandwich. This is followed by a major reorganization of the ECD, notably its twist
619 and its quaternary compaction. This sequence of events appears hardly
620 compatible with our quenching data, although a comprehensive integration of both
621 sets of data would require extensive *in silico* investigations of the bimane-labeled
622 mutants to analyze the reorganizations of the quenching pairs. Of note, an
623 important limitation of the method is that it implicitly postulates the occurrence of a
624 single trajectory. However, a coarse-grained simulation (hybrid elastic-network
625 Brownian dynamics) predicted two possible pathways for GLIC gating, that are
626 characterized by different compactions of the ECD (Orellana et al., 2016).

627 In this paper, we performed iMODfit/bimane docking calculations and
628 generated two distinct trajectories with an inverted sequence of events. While
629 these trajectories are coarse and do not implement fine atomistic interactions, they
630 allow the visualization of plausible collective motions in relation with the
631 reorganization of the quenching pairs.

632 Remarkably, both trajectories show complex quaternary asymmetric re-
633 organizations of ECD compaction. As stated above, ECD compaction is critically
634 involved in pre-activation, a feature consistent with recent work by electron
635 paramagnetic resonance (EPR) spectroscopy (Tiwari et al., 2020) showing a
636 proton-induced inward tilting motion of the ECDs, and recent cryoEM work
637 showing marked structural flexibility of the ECD in the closed-channel state at pH 7
638 (Rovsnik et al., 2021). Interestingly, fluorescence curves of pre-activation,

639 especially the one of Bim136-Q101W, are endowed with markedly low
640 cooperativities. We thus speculate that this low cooperativity might arise from the
641 contribution of multiple asymmetric intermediate states to the transition, in a
642 manner reminiscent of the asymmetric motions recently described for the
643 desensitization of the GABA_A receptor (Gielen et al., 2020).

644 In addition, both trajectories show a “central gating motion” involving
645 several key concerted re-organizations: a compaction of the lower part of the β -
646 sandwich, an outward movement of the M2-M3 loop, as well as a tilt of the M2
647 helix toward M3, that involves a marked increase in the opening of the pore.
648 Similar structural couplings are also observed in string simulations (Lev et al.,
649 2017). This observation nicely parallels our finding that these motions are
650 principally involved in activation. We can thus speculate that the central gating
651 motion constitutes the heart of the activation transition.

652 Concerning the order in which reorganizations are observed, Trajectory A is
653 a better fit to the fluorescence data. It suggests a scenario involving, during pre-
654 activation, progressive ECD compaction and beginning of the M2-M3 loop motion,
655 generating the fluorescence variations. Then the M2-M3 loop completes its
656 movement in concert with β -sandwich compaction and pore opening. Future
657 computational studies are needed to explore this possibility.

658 **Consequences on the gating mechanism within the pLGIC family**

659 The conservation of the general gating mechanism between bacterial and
660 eukaryotic pLGICs is well documented by the available structures with the
661 common allosteric regulatory sites for ligands and mutations (Sauguet et al., 2015;
662 Bertozzi et al., 2016; Rienzo et al., 2016), together with the allosteric compatibility
663 between eukaryotic and prokaryotic ECD/TMD domains to form functional
664 chimeras (Duret et al., 2011; Moraga-Cid et al., 2015; Laverty et al., 2017). It is
665 therefore tempting to speculate that the pre-activation transition of GLIC that we
666 characterize here might have counterparts in human neurotransmitter-gated
667 receptors. In this line, some recent structures of eukaryotic receptors including the
668 5-HT₃R (Polovinkin et al., 2018), the GABA_AR (Masiulis et al., 2019) and the GlyR
669 (Yu et al., 2021) show pre-active-like conformations characterized by marked
670 agonist-elicited re-organization of the ECD but a closed channel at the TMD.
671 Additionally, the flipped or primed states, where the conformational change of the
672 orthosteric site is predicted to be complete, but where the channel is closed, would

673 fit the functional requirement of a pre-active state (Lape et al., 2008; Plested,
674 2014).

675 Our work also investigates the mechanism of action of allosteric mutations
676 by measuring their effects at different levels of the protein, dissecting their
677 phenotype along the gating pathway (Galzi et al., 1996). Allosteric mutations of
678 neurotransmitter-gated receptors, causing congenital pathologies including
679 myasthenia and hyperekplexia have been extensively studied (Taly and
680 Changeux, 2008; Bode and Lynch, 2014; Hernandez and Macdonald, 2019). Most
681 of the hot spots mutated here on GLIC were found associated with pathologies on
682 human receptors. In particular, the lower part of the ECD-ECD interface is the site
683 of a *de novo* S76R mutation in GABA_A α 1 (homologous to Glu26) causing epilepsy
684 (Johannesen et al., 2016) and the mutation L42P in the nAChR δ (homologous to
685 Cys27) causing myasthenia (Shen et al., 2008). This latter mutation (as well as
686 mutation of N41, homologous to E26) decreases activation kinetics and this
687 residue was shown to be energetically coupled to Y127 on the other side of the
688 interface. Interestingly, equivalent residues in GLIC (C27; E26 and Y111) are part
689 of a water network at the bottom of the ECD (Figure 2A). Another noteworthy
690 example is the mutation P250T in GlyR α 1 that causes hyperekplexia (Saul et al.,
691 1999) and which is homologous to E222 in GLIC. Interestingly, on the glycine
692 receptor α 1, other mutations have been studied by single channel recordings and
693 are described to affect principally a flip pre-activation-like step for A52S in the loop
694 2 at the ECD-ECD interface (Plested et al., 2007) or gating for K276E on the M2-
695 M3 loop (Lape et al., 2012). These data suggest that mutations produce similar
696 allosteric perturbations on GLIC and GlyR in those regions.

697 Our work on GLIC provides general mechanisms of how mutations affect
698 pLGICs transitions and further documents conformational changes, beyond
699 information provided by structures. Further work, for example by voltage-clamp
700 fluorometry, would be required to challenge such mechanisms in the context of
701 congenital pathologies on neurotransmitter receptors.

702

703 **MATERIAL AND METHODS****Key Resources Table**

Reagent type (species) or resource	Designation	Source or reference	Identifiers	Additional information
Gene (<i>G. violaceus</i>)	<i>glvI</i> , GLIC	UniProt	Q7NDN8	
Strain, strain background (<i>Escherichia coli</i>)	BL21(DE3) C43	Sigma Aldrich	CMC0019	Chemically competent cells
Biological sample (<i>X. laevis</i>)	Xenopus oocytes	Centre de Ressources Biologiques Xénopes (Rennes-France) and Ecocyte Bioscience (Dortmund-Germany)		
Antibody	Anti-HA Tag (rabbit)	Euromedex	HA-1A1-20uL	(1:200)
Antibody	Anti-rabbit – AlexaFluor645 (goat)	Molecular probes	A21246	(1:1000)
Recombinant DNA reagent	Pet20b-MBP-GLIC	Bocquet et al, 2007		
Recombinant DNA reagent	pMT3-GLIC-HAtag	Nury et al, 2011		
Recombinant DNA reagent	Pmt3-GFP	Nury et al, 2011		
Chemical compound, drug	Monobromo-Bimane	Thermofischer	M1378	
Chemical compound, drug	Bunte salt Bimane	Menny et al, 2017		
Chemical compound, drug	Propofol	Sigma Aldrich	Y0000016	
Software algorithm	iMODfit	López-Blanco and Chacón, 2013		
Software algorithm	MOLEonline	Pravda et al, 2018		

Software algorithm	Clampfit	Molecular devices
Software algorithm	AxoGraph X	https://axograph.com/

704 **Mutagenesis**

705 All GLIC mutants were obtained using site directed mutagenesis on the
706 C27S background of GLIC, except Bim136-Q101W-Y28F (C27) for which the
707 endogenous cysteine was introduced back. Similarly to previous studies (Sauguet
708 et al., 2014; Menny et al., 2017; Nemezc et al., 2017), two different vectors were
709 used: a pet20b vector with GLIC fused to MBP by a linker containing a thrombin
710 cleavage site under a T7 promoter for expression in *E. coli* BL21; a pmt3 vector for
711 expression in oocytes with GLIC containing a Cter HA tag and in Nter the peptide
712 signal from $\alpha 7$ -nAChR. Incorporation of the mutations in both vectors were verified
713 by sequencing.

714 **GLIC mutants production and purification**

715 Protein production of MBP-GLIC and labeling was done as previously
716 described (Menny et al., 2017) with a few modifications. In brief, MBP-GLIC was
717 expressed in BL21 *E coli* cells overnight at 20°C after induction by 100 μ M IPTG.
718 Cells were collected and resuspended in buffer A containing 20 mM Tris; 300 mM
719 NaCl at pH 7.4 and subsequently disrupted by sonication. After membrane
720 separation by ultracentrifugation, membrane proteins were extracted overnight in
721 buffer A supplemented with 2 % DDM. After ultracentrifugation, supernatant was
722 incubated with amylose resin and MBP-GLIC was eluted using buffer A
723 supplemented with DDM 0.02 % and saturating concentration of maltose. To
724 remove endogenous maltoporin contaminant, a first size exclusion
725 chromatography was performed on superose 6 10/300 GL in buffer A with 0.02 %
726 DDM. GLIC-MBP concentration was measured and the protein was incubated
727 overnight at 4°C with thrombin to cleave off MBP and with monobromobimane
728 (mBBr) at a 1:5 (GLIC monomer:fluorophore) ratio, to label the protein. The mBBr
729 dye being solubilized in DMSO, the sample volume was adjusted to remain below
730 1% DMSO final concentration. After labeling, a second gel filtration was done to
731 get rid of the MBP and unbound dye molecules. GLIC-Bimane samples were flash
732 frozen in liquid nitrogen and stored at -80°C prior to fluorescence measurements.

733 **Steady-state fluorescence measurements**

734 Fluorescence measurements were done as previously described (Menny et
735 al., 2017). Samples were equilibrated to room temperature and diluted with buffer
736 A with 0.02 % DDM to reach a concentration around 40 $\mu\text{g}\cdot\text{mL}^{-1}$. Fluorescence
737 recording buffers consisting of 300 mM NaCl, 2.7 mM KCl, 5.3 mM Na_2HPO_4 and
738 1.5 mM KH_2PO_4 were prepared beforehand and their pH was adjusted either to
739 7.4 or to different pH in order to reach the desired pH value (from pH 8 to 3) after
740 mixing equal volumes with Buffer A 0.02 % DDM. Measurements were done at
741 20°C in 1 mL disposable UV transparent 2.5 mL cuvettes in a Jasco 8200
742 fluorimeter with 385 nm excitation wavelength and the emission spectra was
743 recorded through 2.5 nm slits from 420 to 530 nm. Parameters were kept constant
744 throughout the study. On the sample at pH 7.4, an addition of SDS to reach 1 %
745 final concentration was done to obtain the F_{SDS} value and a tryptophan emission
746 spectrum was done before and after SDS addition in order to monitor
747 denaturation.

748 Fitting of fluorescence measurements was done on each fluorescence
749 series (values from one pH range) with at least 3 series per mutant using the
750 following Hill equation:

$$y(x) = \frac{\Delta F_{\text{max}} + x^{n_H}}{x^{n_H} + EC_{50}^{n_H}} + F_0$$

751 where ΔF_{max} represents the maximal change in fluorescence amplitude; F_0 the
752 initial fluorescence at pH 7.8; n_H represents the hill number and EC_{50} the proton
753 concentration for which half of the maximal fluorescence change is measured. For
754 Bim136-Q101W and Bim250-Y197 and in some other mutants, we excluded from
755 the fit the data point below pH 3.5 that show a small but significant change in
756 fluorescence intensity in the opposite direction to the quenching curves. We did
757 not fit the Bim135-W72 mutant that shows a bell-shaped curve.

758 **Electrophysiological recordings**

759 Electrophysiological recordings of GLIC were made on *Xenopus* oocytes
760 provided either by the Centre de Ressources Biologiques Xénopes (Rennes-
761 France) or by Ecocyte Bioscience (Dortmund-Germany). Recordings were made
762 as previously described (Nury et al., 2011) with oocytes 48-96 h post nucleus
763 injection with a mix containing 80 $\text{ng}\cdot\mu\text{L}^{-1}$ of GLIC cDNA and 25 $\text{ng}\cdot\mu\text{L}^{-1}$ of GFP
764 cDNA. Recordings were done in MES buffer containing 100 mM NaCl, 3 mM KCl,
765 1 mM CaCl_2 , 1 mM MgCl_2 and 10 mM MES with pH adjusted by addition of 2 M

766 HCl. The perfusion chamber contained two compartments and only a portion of the
767 oocyte was perfused with low pH solution. Bunte salt bimeane labeling was
768 performed prior to recording by incubation for 1h at room temperature with the dye
769 concentrated at 1 mM in MES buffer. To correct data for rundown, a solution with a
770 pH value in the middle of the pH range (usually pH 5) was used as a reference at
771 the beginning and the end of the recording and every 3/4 applications. To limit the
772 effect of propofol that can stay in the membrane in-between applications (Heusser
773 et al., 2018), only a limited number of pH solutions were tested per oocyte.

774 Electrophysiological recordings were analyzed using AxoGraph X and
775 Prism was used to fit individual pH-dependent recording using the Hill equation:

$$y(x) = \frac{I_{max} + x^{n_H}}{x^{n_H} + EC_{50}^{n_H}}$$

776 where I_{max} represents the maximal current in percentage of the response from the
777 reference solution. n_H represents the hill number and EC_{50} the proton
778 concentration for which half of the maximal electrophysiological response is
779 recorded.

780 **Xenopus oocytes immunolabeling**

781 Mutants generating currents smaller than 500 nA at high proton
782 concentrations were categorized as non-functional. For these non-functional
783 mutants, expression tests were performed by immunolabeling of oocytes as
784 previously described (Prevost et al., 2012; Sauguet et al., 2014). 3 to 4 days post
785 injection, GFP positive oocytes were fixed overnight in paraformaldehyde (PFA) 4
786 % at 4°C. Immunolabeling was performed after 30 min saturation by 10 % horse
787 serum in PBS buffer. Rabbit anti HA-tag primary antibody was incubated for 90
788 min in 2 % horse serum and the secondary antibody anti-Rabbit coupled to Alexa
789 Fluor 645 was incubated for 30 min. After a second PFA fixation overnight,
790 oocytes were included in warm 3 % low-melting agarose and 40 μ m slices were
791 made using a vibratome on a portion of the oocyte. Several slices per oocytes
792 were mounted one a slide and analyzed in an epi-fluorescence microscope using
793 constant exposure time between non-functional mutant and functional mutants
794 used as positive controls.

795 **Molecular Modeling**

796 The iMODfit flexible fitting method (López-Blanco and Chacón, 2013)
797 searches the conformational space using the lowest normal modes for the best

798 cross-correlation fit of a starting conformation atomic model into a target
799 conformation density map. Two trajectories were generated here. In trajectory A
800 structure 4NPQ (GLIC-pH 7) is fitted to the density of 4HFI (GLIC-pH 4), and in
801 trajectory B structure 4HFI is fitted to the density of 4NPQ.

802 The detailed procedure is performed as follows, taking as an example
803 trajectory A:

804 1/ A computed EM density map was generated for the X-ray structure of the target
805 4NPQ using the pdb2vol tool (called 4NPQ map). The EM density map resolution
806 was set to 5 Å and the grid size to 0.5 Å, i.e. the resolution was set at a relatively
807 large value to avoid being locked in local minima during the iMODfit procedure.

808 2/ 4HFI was represented with the detailed all heavy-atoms force field (all atoms
809 are considered except hydrogens), called the 4HFI model.

810 3/ The lowest-frequency NMA-modes of the 4HFI model were computed. For the
811 subsequent steps, the range of modes considered (-n option) was set to 0.5, i.e.
812 half of the modes, corresponding to the lower frequency modes, are considered for
813 computing the conformational changes.

814 4/ During the iMODfit procedure, starting from the 4HFI model, 10% of the modes
815 are randomly selected and used to generate a very small conformational change.
816 The new conformation is used to compute a simulated density map, and the new
817 conformation is accepted only if the cross-correlation between the targeted 4NPQ
818 and simulated maps improves. This process is repeated iteratively until the
819 conformation deviates by a RMSD of 0.5 Å from the starting/previous model, in
820 which case an intermediate structure is generated and stored. The entire process
821 is then repeated iteratively to generate a series of intermediate states that
822 progressively converge to the targeted structure.

823 The geometry of the ion channel has been computed with MOLEonline
824 web server (mole.upol.cz), with the 'pore' mode (Sehna et al., 2013). We used the
825 FreeRadius value computed at the level of the I9' residue.

826 For the Bimane docking procedure on each intermediate structure, the
827 position of side chains was first optimized with the software Scwrl4 (Krivov et al.,
828 2009) while keeping the main chain rigid. This step also allowed the introduction of
829 point mutations. The structure of the protein and bimeane was converted to pdbqt
830 files with the software open babel 2.4.1. Covalent docking was then performed
831 with the software smina (Koes et al., 2013). The box for docking has been defined

832 around the mutated cysteine residue, with a size of 30 Å in each direction.
 833 Covalent docking forced the bimane to be in appropriate distance with the sulfur
 834 atom of the introduced cysteine. Only the first pose was kept for further analysis.

835 **MWC Model building**

836 To build a 3-states MWC model, the following equations were used to ob-
 837 tain the population of each state resting, pre-active and active:

$$\bar{A} = \frac{(1 + \alpha)^5 \times (1 + \alpha')^5}{(1 + \alpha)^5 \times (1 + \alpha')^5 + L_{pA}L_A(1 + C_{pA}C_A\alpha)^5 \times (1 + C_{pA}'C_A'\alpha')^5 + L_A(1 + C_A\alpha)^5 \times (1 + C_A'\alpha')^5}$$

$$\bar{pA} = \frac{L_A(1 + C_A\alpha)^5 \times (1 + C_A'\alpha')^5}{(1 + \alpha)^5 \times (1 + \alpha')^5 + L_{pA}L_A(1 + C_{pA}C_A\alpha)^5 \times (1 + C_{pA}'C_A'\alpha')^5 + L_A(1 + C_A\alpha)^5 \times (1 + C_A'\alpha')^5}$$

$$\bar{R} = \frac{L_{pA}L_A(1 + C_{pA}C_A\alpha)^5 \times (1 + C_{pA}'C_A'\alpha')^5}{(1 + \alpha)^5 \times (1 + \alpha')^5 + L_{pA}L_A(1 + C_{pA}C_A\alpha)^5 \times (1 + C_{pA}'C_A'\alpha')^5 + L_A(1 + C_A\alpha)^5 \times (1 + C_A'\alpha')^5}$$

838 With constants defined below:

$$L_{pA} = \frac{\bar{R}_{pH8}}{pA_{pH8}} \quad C_{pA} = \frac{K_{pA}}{K_R} \quad C'_{pA} = \frac{K'_{pA}}{K'_R} \quad \alpha = \frac{[H^+]}{K_A}$$

$$L_A = \frac{pA_{pH8}}{A_{pH8}} \quad C_A = \frac{K_A}{K_{pA}} \quad C'_A = \frac{K'_A}{K'_{pA}} \quad \alpha' = \frac{[H^+]}{K'_A}$$

839 The weighted fluorescence value was calculated as followed:

$$F = \bar{R} \times F_R + \bar{pA} \times F_{pA} + \bar{A} \times F_A$$

840 With fluorescence values set at:

$$F_R^{\text{Bim136-Q101W}} = 0.70 \quad F_R^{\text{Bim250-Y197}} = 0.56$$

$$F_{pA}^{\text{Bim136-Q101W}} = 0.30 \quad F_{pA}^{\text{Bim250-Y197}} = 0.92$$

$$841 \quad F_A^{\text{Bim136-Q101W}} = 0.30 \quad F_A^{\text{Bim250-Y197}} = 0.92$$

842 Isomerization constants were manually adjusted to fit theoretical and ex-
 843 perimental fluorescence quenching curves and normalized electrophysiological
 844 curves. Of note, the fluorescence variations of E26Q mutant were normalized to
 845 that of the Bim136-Q101W, to correct for its effect on the fluorescence at pH 7
 846 which likely reflects an alteration of the structure of the resting state, independently
 847 of the allosteric transitions. Additionally, the \bar{A} population for the Y28F mutant does
 848 not reach 1, so it was normalized in order to compare the values with the normal-
 849 ized experimental data.

850 **REFERENCES**

851 Althoff T, Hibbs RE, Banerjee S and Gouaux E. 2014. 'X-ray structures of GluCl in
 852 apo states reveal a gating mechanism of Cys-loop receptors'. *Nature*,
 853 512(7514), pp. 333–337. doi: 10.1038/nature13669.

854 Bahar I, Lezon TR, Bakan A and Shrivastava IH. 2010. 'Normal Mode Analysis of

- 855 Biomolecular Structures: Functional Mechanisms of Membrane Proteins'.
856 *Chemical Reviews*, 110(3), pp. 1463–1497. doi: 10.1021/cr900095e.
- 857 Bertozzi C, Zimmermann I, Engeler S, Hilf RJC and Dutzler R. 2016. 'Signal
858 Transduction at the Domain Interface of Prokaryotic Pentameric Ligand-Gated
859 Ion Channels'. *PLOS Biology*. Edited by P.-J. Corringer, 14(3), p. e1002393.
860 doi: 10.1371/journal.pbio.1002393.
- 861 Bocquet N, Prado de Carvalho L, Cartaud J, Neyton J, Le Poupon C, Taly A,
862 Grutter T, Changeux J-P and Corringer P-J. 2007. 'A prokaryotic proton-gated
863 ion channel from the nicotinic acetylcholine receptor family'. *Nature*, 445(7123),
864 pp. 116–119. doi: 10.1038/nature05371.
- 865 Bocquet N, Nury H, Baaden M, Le Poupon C, Changeux J-P, Delarue M and
866 Corringer P-J. 2009. 'X-ray structure of a pentameric ligand-gated ion channel
867 in an apparently open conformation.' *Nature*. Nature Publishing Group,
868 457(7225), pp. 111–114. doi: 10.1038/nature07462.
- 869 Bode A and Lynch JW. 2014. 'The impact of human hyperekplexia mutations on
870 glycine receptor structure and function'. *Molecular Brain*, 7(1), p. 2. doi:
871 10.1186/1756-6606-7-2.
- 872 Calimet N, Simoes M, Changeux J-P, Karplus M, Taly A and Cecchini M. 2013.
873 'PNAS Plus: From the Cover: A gating mechanism of pentameric ligand-gated
874 ion channels'. *Proceedings of the National Academy of Sciences*, 110(42), pp.
875 E3987–E3996. doi: 10.1073/pnas.1313785110.
- 876 Carswell CL, Sun J and Baenziger JE. 2015. 'Intramembrane Aromatic
877 Interactions Influence the Lipid Sensitivities of Pentameric Ligand-gated Ion
878 Channels'. *Journal of Biological Chemistry*, 290(4), pp. 2496–2507. doi:
879 10.1074/jbc.M114.624395.
- 880 Cheng MH, Coalson RD and Tang P. 2010. 'Molecular Dynamics and Brownian
881 Dynamics Investigation of Ion Permeation and Anesthetic Halothane Effects on
882 a Proton-Gated Ion Channel'. *Journal of the American Chemical Society*,
883 132(46), pp. 16442–16449. doi: 10.1021/ja105001a.
- 884 Du J, Lü W, Wu S, Cheng Y and Gouaux E. 2015. 'Glycine receptor mechanism
885 elucidated by electron cryo-microscopy'. *Nature*, 526(7572), pp. 224–229. doi:
886 10.1038/nature14853.
- 887 Duret G, Van Renterghem C, Weng Y, Prevost M, Moraga-Cid G, Huon C, Sonner
888 JM and Corringer P-J. 2011. 'Functional prokaryotic-eukaryotic chimera from
889 the pentameric ligand-gated ion channel family'. *Proceedings of the National
890 Academy of Sciences*, 108(29), pp. 12143–12148. doi:
891 10.1073/pnas.1104494108.
- 892 Elenes S and Auerbach A. 2002. 'Desensitization of diliganded mouse muscle
893 nicotinic acetylcholine receptor channels'. *The Journal of Physiology*, 541(2),
894 pp. 367–383. doi: 10.1113/jphysiol.2001.016022.
- 895 Esmenjaud J, Stroebel D, Chan K, Grand T, David M, Wollmuth LP, Taly A and
896 Paoletti P. 2019. 'An inter-dimer allosteric switch controls NMDA receptor
897 activity'. *The EMBO Journal*, 38(2), pp. 1–16. doi: 10.15252/emboj.201899894.
- 898 Fourati Z, Howard RJ, Heusser SA, Hu H, Ruza RR, Sauguet L, Lindahl E and
899 Delarue M. 2018. 'Structural Basis for a Bimodal Allosteric Mechanism of

- 900 General Anesthetic Modulation in Pentameric Ligand-Gated Ion Channels'. *Cell*
901 *Reports*. Elsevier Company., 23(4), pp. 993–1004. doi:
902 10.1016/j.celrep.2018.03.108.
- 903 Fritsch S, Ivanov I, Wang H and Cheng X. 2011. 'Ion Selectivity Mechanism in a
904 Bacterial Pentameric Ligand-Gated Ion Channel'. *Biophysical Journal*.
905 Biophysical Society, 100(2), pp. 390–398. doi: 10.1016/j.bpj.2010.11.077.
- 906 Galzi JL, Edelstein SJ and Changeux J-P. 1996. 'The multiple phenotypes of
907 allosteric receptor mutants.' *Proceedings of the National Academy of Sciences*,
908 93(5), pp. 1853–1858. doi: 10.1073/pnas.93.5.1853.
- 909 Gharpure A, Teng J, Zhuang Y, Noviello CM, Walsh RM, Cabuco R, Howard RJ,
910 Zaveri NT, Lindahl E and Hibbs RE. 2019. 'Agonist Selectivity and Ion
911 Permeation in the $\alpha 3\beta 4$ Ganglionic Nicotinic Receptor'. *Neuron*, 104(3), pp.
912 501-511.e6. doi: 10.1016/j.neuron.2019.07.030.
- 913 Ghosh B, Tsao TW and Czajkowski C. 2017. 'A chimeric prokaryotic-eukaryotic
914 pentameric ligand gated ion channel reveals interactions between the
915 extracellular and transmembrane domains shape neurosteroid modulation'.
916 *Neuropharmacology*. Elsevier Ltd, 125, pp. 343–352. doi:
917 10.1016/j.neuropharm.2017.08.007.
- 918 Gielen M, Barilone N and Corringer PJ. 2020. 'The desensitization pathway of
919 GABAA receptors, one subunit at a time'. *Nature Communications*. Springer
920 US, 11(1), pp. 1–14. doi: 10.1038/s41467-020-19218-6.
- 921 Gonzalez-Gutierrez G, Wang Y, Cymes GD, Tajkhorshid E and Grosman C. 2017.
922 'Chasing the open-state structure of pentameric ligand-gated ion channels'.
923 *Journal of General Physiology*, 149(12), pp. 1119–1138. doi:
924 10.1085/jgp.201711803.
- 925 Gupta S, Chakraborty S, Vij R and Auerbach A. 2017. 'A mechanism for
926 acetylcholine receptor gating based on structure, coupling, phi, and flip'. *Journal*
927 *of General Physiology*, 149(1), pp. 85–103. doi: 10.1085/jgp.201611673.
- 928 Heidmann T and Changeux J-P. 1980. 'Interaction of a fluorescent agonist with the
929 membrane-bound acetylcholine receptor from *Torpedomarmorata* in the
930 millisecond time range: Resolution of an "intermediate" conformational transition
931 and evidence for positive cooperative effects'. *Biochemical and Biophysical*
932 *Research Communications*, 97(3), pp. 889–896. doi: 10.1016/0006-
933 291X(80)91460-6.
- 934 Hernandez CC and Macdonald RL. 2019. 'A structural look at GABAA receptor
935 mutations linked to epilepsy syndromes'. *Brain Research*. Elsevier B.V.,
936 1714(July 2018), pp. 234–247. doi: 10.1016/j.brainres.2019.03.004.
- 937 Heusser SA, Lycksell M, Wang X, McComas SE, Howard RJ and Lindahl E. 2018.
938 'Allosteric potentiation of a ligand-gated ion channel is mediated by access to a
939 deep membrane-facing cavity'. *Proceedings of the National Academy of*
940 *Sciences*, 115(42), pp. 10672–10677. doi: 10.1073/pnas.1809650115.
- 941 Hilf RJC and Dutzler R. 2008. 'X-ray structure of a prokaryotic pentameric ligand-
942 gated ion channel'. *Nature*, 452(7185), pp. 375–379. doi: 10.1038/nature06717.
- 943 Hu H, Nemezc Á, Van Renterghem C, Fourati Z, Sauguet L, Corringer P-J and
944 Delarue M. 2018. 'Crystal structures of a pentameric ion channel gated by

- 945 alkaline pH show a widely open pore and identify a cavity for modulation'.
 946 *Proceedings of the National Academy of Sciences*, 115(17), pp. E3959–E3968.
 947 doi: 10.1073/pnas.1717700115.
- 948 Hu H, Howard RJ, Bastolla U, Lindahl E and Delarue M. 2020. 'Structural basis for
 949 allosteric transitions of a multidomain pentameric ligand-gated ion channel'.
 950 *Proceedings of the National Academy of Sciences*, 117(24), pp. 13437–13446.
 951 doi: 10.1073/pnas.1922701117.
- 952 Jaiteh M, Taly A and Hénin J. 2016. 'Evolution of Pentameric Ligand-Gated Ion
 953 Channels: Pro-Loop Receptors'. *PLOS ONE*. Edited by S. Bertrand, 11(3), p.
 954 e0151934. doi: 10.1371/journal.pone.0151934.
- 955 Johannesen K *et al.* 2016. 'Phenotypic spectrum of GABRA1'. *Neurology*, 87(11),
 956 pp. 1140–1151. doi: 10.1212/WNL.0000000000003087.
- 957 Jones Brunette AM and Farrens DL. 2014. 'Distance Mapping in Proteins Using
 958 Fluorescence Spectroscopy: Tyrosine, like Tryptophan, Quenches Bimane
 959 Fluorescence in a Distance-Dependent Manner'. *Biochemistry*, 53(40), pp.
 960 6290–6301. doi: 10.1021/bi500493r.
- 961 Koes DR, Baumgartner MP and Camacho CJ. 2013. 'Lessons Learned in
 962 Empirical Scoring with smina from the CSAR 2011 Benchmarking Exercise'.
 963 *Journal of Chemical Information and Modeling*, 53(8), pp. 1893–1904. doi:
 964 10.1021/ci300604z.
- 965 Krivov GG, Shapovalov M V. and Dunbrack RL. 2009. 'Improved prediction of
 966 protein side-chain conformations with SCWRL4'. *Proteins: Structure, Function,
 967 and Bioinformatics*, 77(4), pp. 778–795. doi: 10.1002/prot.22488.
- 968 Laha KT, Ghosh B and Czajkowski C. 2013. 'Macroscopic Kinetics of Pentameric
 969 Ligand Gated Ion Channels: Comparisons between Two Prokaryotic Channels
 970 and One Eukaryotic Channel'. *PLoS ONE*. Edited by J. D. Spafford, 8(11), p.
 971 e80322. doi: 10.1371/journal.pone.0080322.
- 972 Lape R, Plested AJR, Moroni M, Colquhoun D and Sivilotti LG. 2012. 'The 1K276E
 973 Startle Disease Mutation Reveals Multiple Intermediate States in the Gating of
 974 Glycine Receptors'. *Journal of Neuroscience*, 32(4), pp. 1336–1352. doi:
 975 10.1523/JNEUROSCI.4346-11.2012.
- 976 Lape R, Colquhoun D and Sivilotti LG. 2008. 'On the nature of partial agonism in
 977 the nicotinic receptor superfamily'. *Nature*, 454(7205), pp. 722–727. doi:
 978 10.1038/nature07139.
- 979 Laverty D, Thomas P, Field M, Andersen OJ, Gold MG, Biggin PC, Gielen M and
 980 Smart TG. 2017. 'Crystal structures of a GABAA-receptor chimera reveal new
 981 endogenous neurosteroid-binding sites'. *Nature Structural & Molecular Biology*.
 982 Nature Publishing Group, 24(11), pp. 977–985. doi: 10.1038/nsmb.3477.
- 983 Lev B, Murail S, Poitevin F, Cromer BA, Baaden M, Delarue M and Allen TW.
 984 2017. 'String method solution of the gating pathways for a pentameric ligand-
 985 gated ion channel'. *Proceedings of the National Academy of Sciences*, 114(21),
 986 pp. E4158–E4167. doi: 10.1073/pnas.1617567114.
- 987 Lopéz-Blanco JR and Chacón P. 2013. 'iMODFIT: Efficient and robust flexible
 988 fitting based on vibrational analysis in internal coordinates'. *Journal of Structural
 989 Biology*. Elsevier Inc., 184(2), pp. 261–270. doi: 10.1016/j.jsb.2013.08.010.

- 990 Mansoor SE, DeWitt M a. and Farrens DL. 2010. 'Distance Mapping in Proteins
991 Using Fluorescence Spectroscopy: The Tryptophan-Induced Quenching (TrIQ)
992 Method'. *Biochemistry*, 49(45), pp. 9722–9731. doi: 10.1021/bi100907m.
- 993 Mansoor SE, Mchaourab HS and Farrens DL. 2002. 'Mapping Proximity within
994 Proteins Using Fluorescence Spectroscopy. A Study of T4 Lysozyme Showing
995 That Tryptophan Residues Quench Bimane Fluorescence †'. *Biochemistry*,
996 41(8), pp. 2475–2484. doi: 10.1021/bi011198i.
- 997 Masiulis S, Desai R, Uchański T, Serna Martin I, Laverty D, Karia D, Malinauskas
998 T, Zivanov J, Pardon E, Kotecha A, Steyaert J, Miller KW and Aricescu AR.
999 2019. 'GABAA receptor signalling mechanisms revealed by structural
1000 pharmacology'. *Nature*, 565(7740), pp. 454–459. doi: 10.1038/s41586-018-
1001 0832-5.
- 1002 Menny A, Lefebvre SN, Schmidpeter PA, Drege E, Fourati Z, Delarue M, Edelstein
1003 SJ, Nimigean CM, Joseph D and Corringer P-J. 2017. 'Identification of a pre-
1004 active conformation of a pentameric channel receptor'. *eLife*, 3. doi:
1005 10.1111/imm.12796.
- 1006 Moraga-Cid G, Sauguet L, Huon C, Malherbe L, Girard-Blanc C, Petres S, Murail
1007 S, Taly A, Baaden M, Delarue M and Corringer P-J. 2015. 'Allosteric and
1008 hyperekplexic mutant phenotypes investigated on an α 1 glycine receptor
1009 transmembrane structure'. *Proceedings of the National Academy of Sciences*,
1010 112(9), pp. 2865–2870. doi: 10.1073/pnas.1417864112.
- 1011 Mukhtasimova N, Lee WY, Wang H-L and Sine SM. 2009. 'Detection and trapping
1012 of intermediate states priming nicotinic receptor channel opening'. *Nature*.
1013 Nature Publishing Group, 459(7245), pp. 451–454. doi: 10.1038/nature07923.
- 1014 Nemezc Á, Prevost MS, Menny A and Corringer P-J. 2016. 'Emerging Molecular
1015 Mechanisms of Signal Transduction in Pentameric Ligand-Gated Ion Channels'.
1016 *Neuron*, 90(3), pp. 452–470. doi: 10.1016/j.neuron.2016.03.032.
- 1017 Nemezc Á, Hu H, Fourati Z, Van Renterghem C, Delarue M and Corringer P-J.
1018 2017. 'Full mutational mapping of titratable residues helps to identify proton-
1019 sensors involved in the control of channel gating in the *Gloeobacter violaceus*
1020 pentameric ligand-gated ion channel'. *PLOS Biology*. Edited by R. Dutzler,
1021 15(12), p. e2004470. doi: 10.1371/journal.pbio.2004470.
- 1022 Nury H, Bocquet N, Le Poupon C, Raynal B, Haouz A, Corringer P-J and Delarue
1023 M. 2010. 'Crystal Structure of the Extracellular Domain of a Bacterial Ligand-
1024 Gated Ion Channel'. *Journal of Molecular Biology*, 395(5), pp. 1114–1127. doi:
1025 10.1016/j.jmb.2009.11.024.
- 1026 Nury H, Van Renterghem C, Weng Y, Tran A, Baaden M, Dufresne V, Changeux
1027 J-P, Sonner JM, Delarue M and Corringer P-J. 2011. 'X-ray structures of
1028 general anaesthetics bound to a pentameric ligand-gated ion channel'. *Nature*.
1029 Nature Publishing Group, a division of Macmillan Publishers Limited. All Rights
1030 Reserved., 469(7330), pp. 428–431. doi: 10.1038/nature09647.
- 1031 Onufriev A, Case DA and Ullmann GM. 2001. 'A Novel View of pH Titration in
1032 Biomolecules †'. *Biochemistry*, 40(12), pp. 3413–3419. doi: 10.1021/bi002740q.
- 1033 Orellana L, Yoluk O, Carrillo O, Orozco M and Lindahl E. 2016. 'Prediction and
1034 validation of protein intermediate states from structurally rich ensembles and

- 1035 coarse-grained simulations'. *Nature Communications*. Nature Publishing Group,
1036 7(1), p. 12575. doi: 10.1038/ncomms12575.
- 1037 Parikh RB, Bali M and Akabas MH. 2011. 'Structure of the M2 Transmembrane
1038 Segment of GLIC, a Prokaryotic Cys Loop Receptor Homologue from
1039 *Gloeobacter violaceus*, Probed by Substituted Cysteine Accessibility'. *Journal*
1040 *of Biological Chemistry*, 286(16), pp. 14098–14109. doi:
1041 10.1074/jbc.M111.221895.
- 1042 Plested AJR, Groot-kormelink PJ, Colquhoun D and Sivilotti LG. 2007. 'Single-
1043 channel study of the spasmodic mutation α 1A52S in recombinant rat glycine
1044 receptors'. *Journal of Physiology*, 581(1), pp. 51–73. doi:
1045 10.1113/jphysiol.2006.126920.
- 1046 Plested AJR. 2014. 'Don't Flip Out: AChRs are Primed to Catch and Hold Your
1047 Attention'. *Biophysical Journal*. Elsevier, 107(1), pp. 8–9. doi:
1048 10.1016/j.bpj.2014.05.021.
- 1049 Polovinkin L, Hassaine G, Perot J, Neumann E, Jensen AA, Lefebvre SN,
1050 Corringer P-J, Neyton J, Chipot C, Dehez F, Schoehn G and Nury H. 2018.
1051 'Conformational transitions of the serotonin 5-HT₃ receptor'. *Nature*, 563(7730),
1052 pp. 275–279. doi: 10.1038/s41586-018-0672-3.
- 1053 Prevost MS, Sauguet L, Nury H, Van Renterghem C, Huon C, Poitevin F, Baaden
1054 M, Delarue M and Corringer P-J. 2012. 'A locally closed conformation of a
1055 bacterial pentameric proton-gated ion channel'. *Nature Structural & Molecular*
1056 *Biology*. Nature Publishing Group, a division of Macmillan Publishers Limited.
1057 All Rights Reserved., 19(6), pp. 642–649. doi: 10.1038/nsmb.2307.
- 1058 Prevost MS, Moraga-Cid G, Van Renterghem C, Edelstein SJ, Changeux J-P and
1059 Corringer P-J. 2013. 'Intermediate closed state for glycine receptor function
1060 revealed by cysteine cross-linking.' *Proceedings of the National Academy of*
1061 *Sciences of the United States of America*, 110(42), pp. 17113–8. doi:
1062 10.1073/pnas.1317009110.
- 1063 Rienzo M, Rocchi AR, Threatt SD, Dougherty DA and Lummis SCR. 2016.
1064 'Perturbation of Critical Prolines in *Gloeobacter violaceus* Ligand-gated Ion
1065 Channel (GLIC) Supports Conserved Gating Motions among Cys-loop
1066 Receptors'. *Journal of Biological Chemistry*, 291(12), pp. 6272–6280. doi:
1067 10.1074/jbc.M115.694372.
- 1068 Rienzo M, Lummis SCR and Dougherty DA. 2014. 'Structural Requirements in the
1069 Transmembrane Domain of GLIC Revealed by Incorporation of Noncanonical
1070 Histidine Analogs'. *Chemistry & Biology*, 21(12), pp. 1700–1706. doi:
1071 10.1016/j.chembiol.2014.10.019.
- 1072 Rovsniik U, Zhuang Y, Forsberg BO, Carroni M, Yvonesdotter L, Howard RJ and
1073 Lindahl E. 2021. 'Dynamic closed states of a ligand-gated ion channel captured
1074 by cryo-EM and simulations'. *bioRxiv*. doi: 10.1101/2021.01.04.425171.
- 1075 Sakmann B, Patlak J and Neher E. 1980. 'Single acetylcholine-activated channels
1076 show burst-kinetics in presence of desensitizing concentrations of agonist'.
1077 *Nature*, 286(5768), pp. 71–73. doi: 10.1038/286071a0.
- 1078 Sauguet L, Poitevin F, Murail S, Van Renterghem C, Moraga-Cid G, Malherbe L,
1079 Thompson AW, Koehl P, Corringer P-J, Baaden M and Delarue M. 2013.

- 1080 'Structural basis for ion permeation mechanism in pentameric ligand-gated ion
1081 channels'. *The EMBO Journal*. EMBO Press, 32(5), pp. 728–741. doi:
1082 10.1038/emboj.2013.17.
- 1083 Sauguet L, Shahsavari A, Poitevin F, Huon C, Menny A, Nemezc A, Haouz A,
1084 Changeux J-P, Corringer P-J and Delarue M. 2014. 'Crystal structures of a
1085 pentameric ligand-gated ion channel provide a mechanism for activation'.
1086 *Proceedings of the National Academy of Sciences*, 111(3), pp. 966–971. doi:
1087 10.1073/pnas.1314997111.
- 1088 Sauguet L, Shahsavari A and Delarue M. 2015. 'Crystallographic studies of
1089 pharmacological sites in pentameric ligand-gated ion channels'. *Biochimica et*
1090 *Biophysica Acta (BBA) - General Subjects*. Elsevier B.V., 1850(3), pp. 511–523.
1091 doi: 10.1016/j.bbagen.2014.05.007.
- 1092 Saul B, Kuner T, Sobetzko D, Brune W, Hanefeld F, Meinck H-M and Becker C-M.
1093 1999. 'Novel GLRA1 Missense Mutation (P250T) in Dominant Hyperekplexia
1094 Defines an Intracellular Determinant of Glycine Receptor Channel Gating'. *The*
1095 *Journal of Neuroscience*, 19(3), pp. 869–877. doi: 10.1523/JNEUROSCI.19-03-
1096 00869.1999.
- 1097 Schmandt N, Velisetty P, Chalamalasetti S V., Stein RA, Bonner R, Talley L,
1098 Parker MD, Mchaourab HS, Yee VC, Lodowski DT and Chakrapani S. 2015. 'A
1099 chimeric prokaryotic pentameric ligand-gated channel reveals distinct pathways
1100 of activation'. *The Journal of General Physiology*, 146(4), pp. 323–340. doi:
1101 10.1085/jgp.201511478.
- 1102 Sehnal D, Svobodová Vařeková R, Berka K, Pravda L, Navrátilová V, Banáš P,
1103 Ionescu C-M, Otyepka M and Koča J. 2013. 'MOLE 2.0: advanced approach for
1104 analysis of biomacromolecular channels'. *Journal of Cheminformatics*, 5(1), p.
1105 39. doi: 10.1186/1758-2946-5-39.
- 1106 Shen X, Fukuda T, Ohno K, Sine SM and Engel AG. 2008. 'Congenital
1107 myasthenia-related AChR δ subunit mutation interferes with intersubunit
1108 communication essential for channel gating'. *Journal of Clinical Investigation*,
1109 118(5), pp. 1867–1876. doi: 10.1172/JCI34527.
- 1110 Taly A, Delarue M, Grutter T, Nilges M, Le Novère N, Corringer P-J and Changeux
1111 J-P. 2005. 'Normal Mode Analysis Suggests a Quaternary Twist Model for the
1112 Nicotinic Receptor Gating Mechanism'. *Biophysical Journal*, 88(6), pp. 3954–
1113 3965. doi: 10.1529/biophysj.104.050229.
- 1114 Taly A and Changeux J-P. 2008. 'Functional Organization and Conformational
1115 Dynamics of the Nicotinic Receptor'. *Annals of the New York Academy of*
1116 *Sciences*, 1132(1), pp. 42–52. doi: 10.1196/annals.1405.008.
- 1117 Tiwari V, Borchardt J, Schuh A, Klug CS and Czajkowski C. 2020. 'Ligand-induced
1118 motions in pentameric ligand-gated ion channels revealed by EPR
1119 spectroscopy'. *bioRxiv*. doi: 10.1101/2020.11.04.368233.
- 1120 Yu J, Zhu H, Lape R, Greiner T, Du J, Lü W, Sivilotti L and Gouaux E. 2021.
1121 'Mechanism of gating and partial agonist action in the glycine receptor'. *Cell*.
1122 Elsevier Inc., 184(4), pp. 957-968.e21. doi: 10.1016/j.cell.2021.01.026.
- 1123 Zimmermann I and Dutzler R. 2011. 'Ligand Activation of the Prokaryotic
1124 Pentameric Ligand-Gated Ion Channel ELIC'. *PLoS Biology*. Edited by D. E.

1125 Clapham, 9(6), p. e1001101. doi: 10.1371/journal.pbio.1001101.

1126 **ACKNOWLEDGMENTS**

1127 The work was supported by the ‘Agence Nationale de la Recherche’ (grant
1128 ANR-13-BSV8-0020, Pentagate), the doctoral school ED3C and the ‘Foundation
1129 pour la Recherche Médicale’ (PhD funding to SNL), the “Initiative d'Excellence”
1130 (cluster of excellence LABEX Dynamo, ANR-11-LABX-0011 to AT) and the ERC
1131 (grant No. 788974, Dynacotine). The authors would like to thank Stuart Edelstein
1132 for helping with MWC equations, Marc Gielen, Akos Nemezc and Marie Prévost
1133 for critical reading of the manuscript.

1134 **AUTHOR CONTRIBUTION**

1135 SNL and PJC designed fluorescent quenching experiments; SNL, AM and
1136 KM performed experiments; AT designed and performed in silico calculations. PJC
1137 designed and performed MWC allosteric modeling. All authors analyzed the data.
1138 SNL and PJC wrote the manuscript with the help of the other authors.

1139

Mutant	Electrophysiological response				Fluorescence quenching response							Fluorescence/ Electrophysiology			
	bimane labeled				in detergent solution										
	pH ₅₀	n _H	n	ΔpH ₅₀	pH ₅₀	F ₀	ΔF _{MAX}	n _H	n	ΔpH ₅₀		ΔpH ₅₀			
Bim136-Q101W C27S	5.42 ± 0.08	2.68 ± 0.33	10	Ref	5.85 ± 0.21	0.71 ± 0.03	0.45 ± 0.06	0.77 ± 0.18	17	Ref	-	0.43	***		
+E26Q	4.83 ± 0.12	2.98 ± 0.64	6	- 0.59	****	5.28 ± 0.34	0.53 ± 0.02	0.22 ± 0.02	1.13 ± 0.27	4	- 0.57	**	-	0.45	*
+Y28F	3.88 ± 0.08	2.63 ± 0.68	3	- 1.54	****	3.68 ± 0.34	0.70 ± 0.01	0.38 ± 0.09	< 3	3	- 2.17	****	-	- 0.2	***
+Y28F & C27	5.34 ± 0.11	2.03 ± 0.12	6	- 0.08	ns	ND	ND	ND	ND	-	-	-	-	-	-
+ D32E	4.65 ± 0.12	2.62 ± 1.51	6	- 0.77	****	5.52 ± 0.05	0.68 ± 0.02	0.38 ± 0.01	0.75 ± 0.05	3	- 0.33	ns	-	0.87	***
+E222Q	4.68 ± 0.09	2.51 ± 0.33	5	- 0.74	****	5.36 ± 0.14	0.66 ± 0.03	0.40 ± 0.04	0.74 ± 0.18	3	- 0.49	*	-	0.68	***
+H235Q	4.04 ± 0.21	1.19 ± 0.31	6	- 1.38	****	5.00 ± 0.09	0.70 ± 0.01	0.42 ± 0.01	0.78 ± 0.10	3	- 0.85	****	-	0.96	***
+Propofol	5.16 ± 0.13	= 2.5	3	- 0.26	*	5.33 ± 0.06	0.67 ± 0.02	0.38 ± 0.01	1.21 ± 0.21	4	- 0.52	**	-	0.17	ns
+H235Q & propofol	4.71 ± 0.15	1.53 ± 0.48	6	- 0.71	****	5.67 ± 0.14	0.70 ± 0.01	0.43 ± 0.01	1.25 ± 0.04	3	- 0.18	ns	-	0.96	***
+H235F	NF	NF	3	-	-	5.25 ± 0.08	0.70 ± 0.05	0.38 ± 0.04	1.06 ± 0.17	3	- 0.60	**	-	-	-
+L157A	NF	NF	3	-	-	5.42 ± 0.65	0.67 ± 0.01	0.19 ± 0.09	0.71 ± 0.46	4	- 0.43	*	-	-	-
+L246A	NF	NF	3	-	-	4.87 ± 0.14	0.65 ± 0.01	0.24 ± 0.01	0.79 ± 0.12	3	- 0.98	****	-	-	-
Bim250-Y197	4.66 ± 0.18	2.20 ± 0.54	12	-0.76	****	5.83 ± 0.17	0.59 ± 0.04	0.33 ± 0.09	1.19 ± 0.28	8	- 0.02	ns	Ref	1.17	***
+H235F	NF	NF	3	-	-	5.40 ± 0.13	0.54 ± 0.01	0.20 ± 0.01	1.16 ± 0.15	4	-	-	0.43	**	-
+L157A	NF	NF	3	-	-	5.81 ± 0.19	0.49 ± 0.06	0.45 ± 0.07	0.64 ± 0.19	3	-	-	0.02	ns	-
+L246A	NF	NF	3	-	-	5.53 ± 0.03	0.64 ± 0.01	0.30 ± 0.01	1.69 ± 0.29	3	-	-	-0.3	*	-

1140 **Table 1. pH-dependence of electrophysiological and fluorescence quenching**
1141 **responses.** pH₅₀ and Hill coefficient n_H average and standard deviation values are
1142 shown after individual fitting of each measurement. n correspond to the number of
1143 oocytes for electrophysiology and the number of fluorescence measurements,
1144 each measurement including values for a full pH range. F₀ corresponds to the
1145 initial fluorescence value at pH 7/8 and ΔF_{max} the maximum variation in
1146 fluorescence amplitude within the pH range (absolute values). To reasonably fit
1147 Bim136-Q101W + propofol current and Bim136-Q101W-Y28F fluorescence, Hill
1148 coefficients have been constrained to 2.5 and below 3 respectively. ΔpH₅₀s are
1149 calculated between mutants and their parent construct Bim136-Q101W or Bim250-
1150 Y197 (labeled Ref). Their significance was calculated with a one-way ANOVA test
1151 using a Dunnett's multiple comparisons test. The p-value is significantly different
1152 with p-value ≤ 0.0001 (****), ≤ 0.001 (***), ≤ 0.01(**), ≤ 0.05 (*) or not significantly
1153 different when p-value > 0.05 (ns). NF stands for non-functional and ND for not
1154 determined. To compare electrophysiological pH₅₀ and fluorescence pH₅₀ for each
1155 mutant (right column), unpaired t tests were done with two-tailed p-value and 95%
1156 confidence intervals.
1157

1158 **FIGURES LEGENDS**

1159 **Figure 1. Electrophysiological and fluorescence characterization of the**
1160 **quenching pairs of GLIC.** (A) Scheme for GLIC activation, showing first a pre-
1161 activation step involving full compaction of the ECD and motion of the M2- M3 loop
1162 as monitored by fluorescence, followed by a pore opening step. Blue spheres
1163 indicate the location of sensors Bim136 and Bim250 used thereafter in this study.
1164 (B) GLIC-pH 4 (pdb code 4HFI) structure side view, the light blue rectangle
1165 represents the position of the membrane. Quenching pairs generated in our
1166 previous study (Menny et al., 2017) are highlighted: blue spheres show the C α of
1167 the residues that were mutated into cysteines and bimeane labeled (Bim33,
1168 Bim133, Bim135, Bim136 and Bim250), black spheres show the C α of the
1169 quenchers (W160, L103W, W72, Q101W and Y197). Bim136 and Bim250 are
1170 shown in dark. (C) pH-dependent response curves of Bim136 and Bim250
1171 sensors, by electrophysiology after labeling (top panel) and with bimeane
1172 fluorescence quenching (lower two panels). Fluorescence data are shown
1173 normalized to the fluorescence of the denatured protein (F_{SDS}), bimeane
1174 fluorescence is shown without quencher (\circ) and in presence of the quencher (\bullet).
1175 **Figure 1-Supplementary 1. Fluorescence quenching data from mutants with**
1176 **the Bim135 W72 sensor.** (A) Structure of two monomers of GLIC pH 4 showing in
1177 spheres the position of the sensor Bim135-W72 and of the different mutants test-
1178 ed. Propofol is shown in sticks in its known binding sites. (B) pH dependent re-
1179 sponse in fluorescence quenching of Bim135 in presence and absence of the
1180 quencher W72 demonstrating it is the main cause of Bim135 quenching. (C) Nor-
1181 malized pH-dependent curves in electrophysiological response (black) and fluo-
1182 rescence quenching (blue) showing that fluorescence pH₅₀ is higher than current
1183 pH₅₀ as in the other sensors shown in Figure 1-Supplementary 2. (D) and (E) show
1184 the effect of H235F and L157A mutations on Bim135-W72 fluorescence quench-
1185 ing. (F) and (G) show the effect of propofol on Bim135-W72 (+/- H235Q) fluo-
1186 rescence quenching. **Conclusion on Bim135-W72:** We unambiguously identify here
1187 Trp72 as the endogenous quenching residue of Bim135 since the mutant Bim135-
1188 W72F is functional in electrophysiology, but does not undergo pH-dependent
1189 quenching. The pH-dependent changes in fluorescence show a bell-shaped curve
1190 suggesting complex changes in distances at this level. When combined with
1191 Bim135-W72, L157A shows a decrease in pH₅₀ of the first quenching component,

1192 and a diminished amplitude of the second unquenching component. Combined
1193 with Bim135-W72, H235F and H235Q display a phenotype with a notably much
1194 smaller amplitude of the first component. On Bim135-W72, propofol causes a de-
1195 crease in pH_{50} for the first quenching component. On Bim135-W72-H235Q,
1196 propofol restores a WT-like pH-dependent quenching curve. The observed global
1197 lower amplitude of the Bim135-W72 H235Q/F quenching curves may either result
1198 from a decrease in the extent of the reorganization responsible for the amplitude of
1199 first component, or a rightward shift of the curve resulting in an overlap which
1200 would result in an averaging of the bimane quenching and unquenching curves.
1201 Therefore, the fluorescence data related to the Bim135-W72 pair cannot be inter-
1202 preted in simple terms, although they further document the strong allosteric cou-
1203 pling between mutations and propofol binding and the upper part of the ECD.

1204 **Figure 1-Supplementary 2. pH-dependent curves comparison.** Normalized pH-
1205 dependent curves in electrophysiological response (black) and fluorescence
1206 quenching (blue) showing that fluorescence pH_{50} is higher than current pH_{50} for
1207 both sensors Bim136-Q101W and Bim250-Y197. For the fluorescence quenching
1208 data, the value at neutral pH is set to 0 and values are then normalized to the val-
1209 ue displaying the maximal change in fluorescence.

1210 **Figure 1-Source data 1. Fluorescence quenching and electrophysiological**
1211 **current measurements of the different mutants tested.**

1212 **Figure 2. Allosteric coupling within the ECD.** (A) Structure of two monomers of
1213 GLIC pH 4 (4HFI) showing positions of the fluorescence sensor (Bim136-Q101W)
1214 and the two mutated residues at the bottom of the ECD resulting in a partial loss of
1215 function. The lower panel shows a zoom on the interface with E26 and Y28
1216 residues and their interactions with surrounding residues and a network of water
1217 molecules (blue spheres). (B) Electrophysiological recordings in oocytes of the
1218 mutants labeled with bimane showing shifted responses to higher proton
1219 concentrations in comparison with GLIC Bim136 -Q101W. pH applications are
1220 shown above each trace and the horizontal scale represents 1 minute of
1221 recording. Graphs represent pH-dependent curves showing a shift to higher proton
1222 concentrations in electrophysiological responses (C) and fluorescence quenching
1223 responses (D) for both mutants.

1224 **Figure 3. Allosteric coupling between the top of the ECD and the TMD.** (A)
1225 Structure of two monomers of GLIC pH 4 (4HFI) showing positions of the

1226 fluorescence sensor (Bim136-Q101W) at the top of the ECD and three mutations
1227 distributed along the protein. Right panels show zooms on important interactions
1228 with the mutated residues. (B) Electrophysiological recordings of the 3 mutants in
1229 oocytes, labeled with bimeans. Recording of GLIC Bim136-Q101W is shown for
1230 comparison. pH applications are shown above each trace and the horizontal scale
1231 represents 1 minute of recording. pH-dependent curves for electrophysiological
1232 response (C) and fluorescence quenching (D) for the three mutants in comparison
1233 with Bim136-Q101W showing a shift to higher proton concentrations of the
1234 response for all three mutants.

1235 **Figure 4. Non-functional mutants differentially alter ECD and TMD motions.**

1236 (A) Structure of two monomers of GLIC pH 4 showing the position of the
1237 fluorescence sensors (Bim136-Q101W and Bim250-Y197) and three mutations
1238 causing a total loss of function. (B) Zooms on important re-organizations of the
1239 mutated residues between structures at pH 4 (4HFI-grey) and pH 7 (4NPQ-black).
1240 (C) Electrophysiological recordings in oocytes of the 3 mutants labeled with
1241 bimeans showing no current in comparison with GLIC presenting sensor mutations
1242 only. pH-dependent curves in fluorescence for the three mutants with the sensor
1243 Bim136-Q101W (D) and Bim250-Y197 (E).

1244 **Figure 4-Supplementary 1. Immunofluorescence microscopy data showing**

1245 **GLIC expression at the oocytes surface.** In grey is the GFP fluorescence and in
1246 blue the fluorescence resulting from GLIC immunolabeling via anti-HA antibody.
1247 The scale and exposure time are the same for all images.

1248 **Figure 5. Allosteric coupling between the top of the ECD and propofol**

1249 **binding.** (A) Structure of two monomers of GLIC pH 4 showing positions of the
1250 fluorescence sensor Bim136-Q101W at the top of the ECD and three propofol
1251 binding sites intra, inter-subunit and in the pore identified by X-ray crystallography
1252 (Fourati et al., 2018). (B) Example of electrophysiological response to 100 μ M
1253 propofol during a low pH application (scale bars represent 100 nA and 30 sec). (C)
1254 Electrophysiological pH-dependent curves of Bim136-Q101W with and without the
1255 H235Q mutation showing inhibition and potentiation respectively. (D) Effect of 100
1256 μ M propofol on fluorescence quenching without (top panel) and with H235Q
1257 mutation (lower panel) for the Bim136-Q101W sensor.

1258 **Figure 6. The 3-state MWC model fits experimental data for Bim136Q101W**

1259 **mutants.** (A) Scheme showing the 3 states and parameters of the model. (B) Ta-

1260 ble with multiplication factors of isomerization constants for pre-activation and acti-
1261 vation as compared to Bim136-Q101W. For the Bim136-Q101W-H235Q in pres-
1262 ence of propofol, the multiplication factors are given in comparison with Bim136-
1263 Q101W-H235Q. Isomerization constants of Bim136-Q101W and Bim136-Q101W-
1264 H235Q are shown above the table (see full table in Figure 6-Source data 1). (C)
1265 Superposition of experimental data points and theoretical curves. Data points
1266 shown as spheres correspond to fluorescence intensities normalized on FSDS in
1267 blue, and to electrophysiological response normalized to the maximal current in
1268 black (except H235Q without propofol for which values were normalized to the
1269 values in the presence of propofol). Theoretical curves: the population of A state is
1270 shown in black lines and the fluorescence curve (blue line) is calculated from the
1271 sum of the 3 states' fractional populations weighted by their intrinsic fluorescence
1272 intensity (see formula in methods section). For each mutant, the fit from Bim136-
1273 Q101W (Bim136-Q101W-H235Q for the last panel) is shown in dotted blue and
1274 black lines for a visual comparison and arrows are illustrating the shift in pH_{50} .

1275 **Figure 6-Supplementary 1. Workflow for fitting experimental data using the**
1276 **MWC model.** The chart is showing the main assumptions and steps to establish
1277 parameters of the MWC model in order to fit the data.

1278 **Figure 6-Supplementary 2. A simplified 2 states MWC model to fit the total**
1279 **loss of function mutant H235F.** (A) 2 states model and parameters used in the
1280 model and their fixed values. (B) Superposition of experimental data points (flu-
1281 orescence quenching normalized on F_{SDS}), and theoretical fluorescence curve (blue
1282 line) calculated from the 2 states weighted by their intrinsic fluorescence intensity.

1283 **Figure 6-Source data 1. Summary of isomerization constant set for each mu-**
1284 **tant.** To test the robustness of the fitting, the model was tested starting with the
1285 isomerization constant of L_{pA} from Bim136-Q101W-H235F set at 100, 1000 or
1286 100,000. The multiplication factor is calculated in comparison with Bim136-Q101W
1287 constants except for H235Q + propofol (compared to Bim136-Q101W-H235Q) and
1288 mutations on Bim250-Y197 sensor background (compared to Bim250-Y197). L_{pA}
1289 constant was averaged on the 3 L_{pA} values. Affinity constants used for the second
1290 binding site were $K'_R = 5 \times 10^{-5}$; $K'_{pA} = 5 \times 10^{-5}$ and $K'A = 5 \times 10^{-6}$, affinity constants
1291 of the first binding site are shown in the table for the different L_{pA} values and fluo-
1292 rescence values for each state are indicated in Figure 6-Supplementary 2. To as-

1293 sess how well our model fits the experimental values, the determination coefficient
1294 (R^2) was calculated for each mutant with the different L_{pA} and corresponding affini-
1295 ties. R^2 were calculated for both fluorescence quenching (R^2 Fluo) and electro-
1296 physiological response (R^2 current).

1297 **Figure 7. The 3-state MWC model fits experimental data for total loss of func-**
1298 **tion mutants.** Data are presented as in Figure 6. (A) Multiplication factors of
1299 isomerization constants for pre-activation and activation of total loss of function
1300 mutants as compared to sensors Bim136-Q101W and Bim250-Y197. (B) Super-
1301 position of experimental data points and theoretical curves. Data points (in
1302 spheres) correspond to fluorescence intensities normalized on F_{SDS} in blue, and to
1303 electrophysiological response normalized to the maximal current in black. Theoret-
1304 ical curves: the population of A state is shown in black lines for sensors and the
1305 fluorescence curve (blue line) is calculated from the sum of the 3 states' fractional
1306 populations weighted by their intrinsic fluorescence intensity. For each mutant, the
1307 fit from the associated sensors (Bim136-Q101W or Bim250 Y197) is shown in dot-
1308 ted lines for a visual comparison and arrows are illustrating the shift in pH_{50} .

1309 **Figure 8. Two distinct trajectories for GLIC activation computed using**
1310 **iMODfit.** (A) RMSD evolution throughout the frames of A and B trajectories
1311 against GLIC structures at pH 4 (●); pH 7 (▲), pdb codes are 4HFI and 4NPQ
1312 respectively. Both trajectories are shown with frame 1 being the closest to GLIC-
1313 pH 7. (B) Twist angle measured throughout the frames on both trajectories. The
1314 twist angle is measured by the angle formed between vectors from the centers of
1315 mass of the ECD and TMD as defined in (Calimet et al., 2013). Each trace
1316 corresponds to the trajectory of a single subunit within the pentamer.

1317 **Figure 9. Key TMD motions in trajectories A and B.** (A) Snapshots of GLIC
1318 TMD top view in the first and last frame of the A trajectory with a Bim250-Y197
1319 quenching pair modeled at one interface. Bimane is shown in blue and Y197 in
1320 black spheres. One subunit is shown in grey, the others are in white, the M2-M3
1321 loop is shown in blue and the loop 2 from ECD is shown in purple for one subunit.
1322 Atoms used for measurements are shown in pale blue spheres and distances are
1323 indicated in angstroms. (B) Pore radius measured at the Ile233 level. (C) Intra-
1324 subunit separation of M2 and M3 helices measured between atoms indicated.
1325 Points at positions 0 and 13 are the distances measured in pH 4 and pH 7 X-ray
1326 structures. (D) Inter-subunit distances showing M2-M3 loop outward motion at the

1327 Pro250-Tyr197 level (top panel) and between bimane and Tyr197 centroids
1328 (bottom panel) in both trajectories A and B.

1329 **Figure 10. Key ECD motions in trajectories A and B.** (A) Snapshots of two
1330 subunits of GLIC ECD in the first and last frame of the A trajectory with a Bim136-
1331 Q101W quenching pair modeled at the interface. One subunit is shown in grey, the
1332 other in white with sheets of the β -sandwich shown in dark and light purple;
1333 Bimane is shown in blue and Trp101 in black spheres; C_α and C_β atoms used for
1334 measurements are shown in pale blue spheres and distances are indicated in
1335 angstroms. Inter-subunit distances showing ECD compaction measured at the
1336 Asp136-Gln101 level (B) and between bimane and Q101W centroids (C) in both
1337 trajectories A and B. Points at frames 0 and 13 are the distances in pH 4 and pH 7
1338 X-ray structures. (D) Intra-subunit distance showing contraction at the bottom of
1339 the β -sandwich measured by C_α distances between Asp32 and Gly159.

1340 **Figure 10-Supplementary 1. Evolution of ECD inter-subunits distance**
1341 **Arg133-Leu103 at the top of the ECD in iMODfit trajectories.** (A) Snapshots of
1342 two subunits of GLIC ECD in the first and last frame of the trajectory A with a
1343 Bim133-L103W quenching pair modeled. One subunit is shown in grey, the other
1344 in white with β -sheets forming the β -sandwich shown in dark and light purple;
1345 bimane is shown in blue and quencher in black spheres; C_β atoms used for meas-
1346 urements are shown in pale blue spheres and distances are indicated in ang-
1347 stroms. (B) Inter-subunit distances showing ECD compaction at the Arg133-
1348 Leu103 level (top panel) and between bimane and L103W centers of mass (bot-
1349 tom panel) in both trajectories A and B. Points at frames 0 and 13 are the distanc-
1350 es in pH 4 and pH 7 structures subunits interfaces.

1351 **Figure 10-Supplementary 2. Evolution of ECD inter-subunits distance Lys33-**
1352 **Trp160 at the bottom of the ECD in iMODfit trajectories.** (A) Snapshots of two
1353 subunits of GLIC ECD in the first and last frame of the trajectory A with Bim33-
1354 W160 quenching pair modeled. One subunit is shown in grey, the other in white
1355 with β -sheets forming the β -sandwich shown in dark and light purple; bimane is
1356 shown in blue and quencher in black spheres; C_β atoms used for measurements
1357 are shown in pale blue spheres and distances are indicated in angstroms. (B) In-
1358 ter-subunit distances showing ECD compaction at the Lys33-Trp160 level (top
1359 panel) and between bimane and W160 centers of mass (bottom panel) in both tra-

1360 jectories A and B. Points at frames 0 and 13 are the distances in pH 4 and pH 7
1361 structures subunits interfaces.

1362 **Figure 10-Supplementary 3. Evolution of Bim135-W72 orientation at the ECD**
1363 **intra- subunits in iMODfit trajectories.** (A) Snapshots of one subunit of GLIC
1364 ECD, top view in the first and last frame of the trajectory A with Bim135-W72
1365 quenching pair modeled. The adjacent subunit is shown in grey, and the main
1366 subunit is shown in white with β -sheets forming the β - sandwich shown in dark and
1367 light purple; bimane is shown in blue and quencher in black spheres. (B)
1368 Snapshots for the trajectory B. (C) Similar representation from the structure
1369 resolved by X-ray of Bim135-W72 at pH 4 (5IUX). Bimane was resolved in two out
1370 of five chains and showed a similar orientation to the one found in the last frames
1371 of both trajectories (A and B right panels). (D) Intra-subunit C_{β} distances between
1372 Val135 and Trp72 (top panel) and between Bim135 and Trp72 centers of mass
1373 (bottom panel) along the trajectories.

1374 **Conclusion:** for Bim135-W72, the distances between the centers of mass of the
1375 bimane and indole moieties are not correlated with the distances between the
1376 residue's backbone. Since at this position bimane occupies a rather buried
1377 location within the protein structure, we suggest that these discrepancies come
1378 from local reorganization of surrounding residues that are not directly correlated
1379 with the movement of the backbone. Interestingly, we previously solved the X-ray
1380 structure of Bim135-W72 at pH 4 by crystallography, which shows a similar
1381 location of the bimane moiety with that of our docking in GLIC-pH 4.

1382 **Figure 11. Effect of mutations on pre-activation and activation.** (A) One subu-
1383 nit of GLIC showing the positions of tested mutations in red spheres, with in grey
1384 the region involved in the central gating pathway identified by iModFit. (B) Multipli-
1385 cation factor shown on a log scale for each mutant to visualize how isomerization
1386 constants L_{pA} and L_A were modified in comparison with Bim136-Q101W, or for
1387 propofol (H235Q) in comparison with the same mutant without propofol.

1388

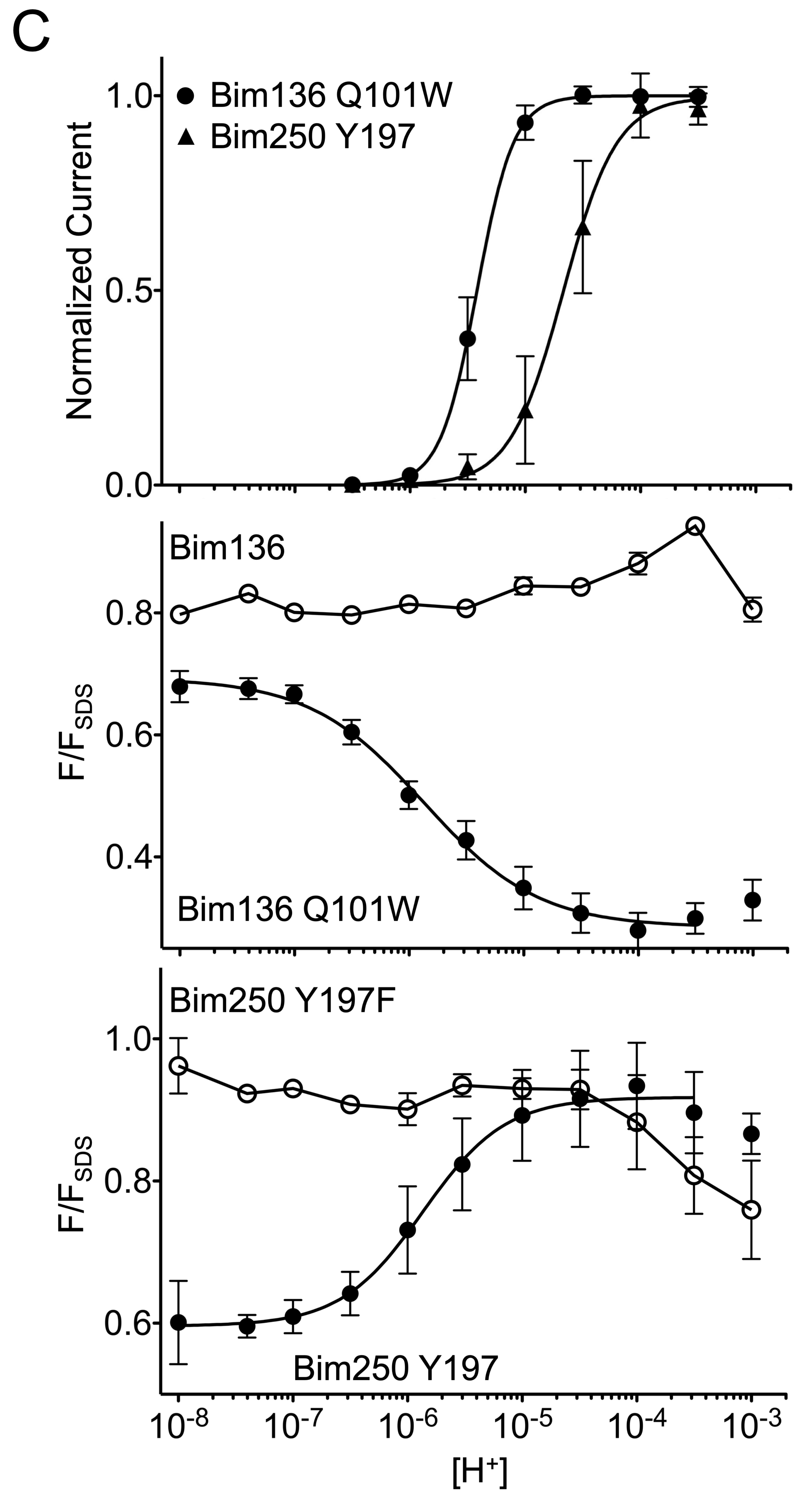
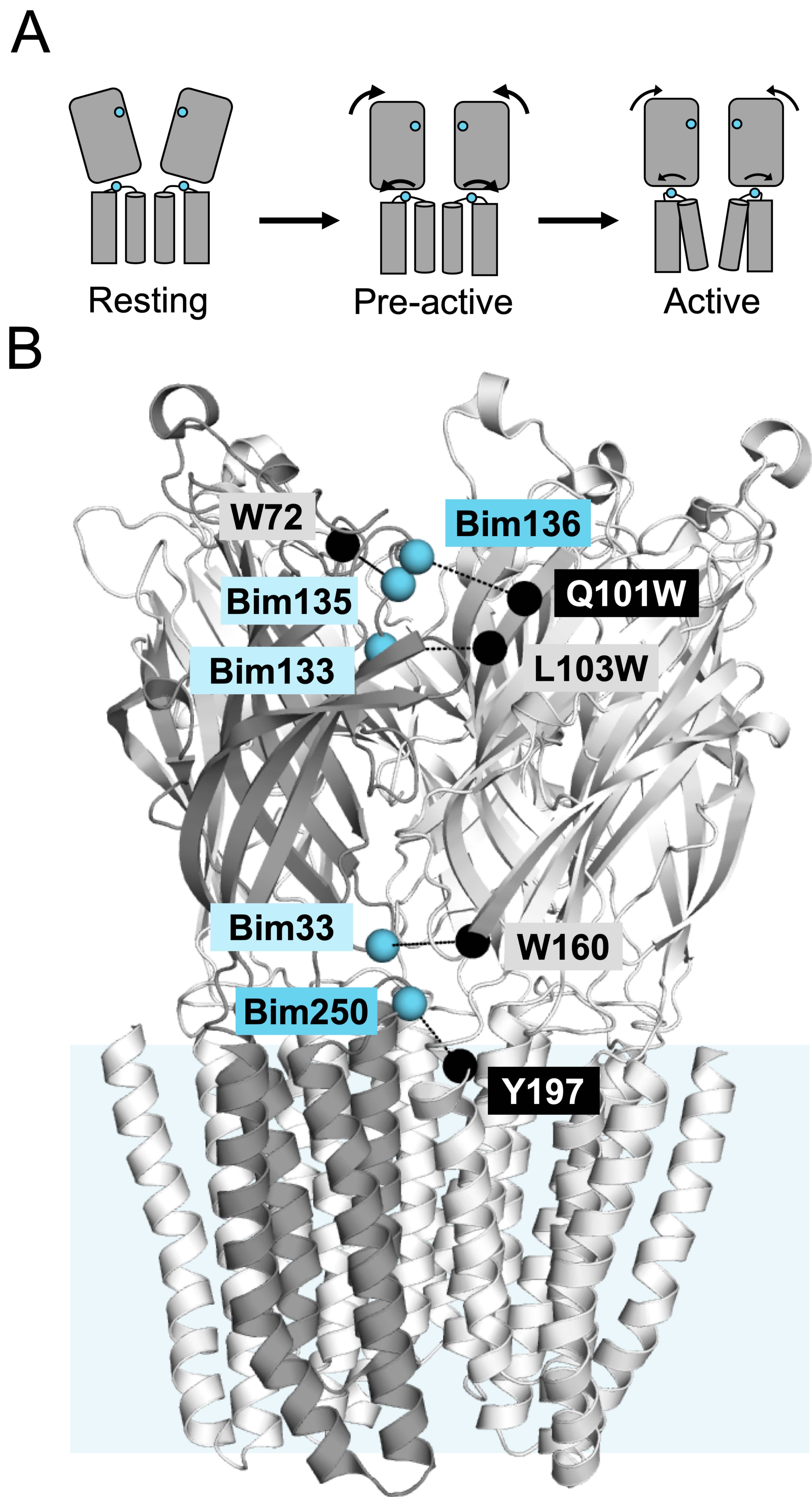


Figure 1

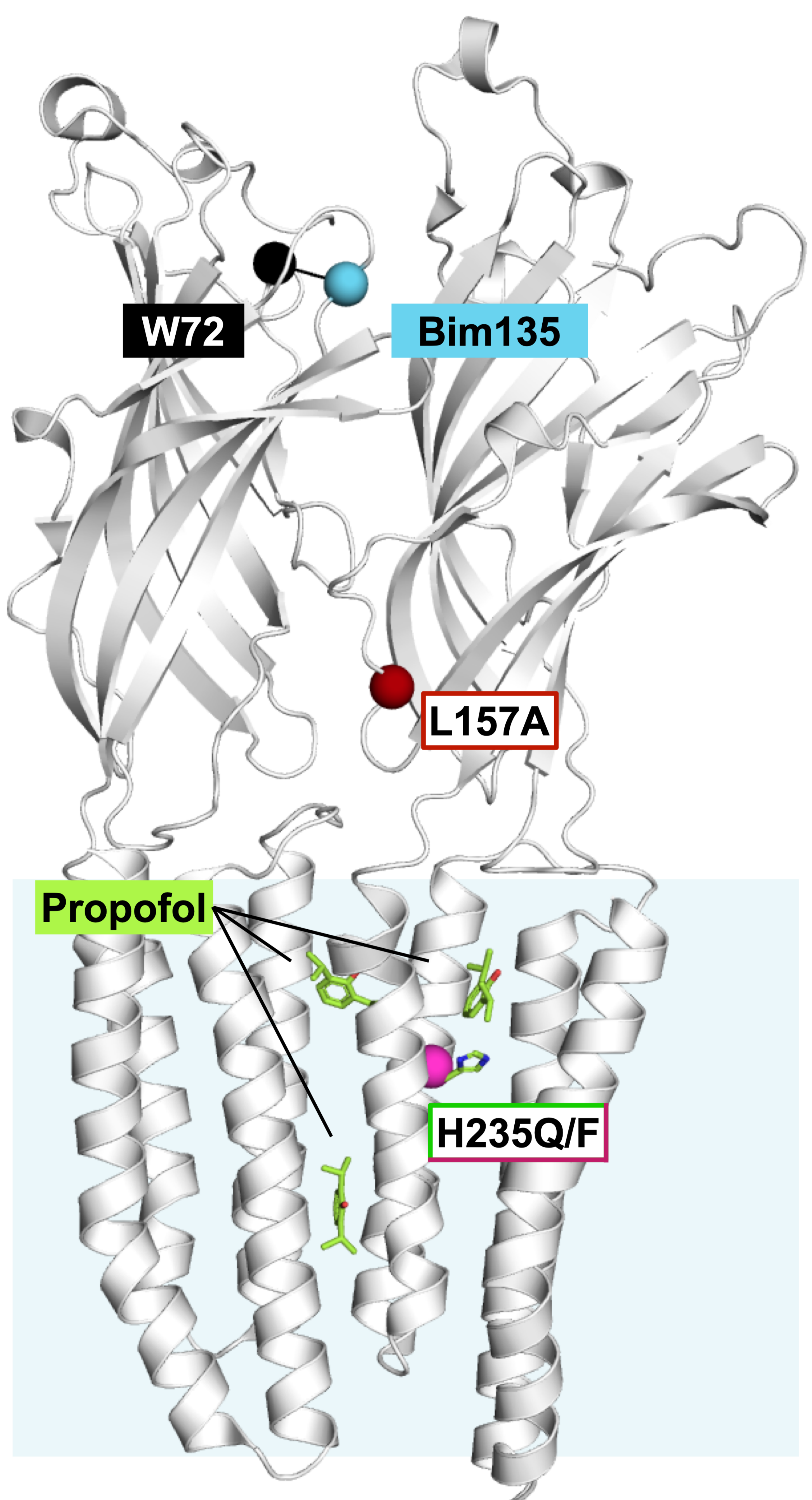
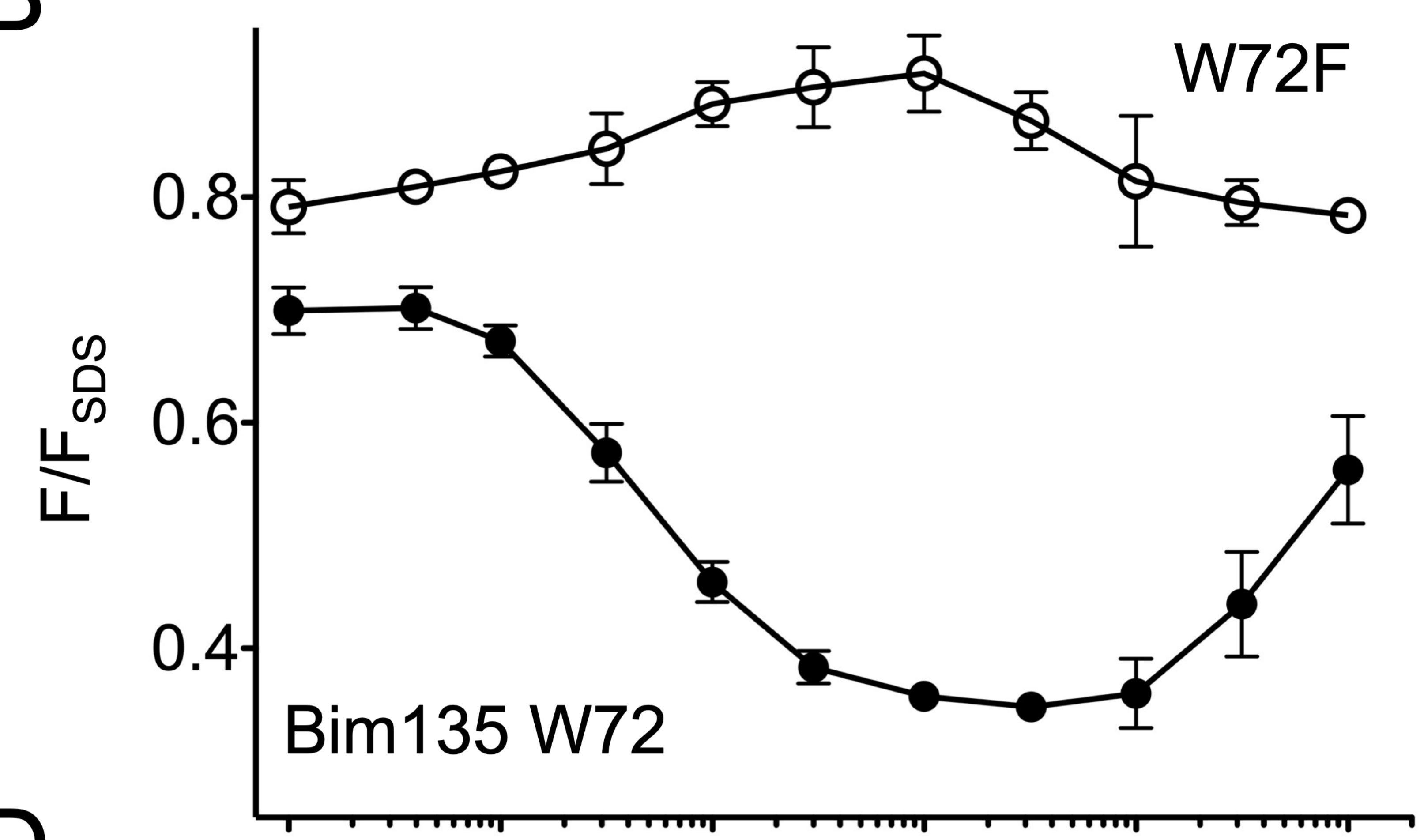
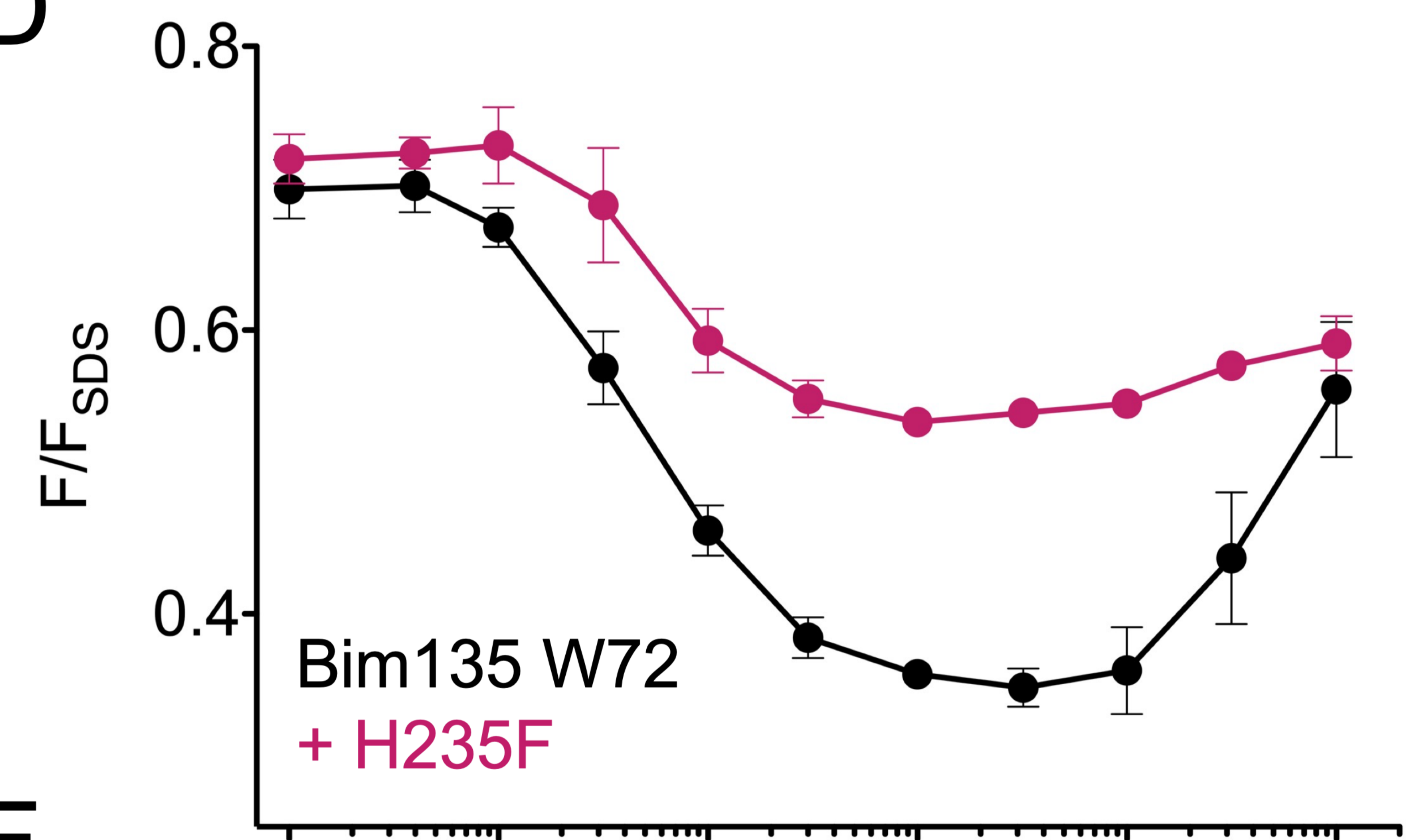
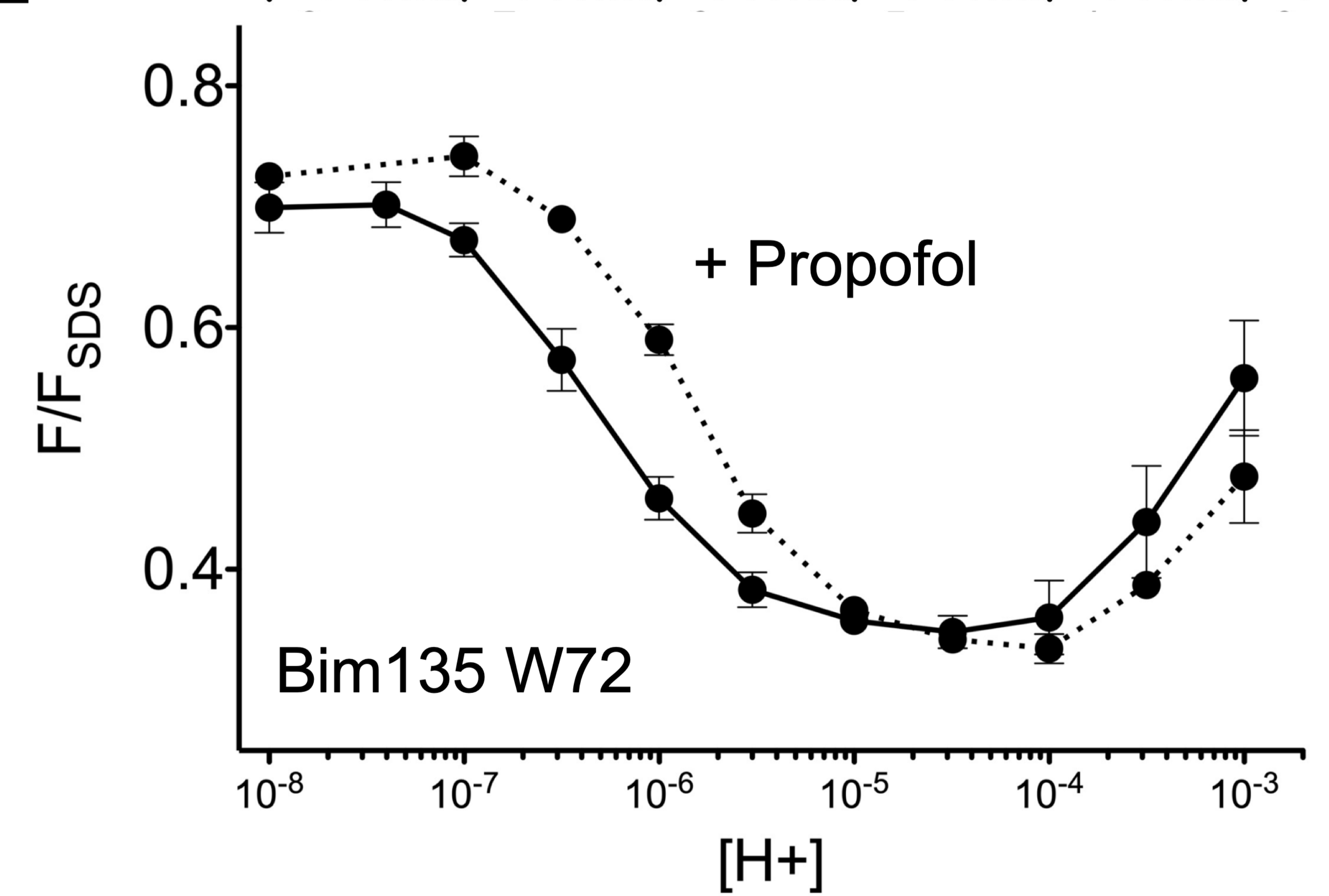
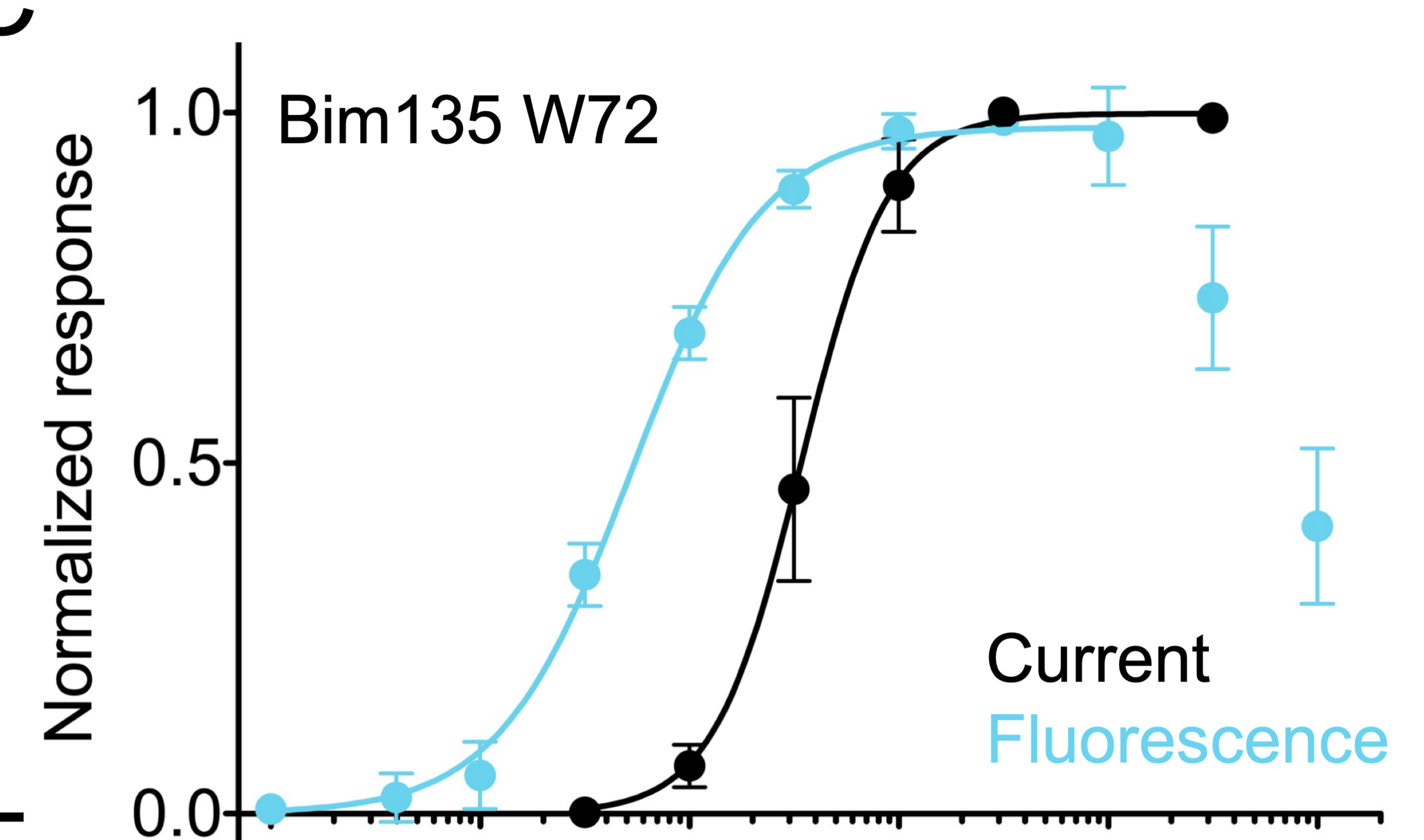
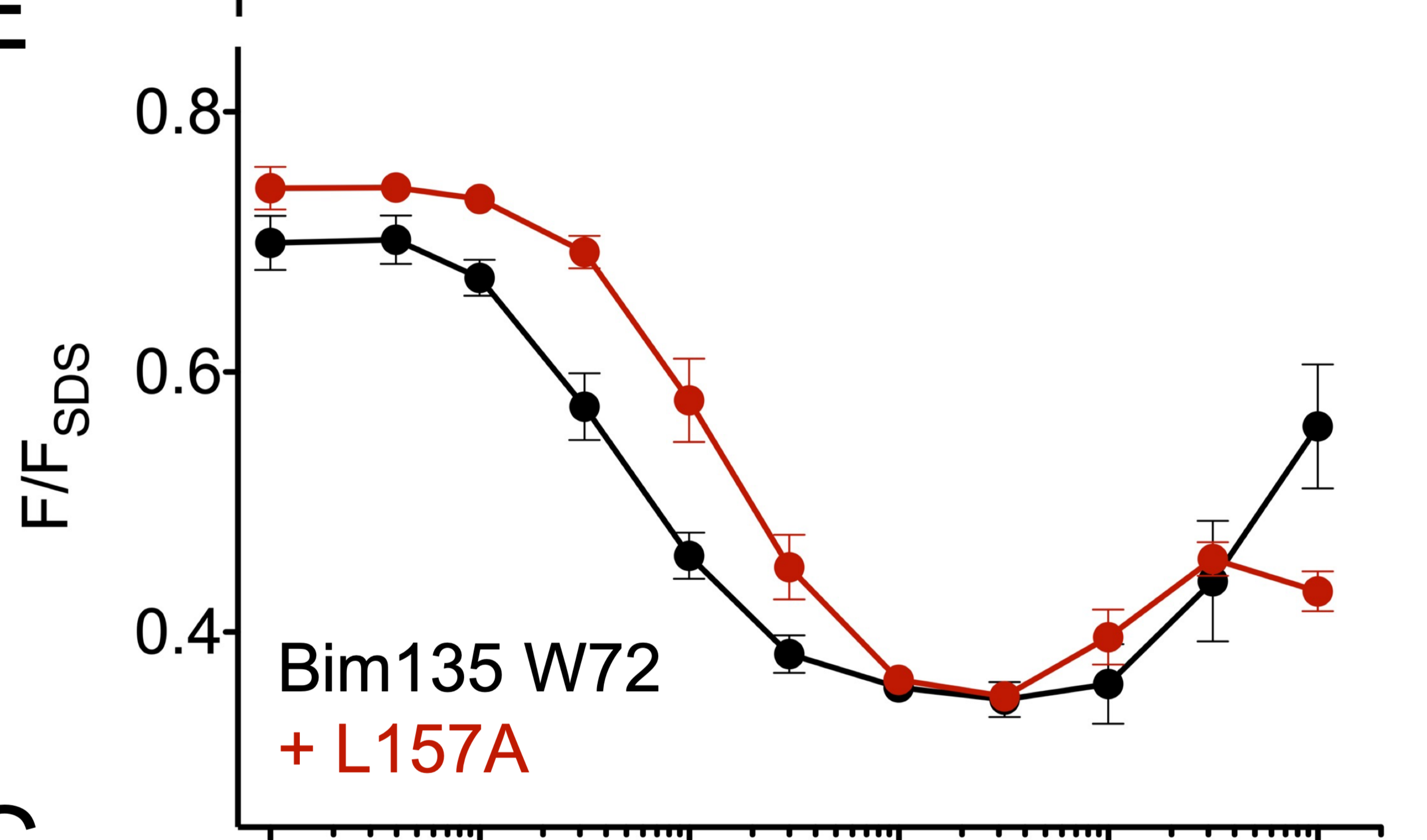
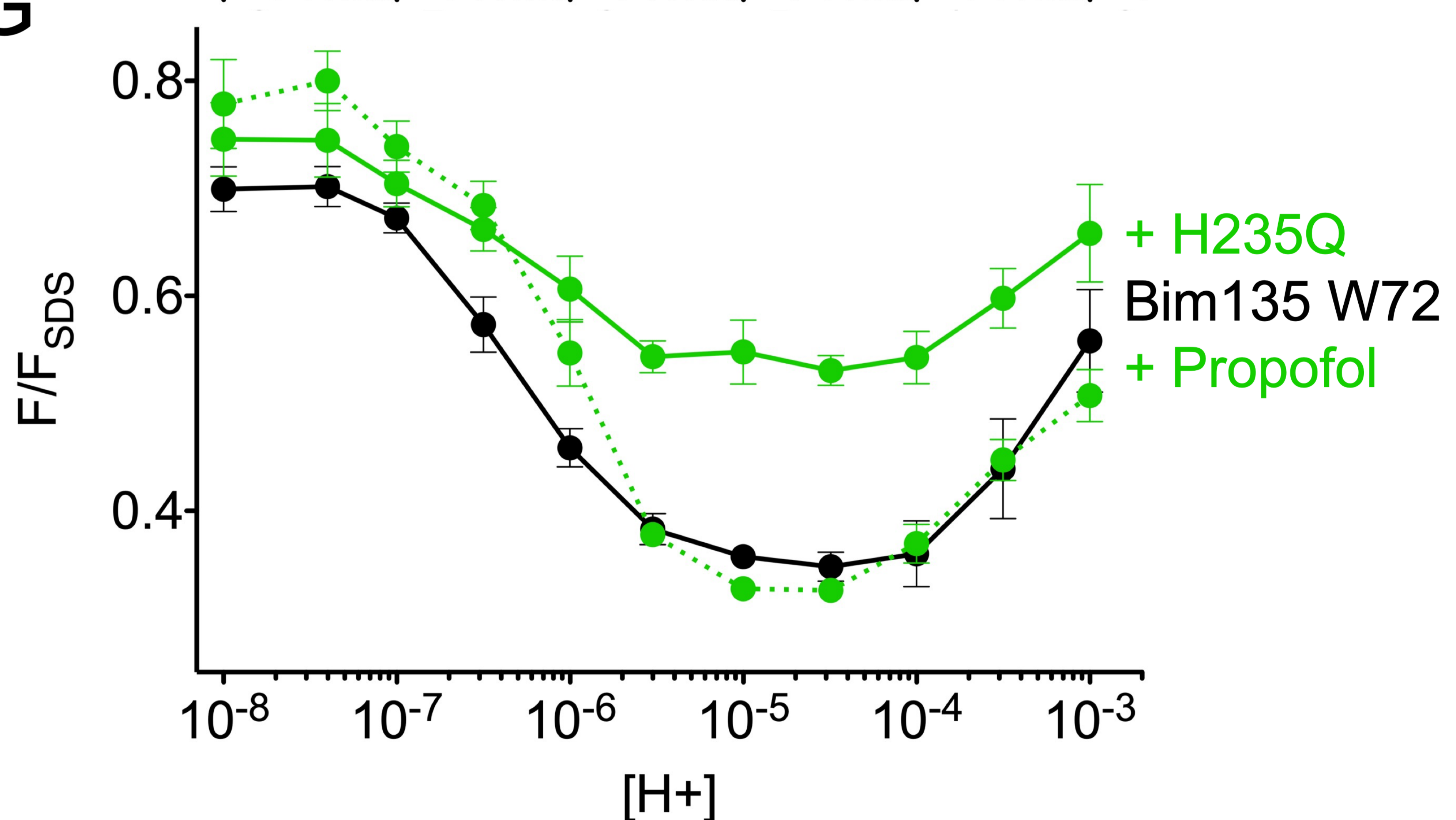
A**B****D****F****C****E****G**

Figure 1 – Supplementary 1

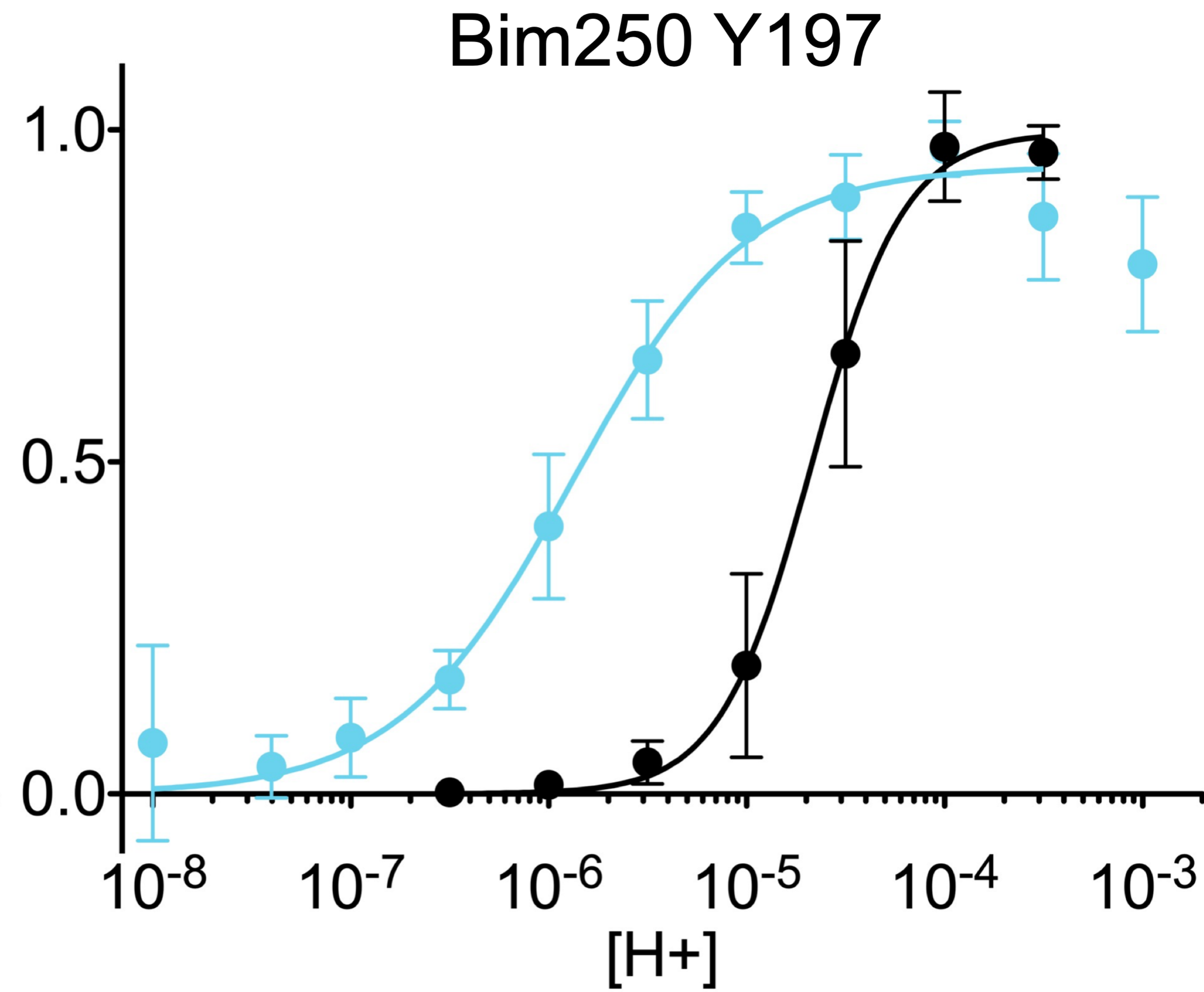
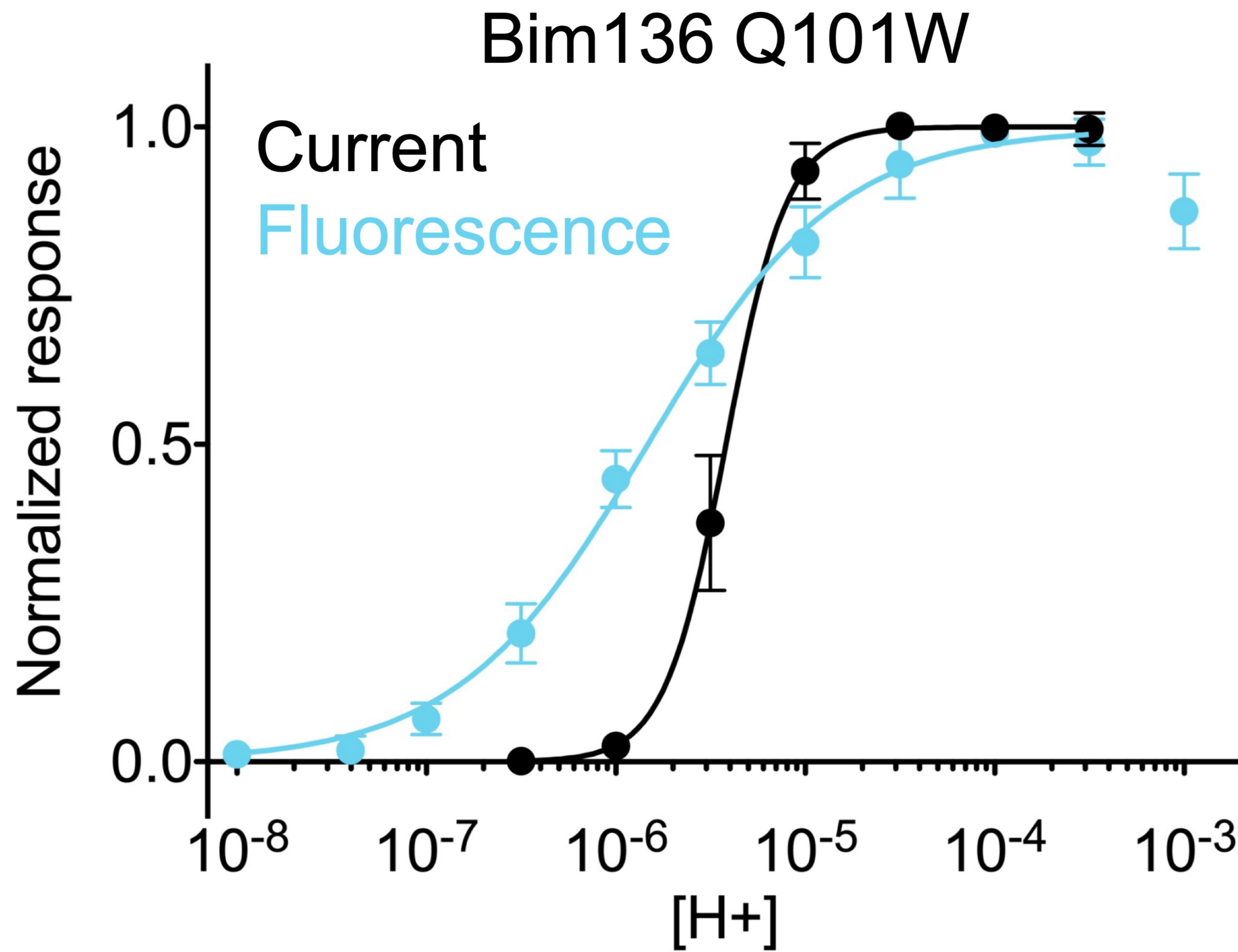
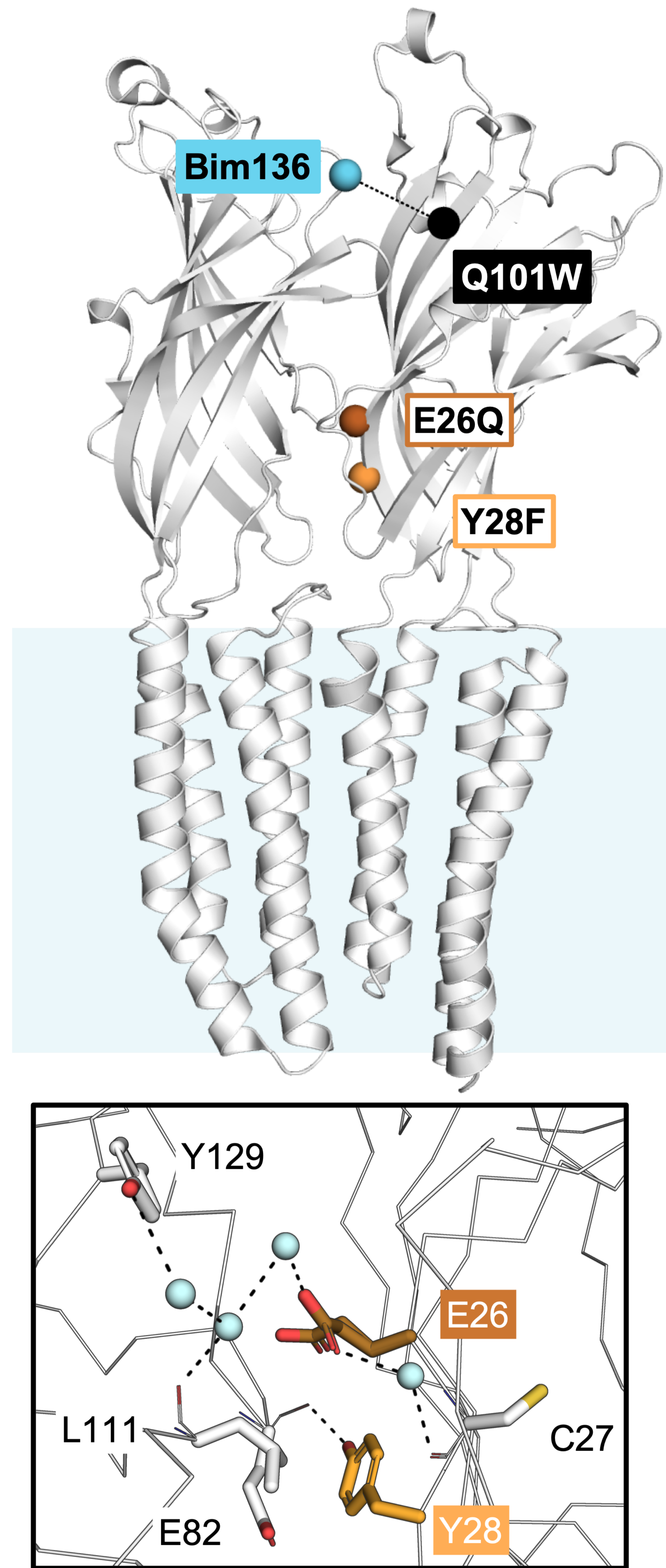
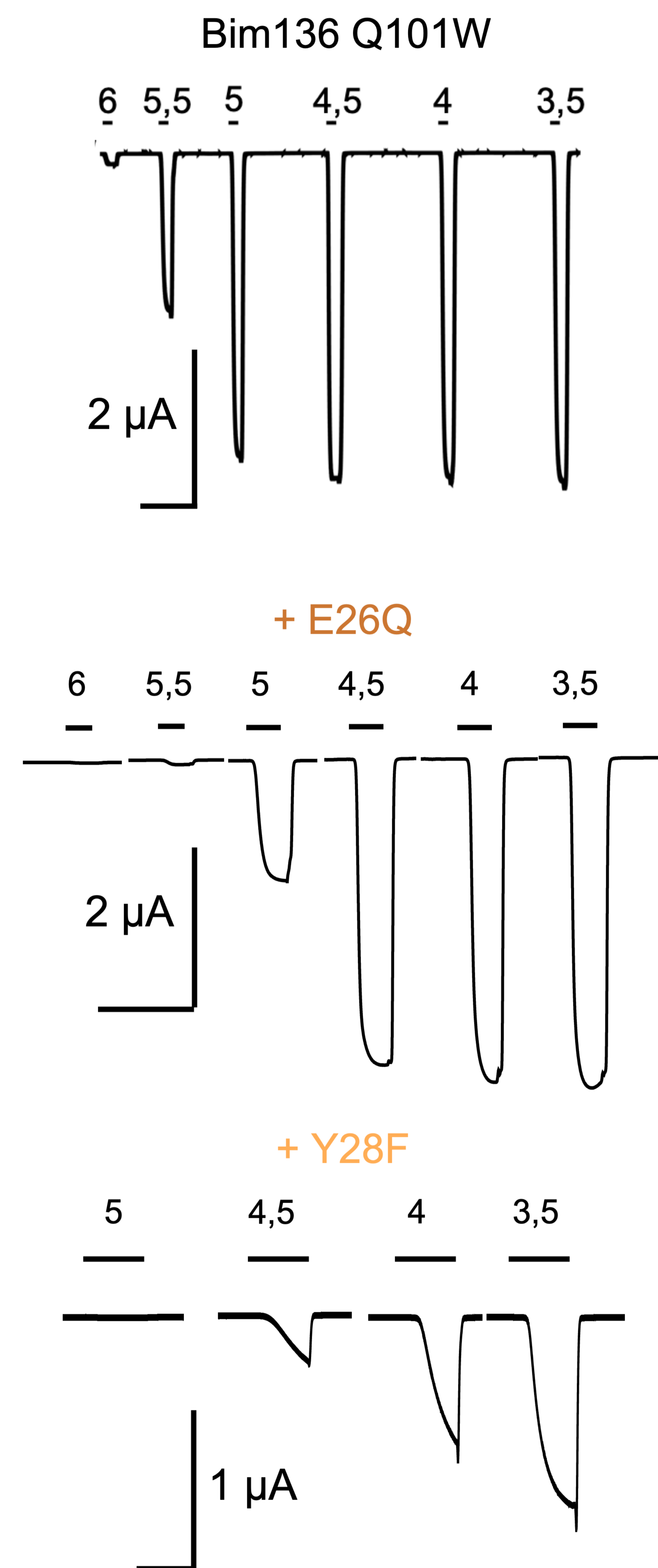


Figure 1 – Supplementary 2

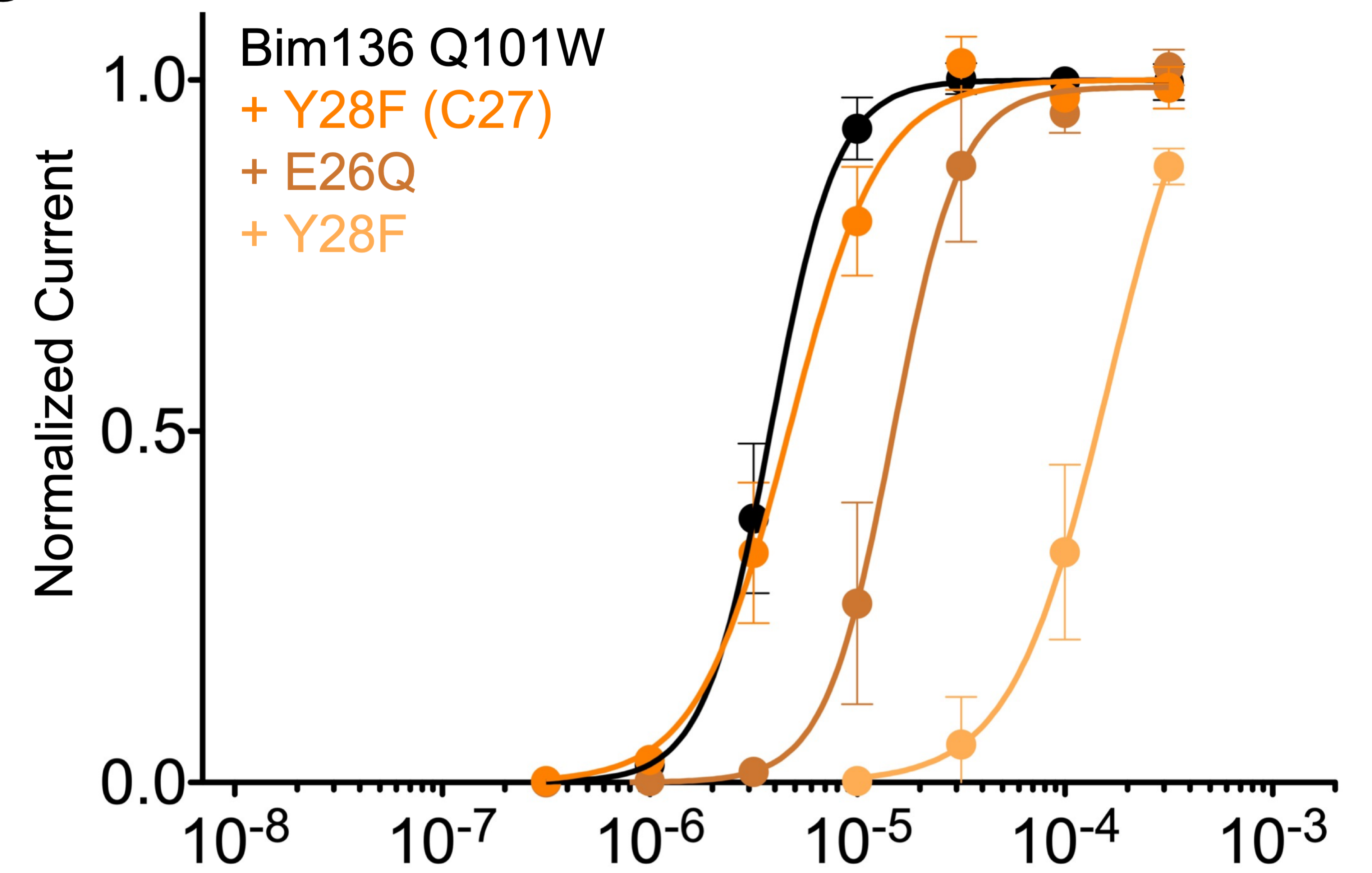
A



B



C



D

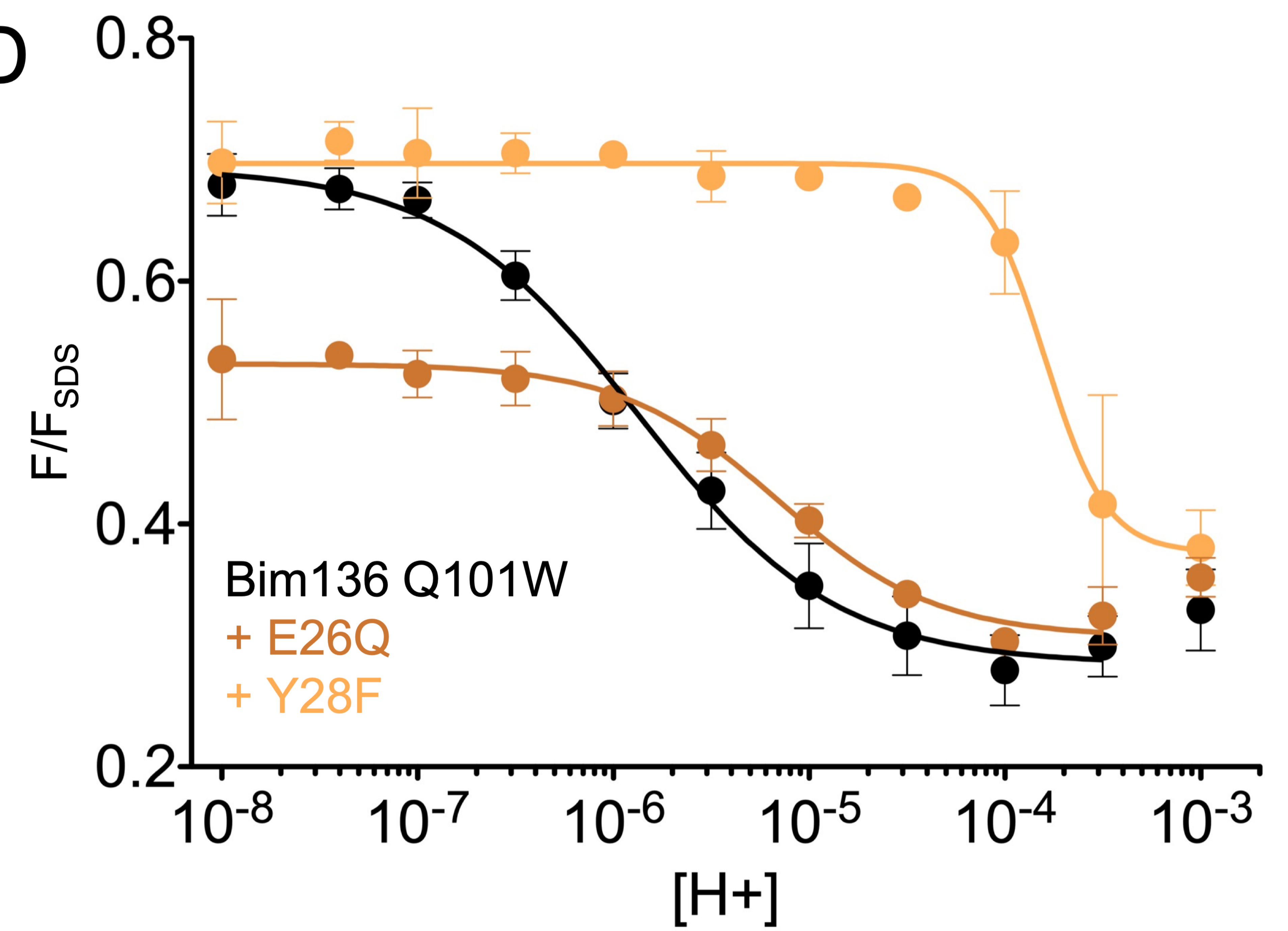
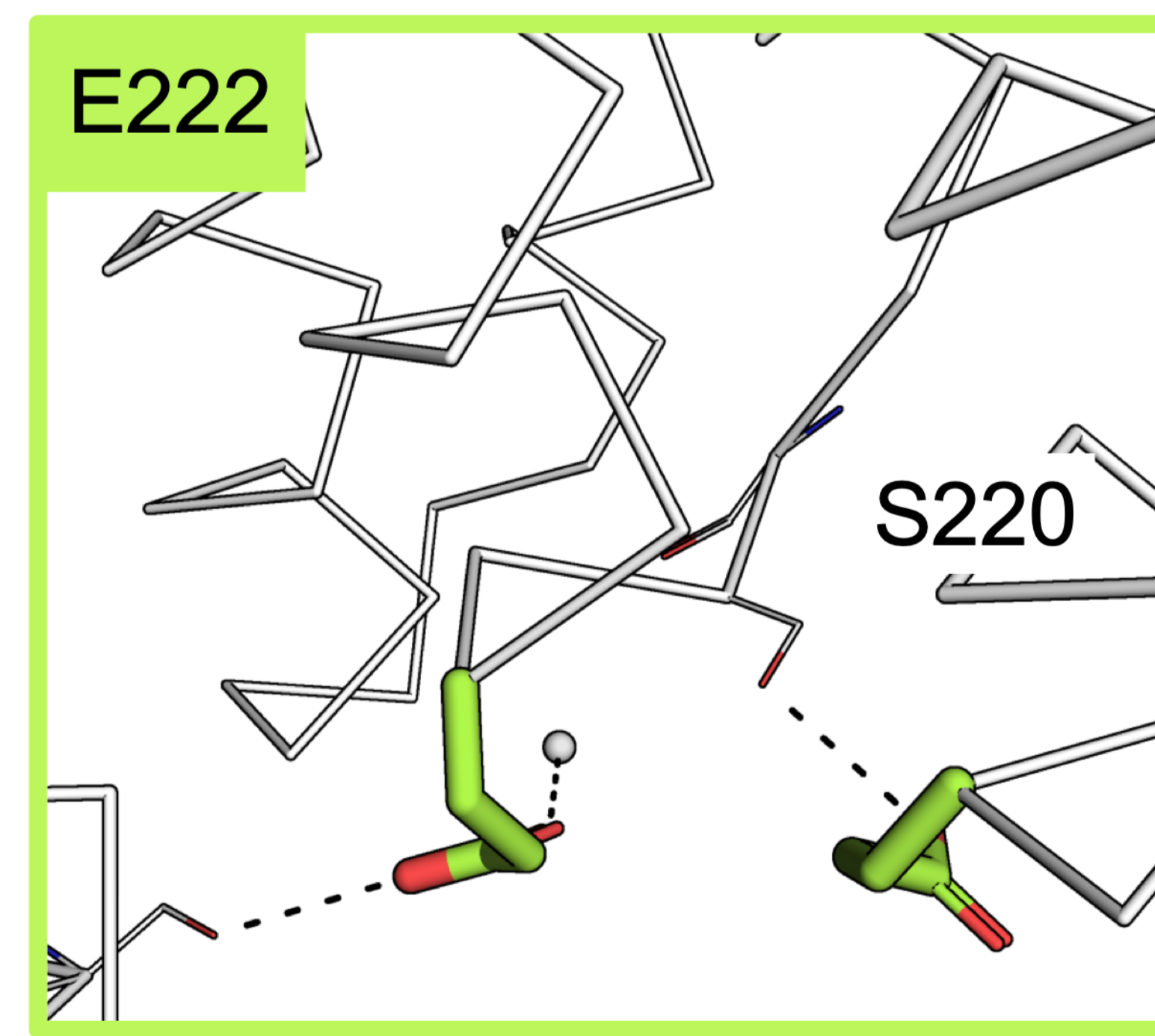
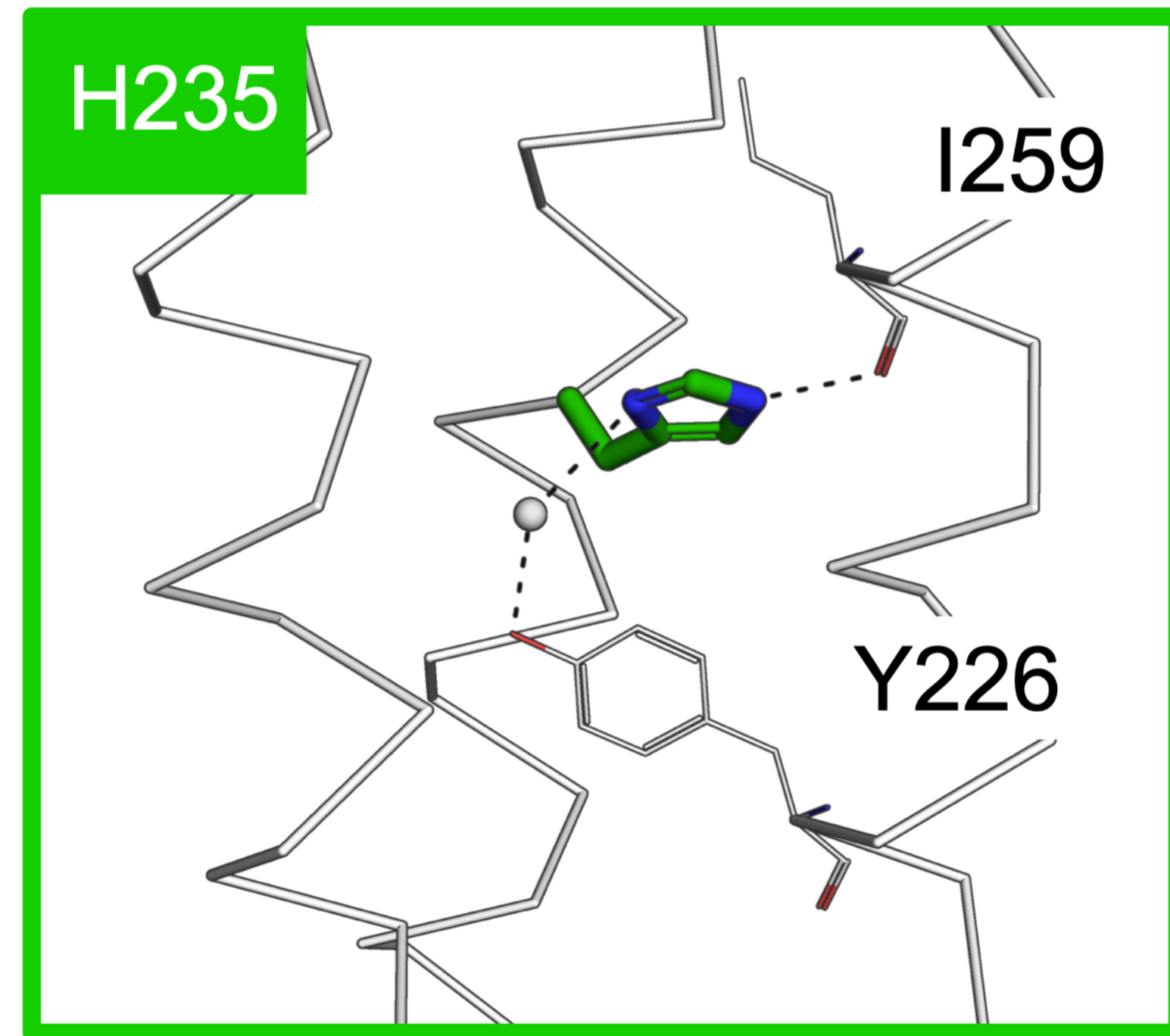
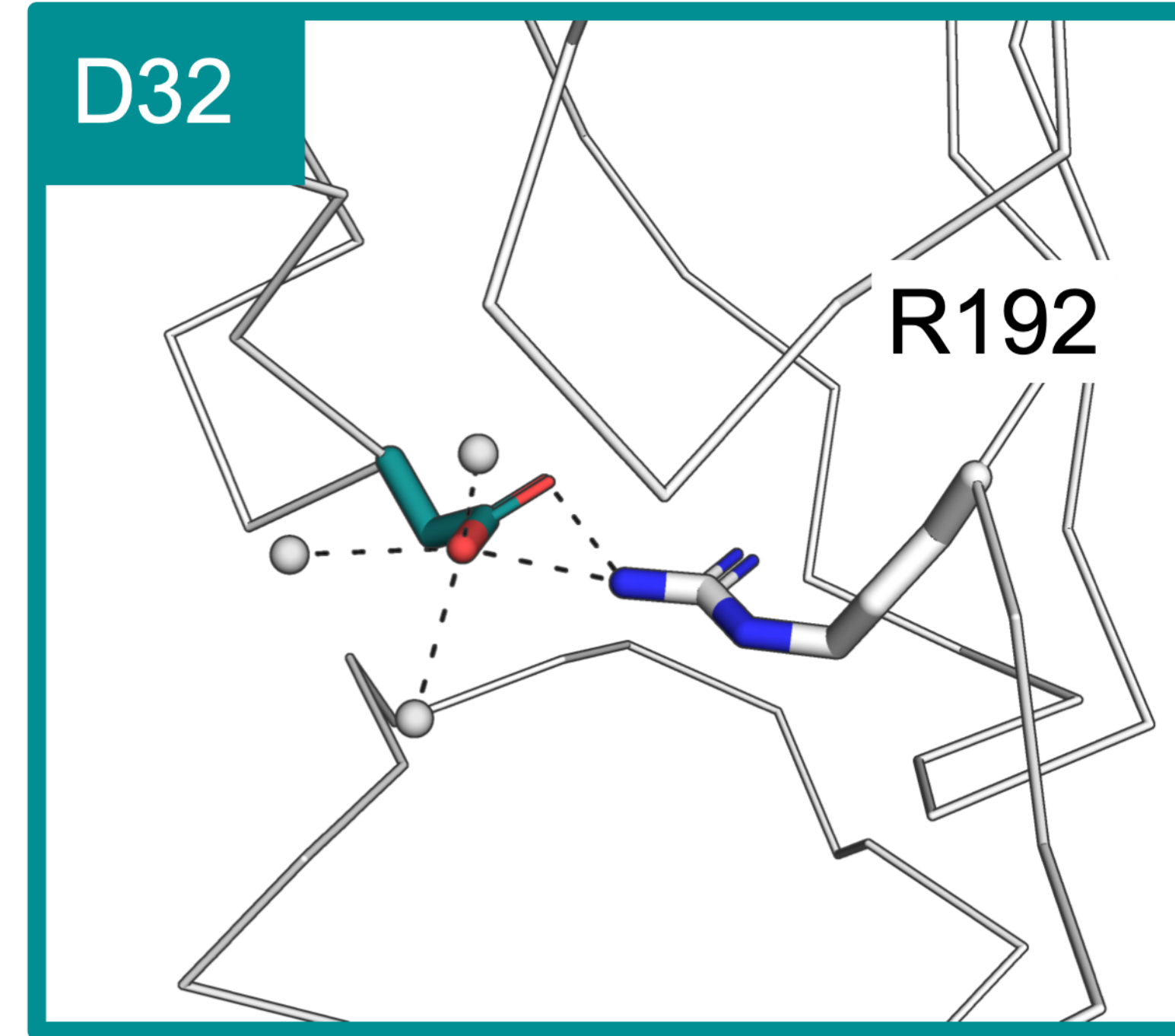
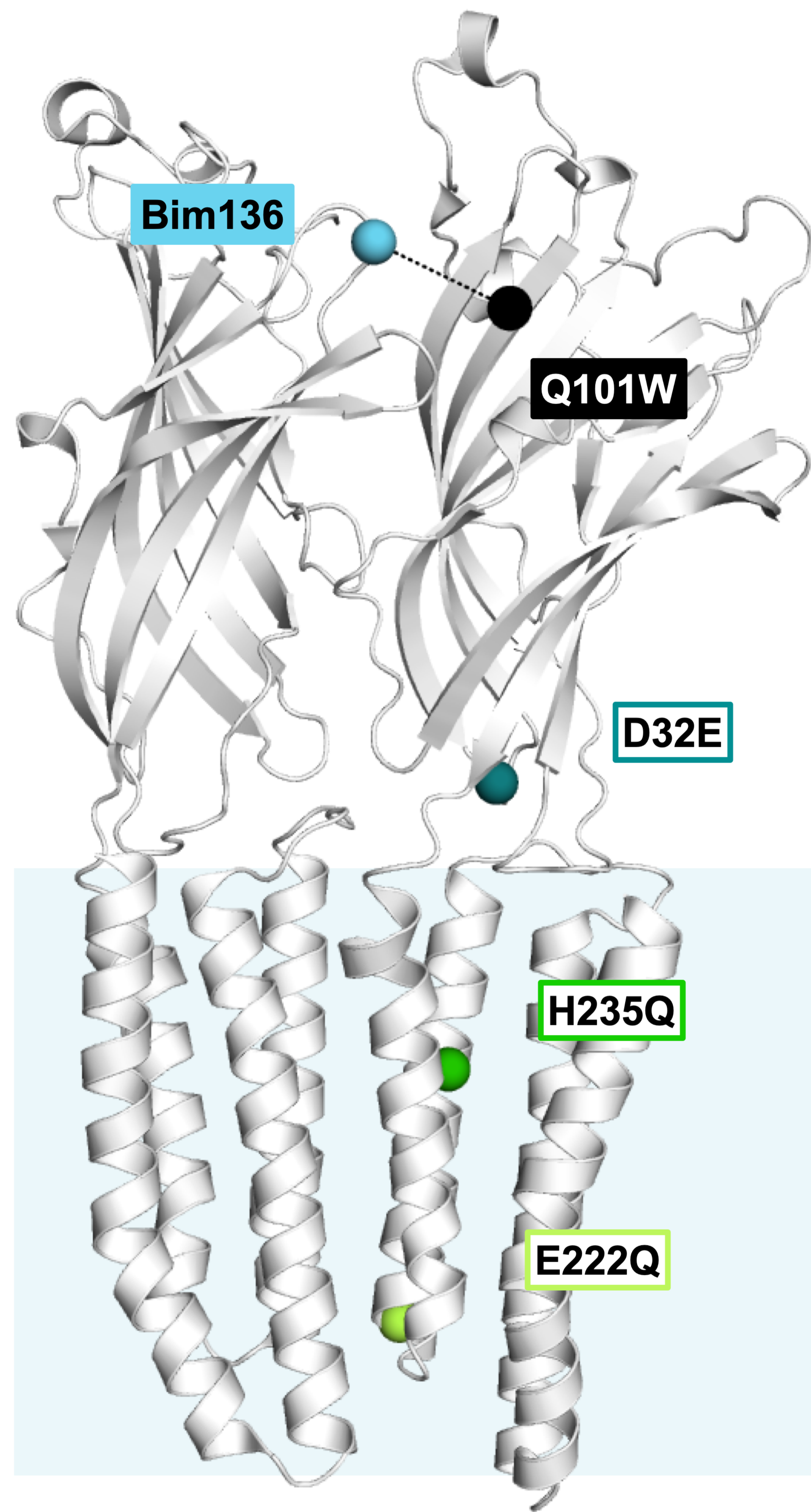
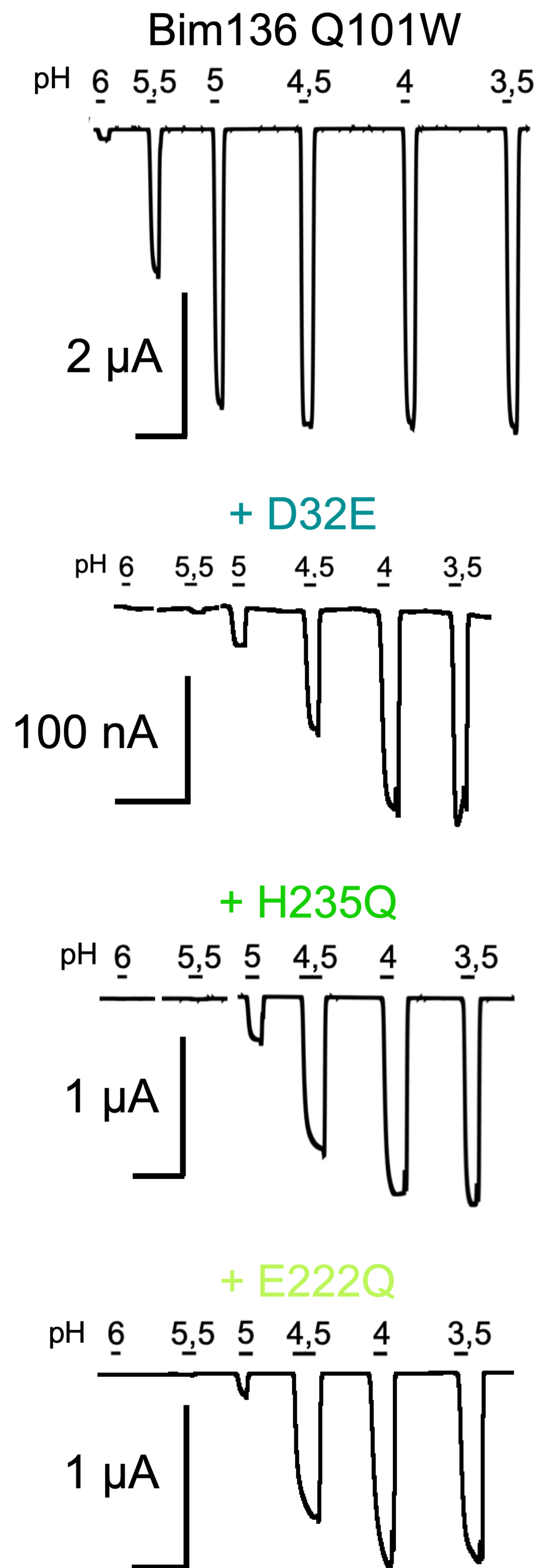


Figure 2

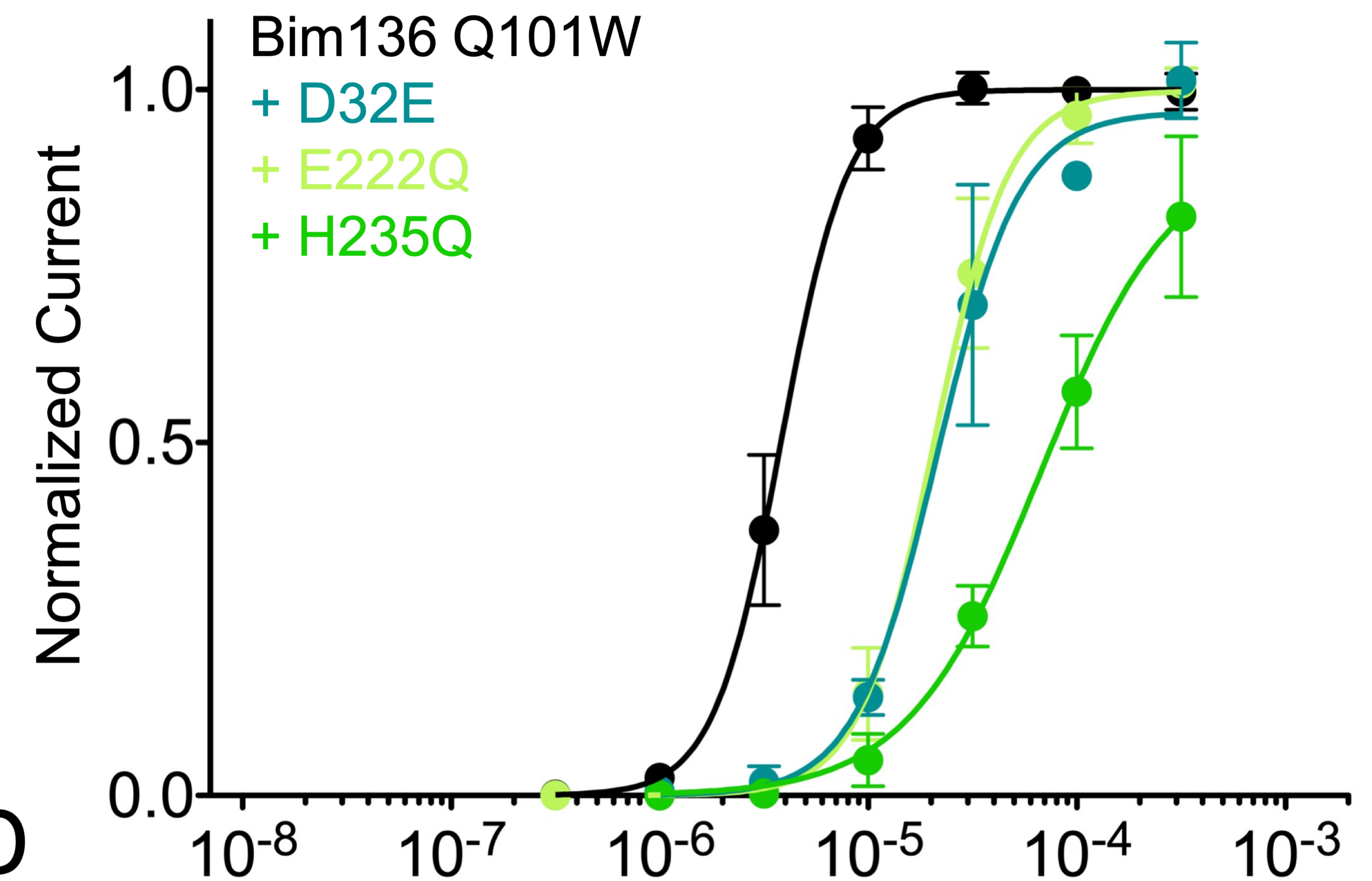
A



B



C



D

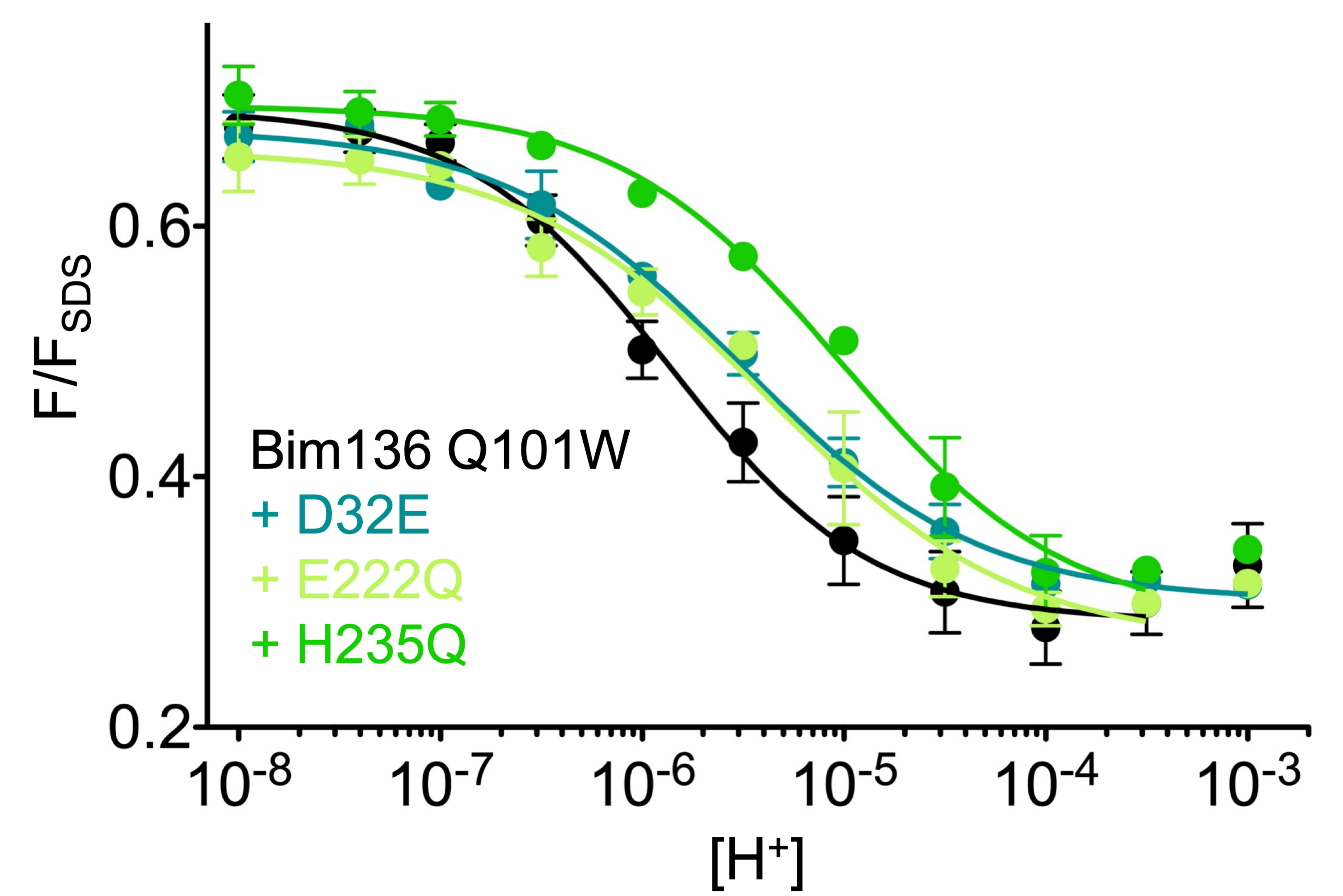
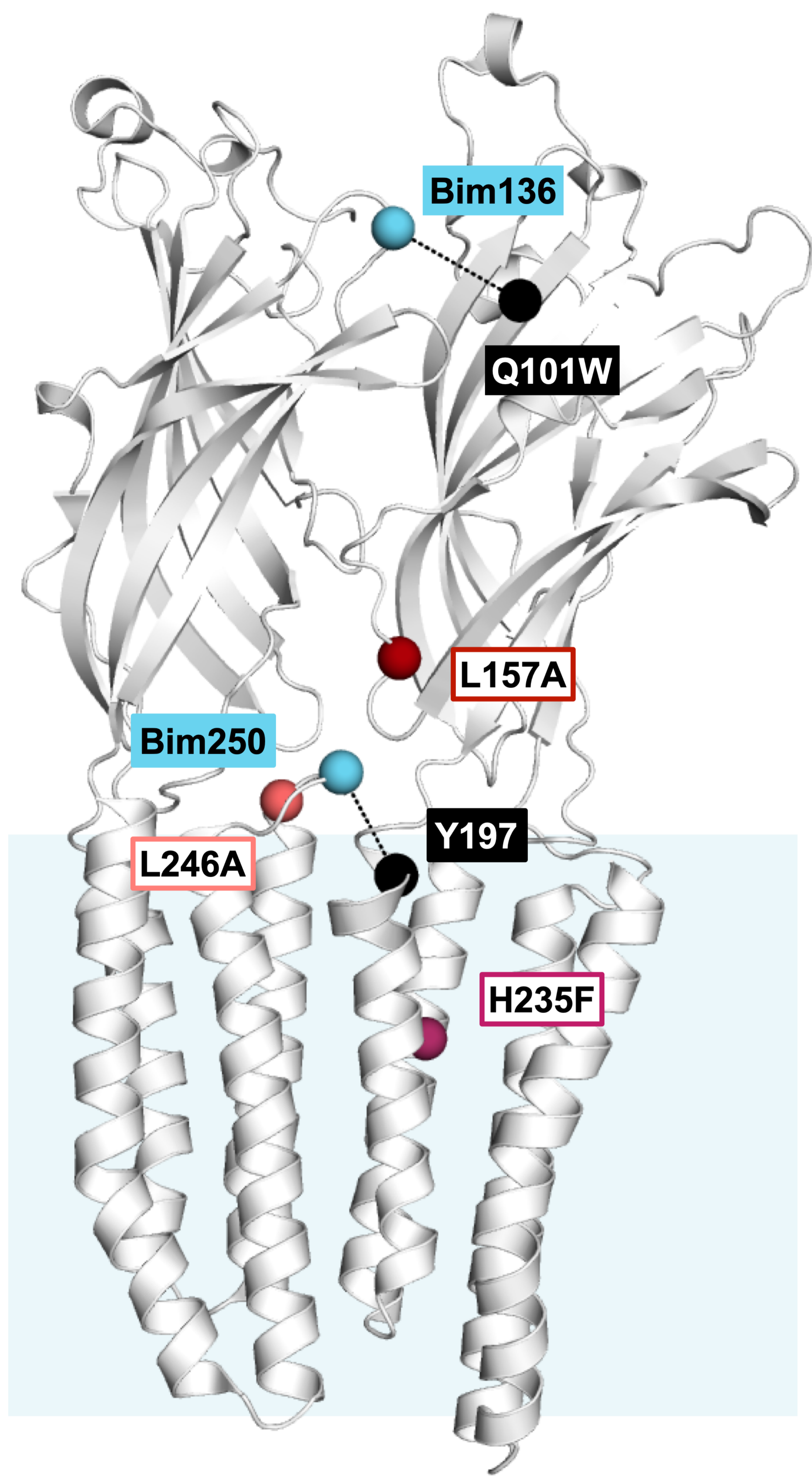
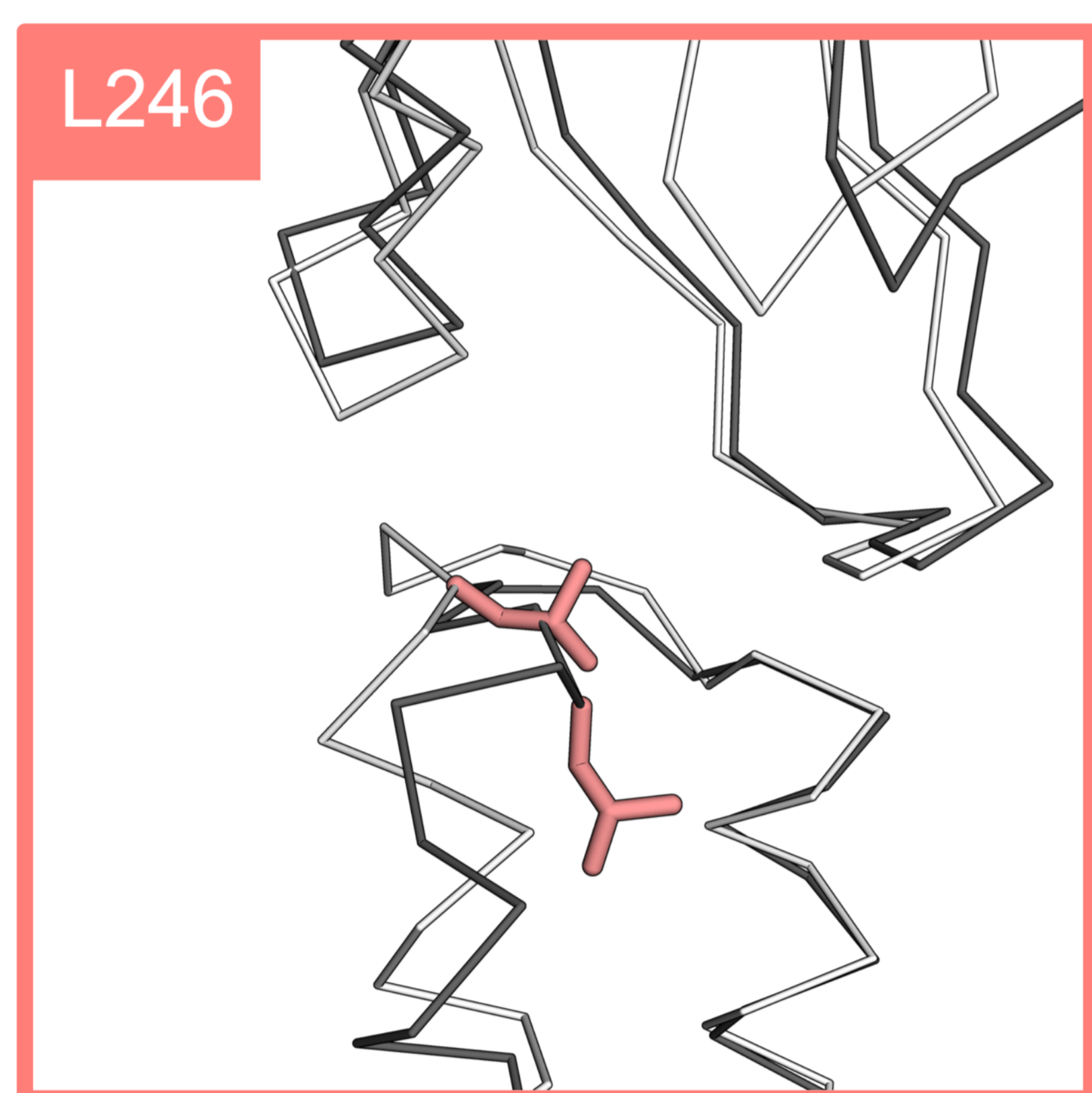
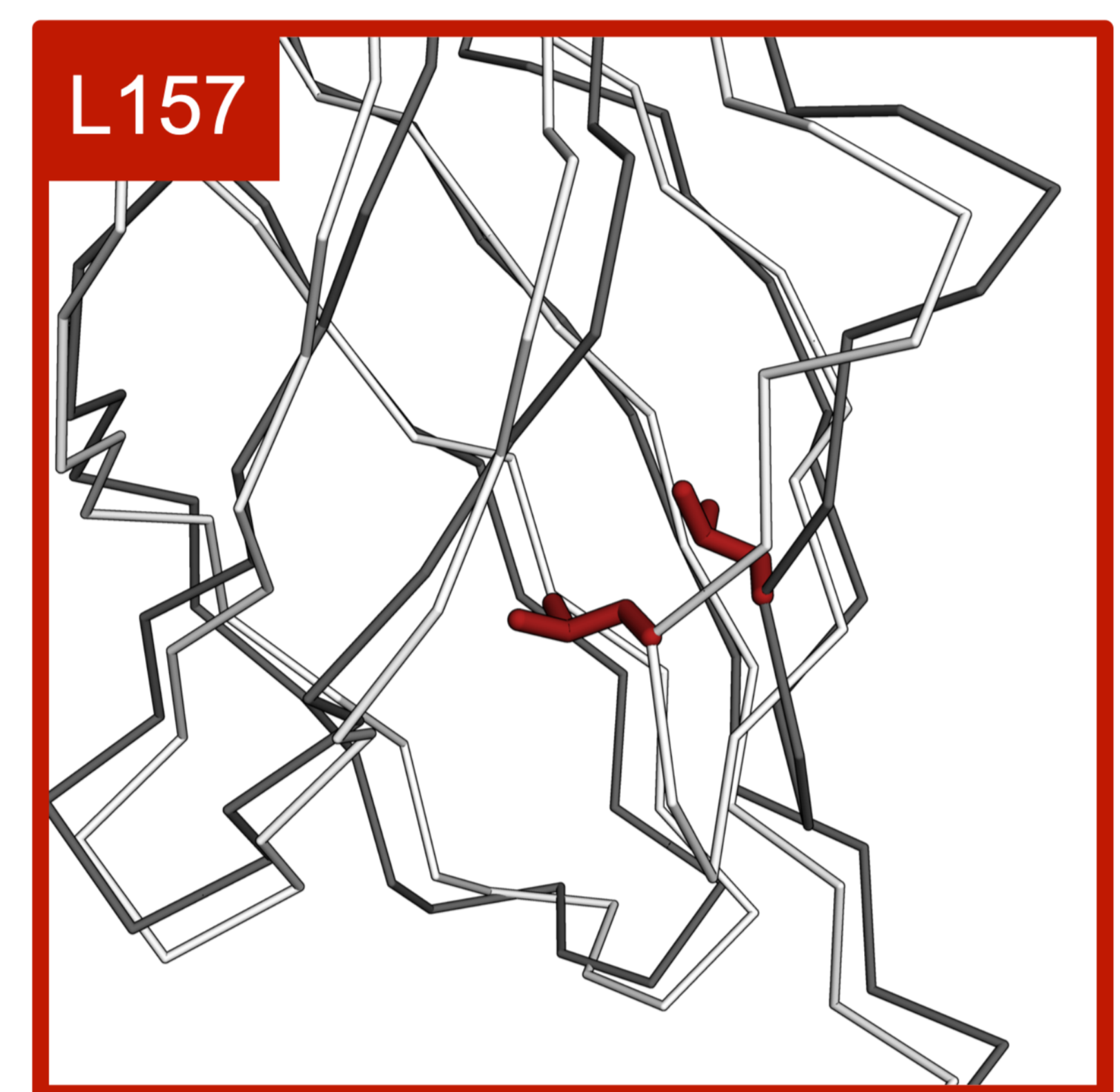
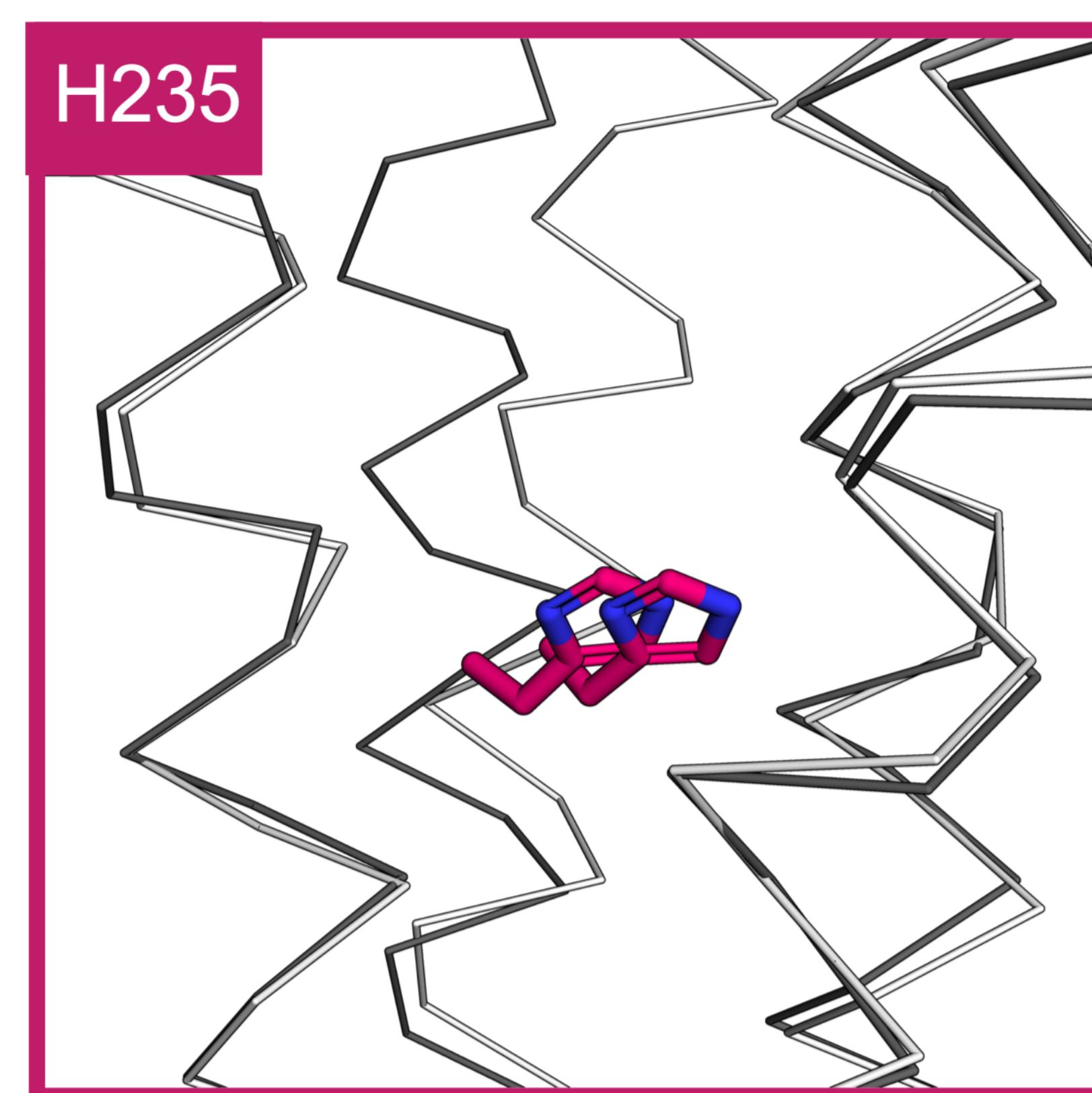


Figure 3

A

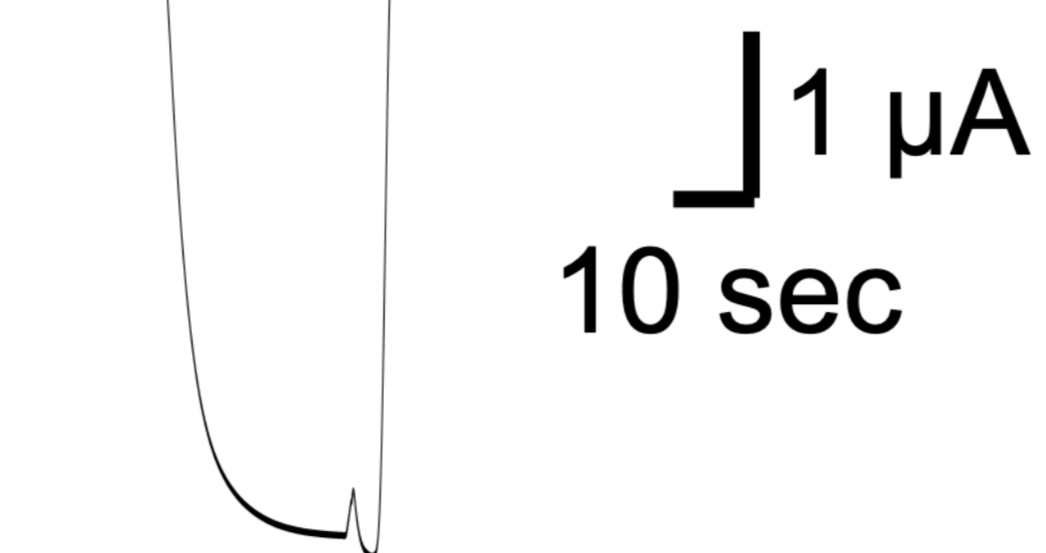


B

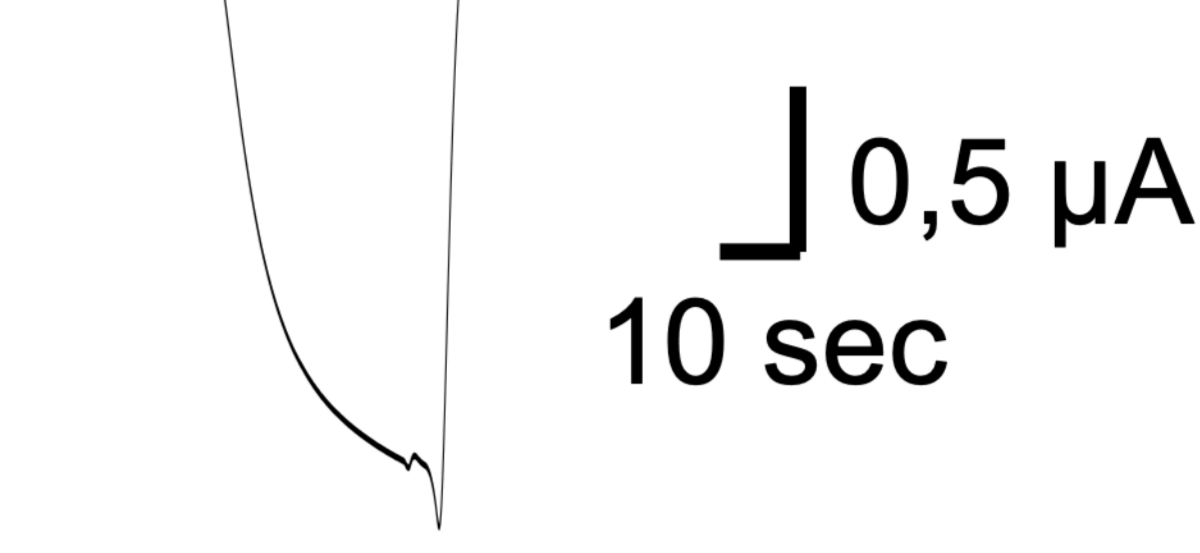


C

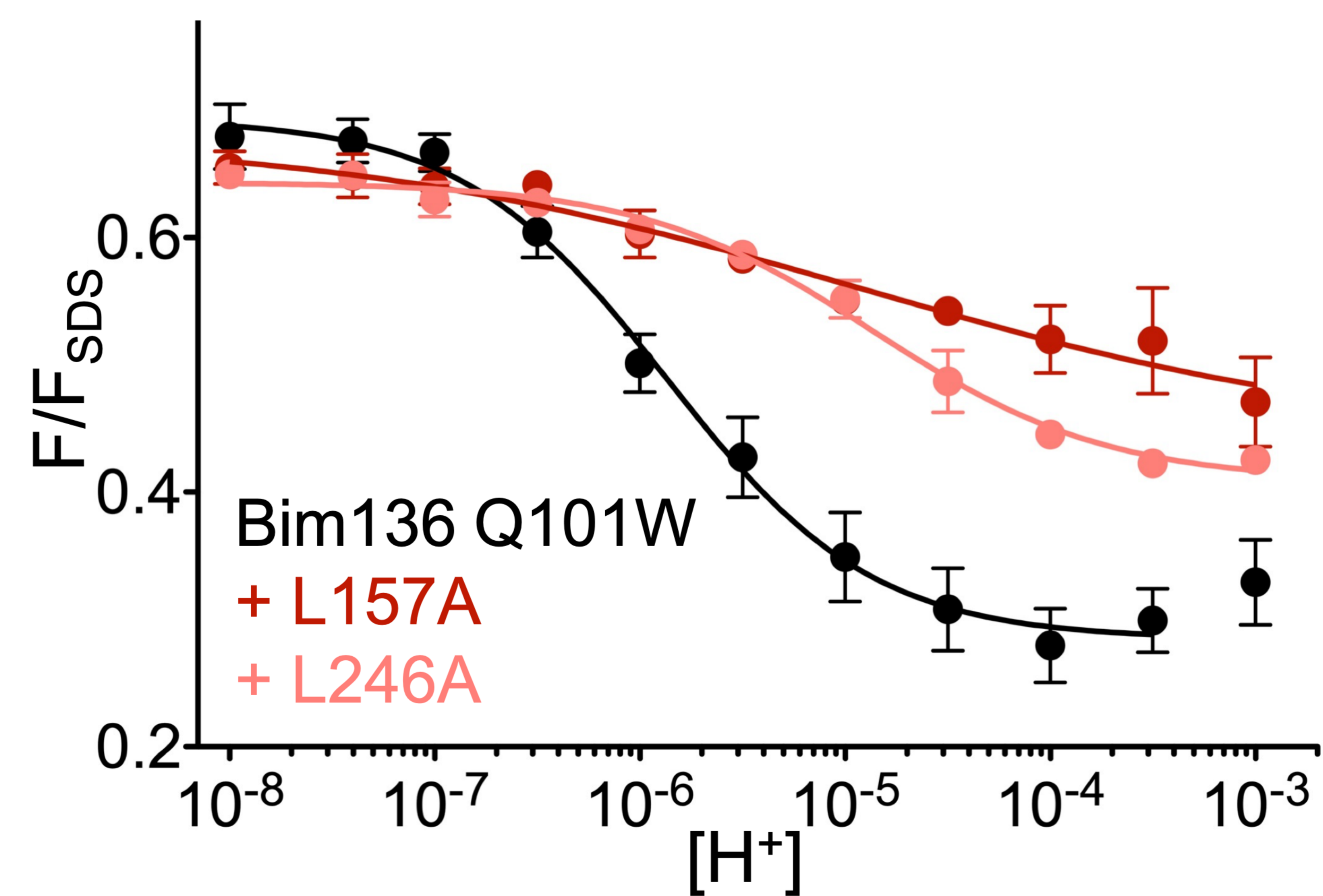
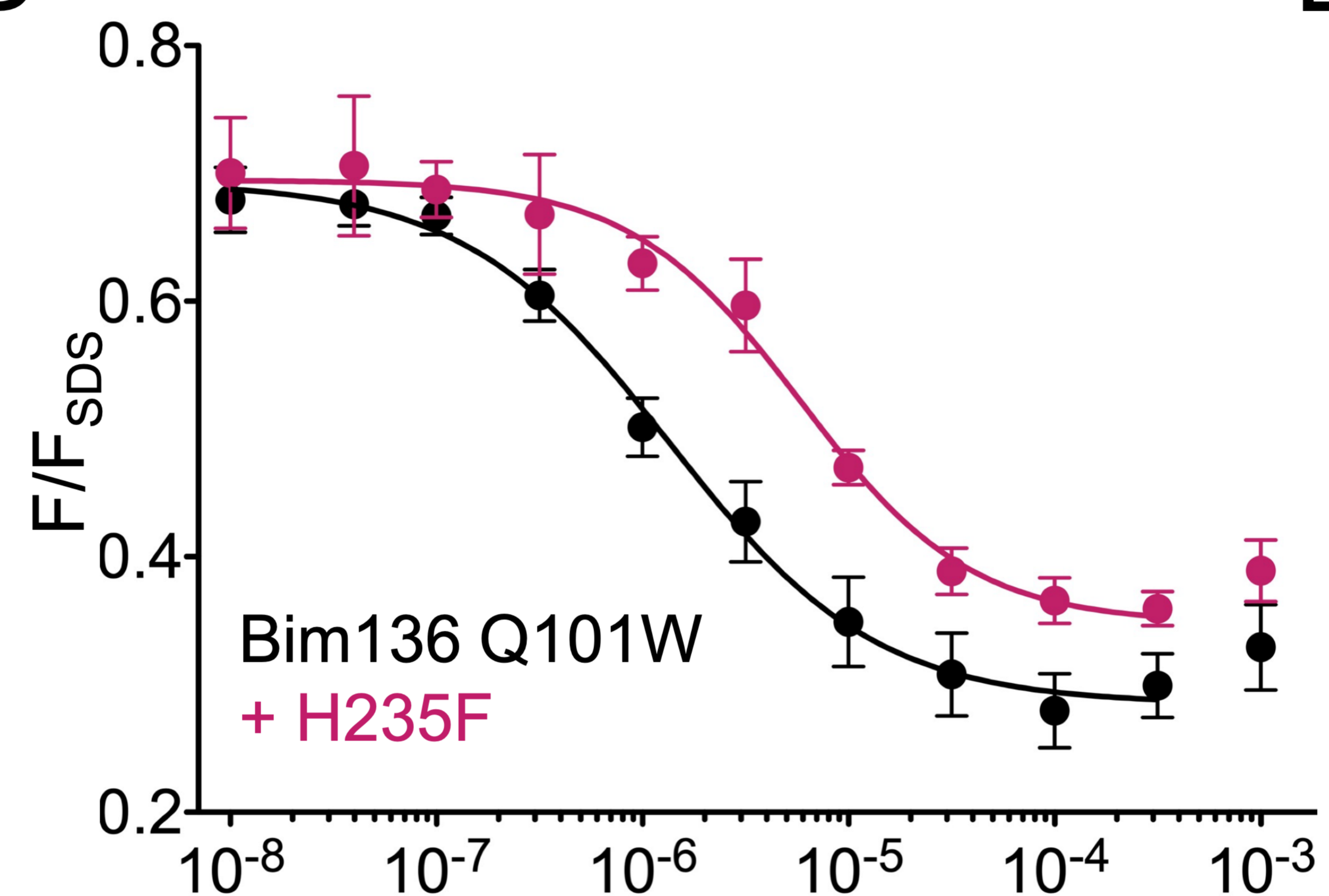
136Bim Q101W + H235F + L157A + L246A pH 3,5



250Bim Y197 + H235F + L157A + L246A pH 3,5



D



E

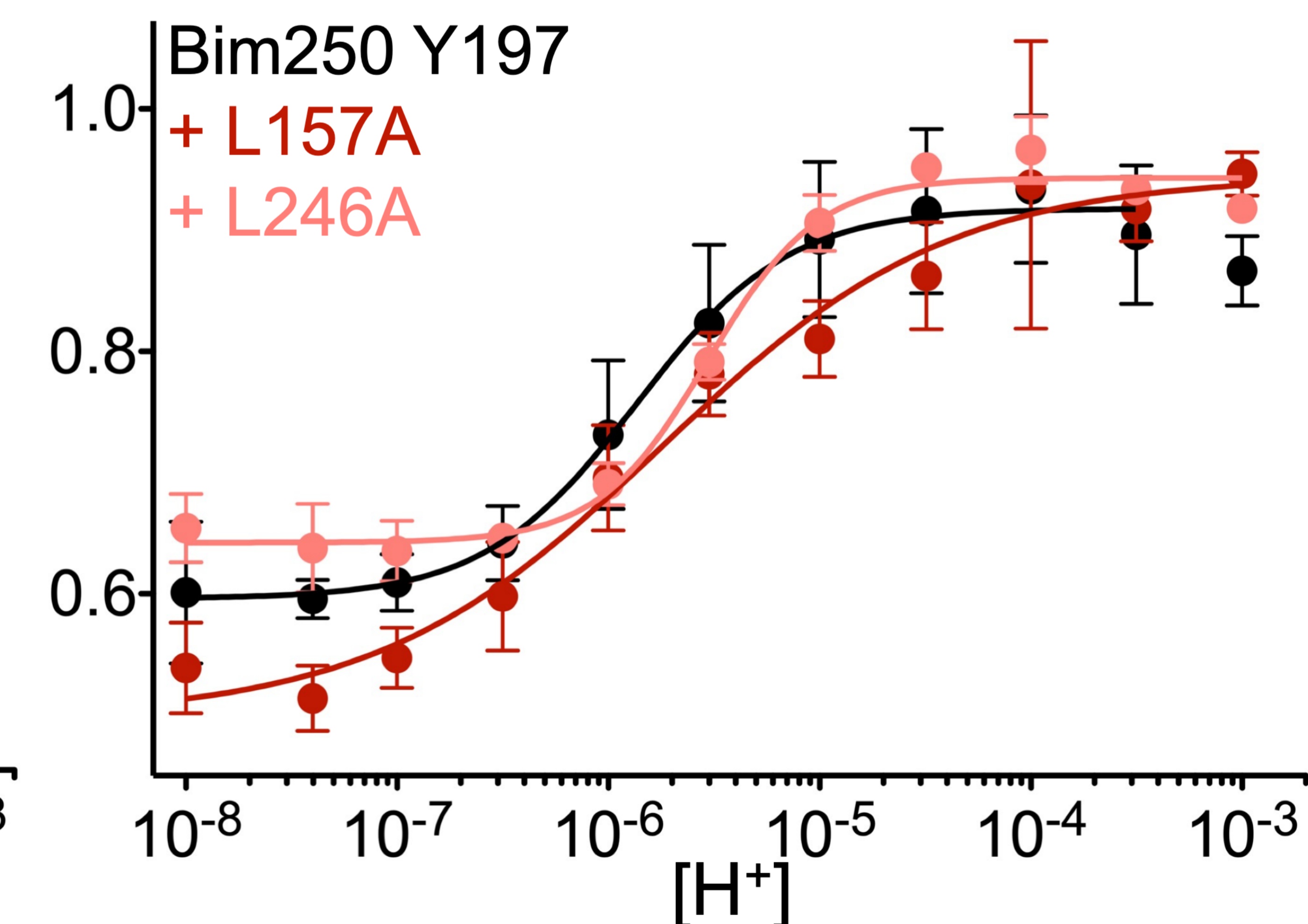
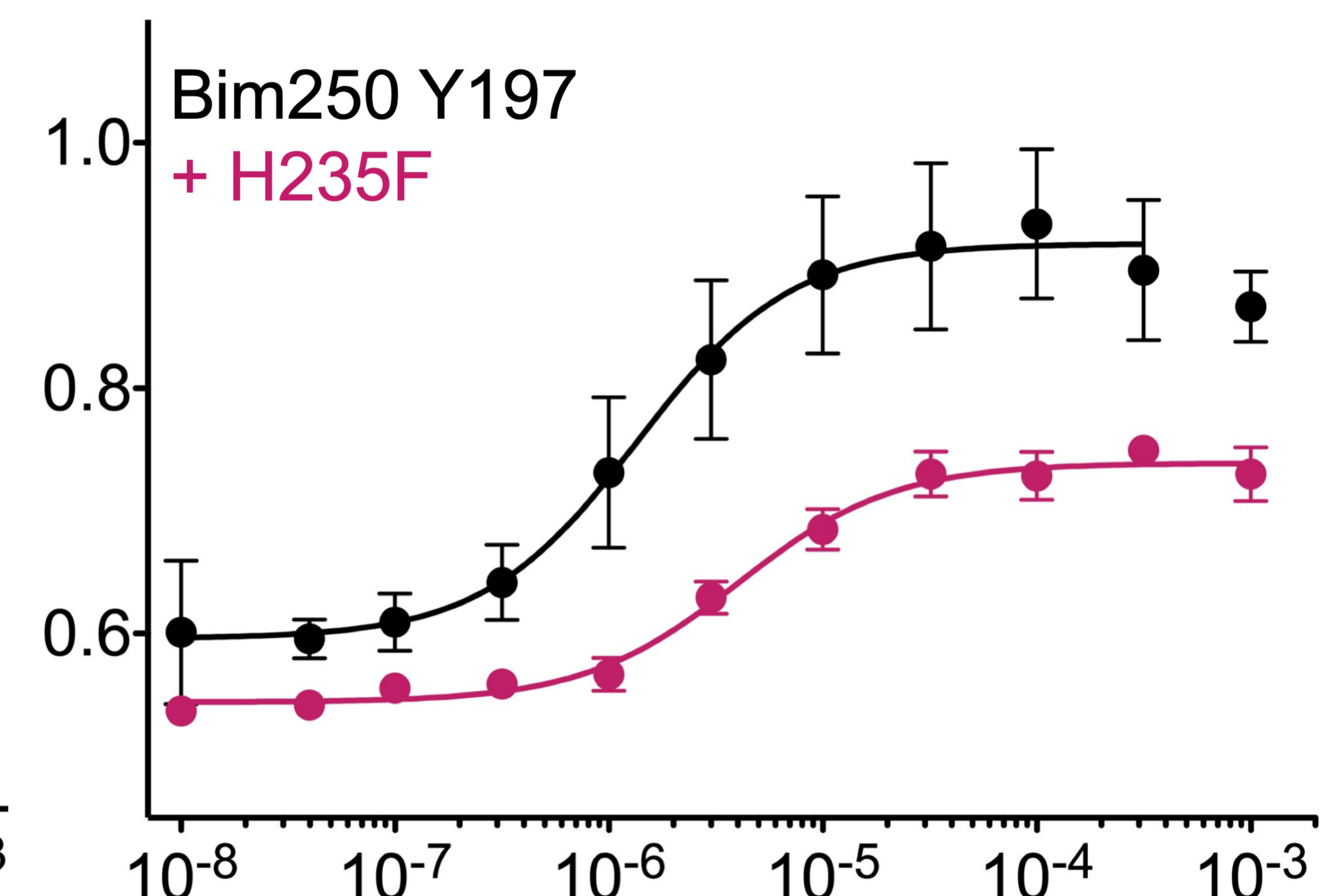
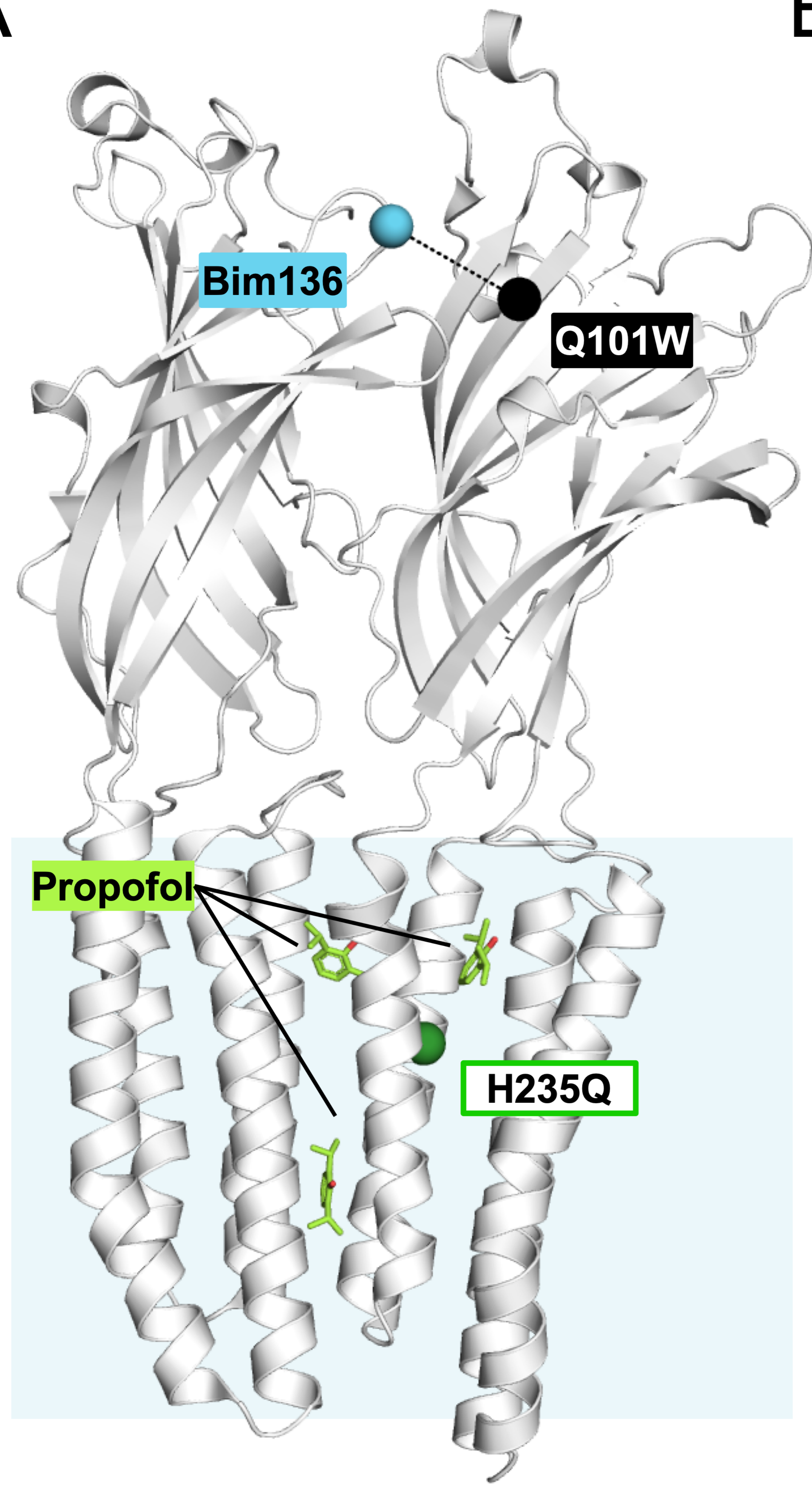
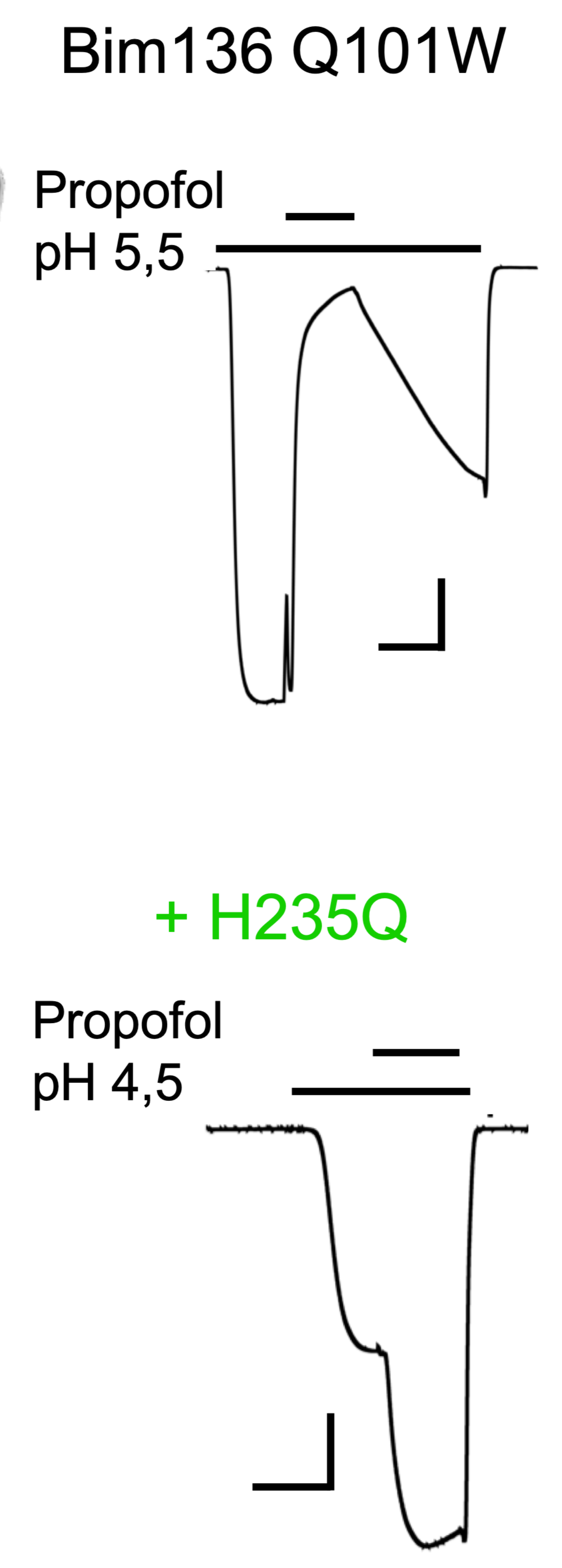
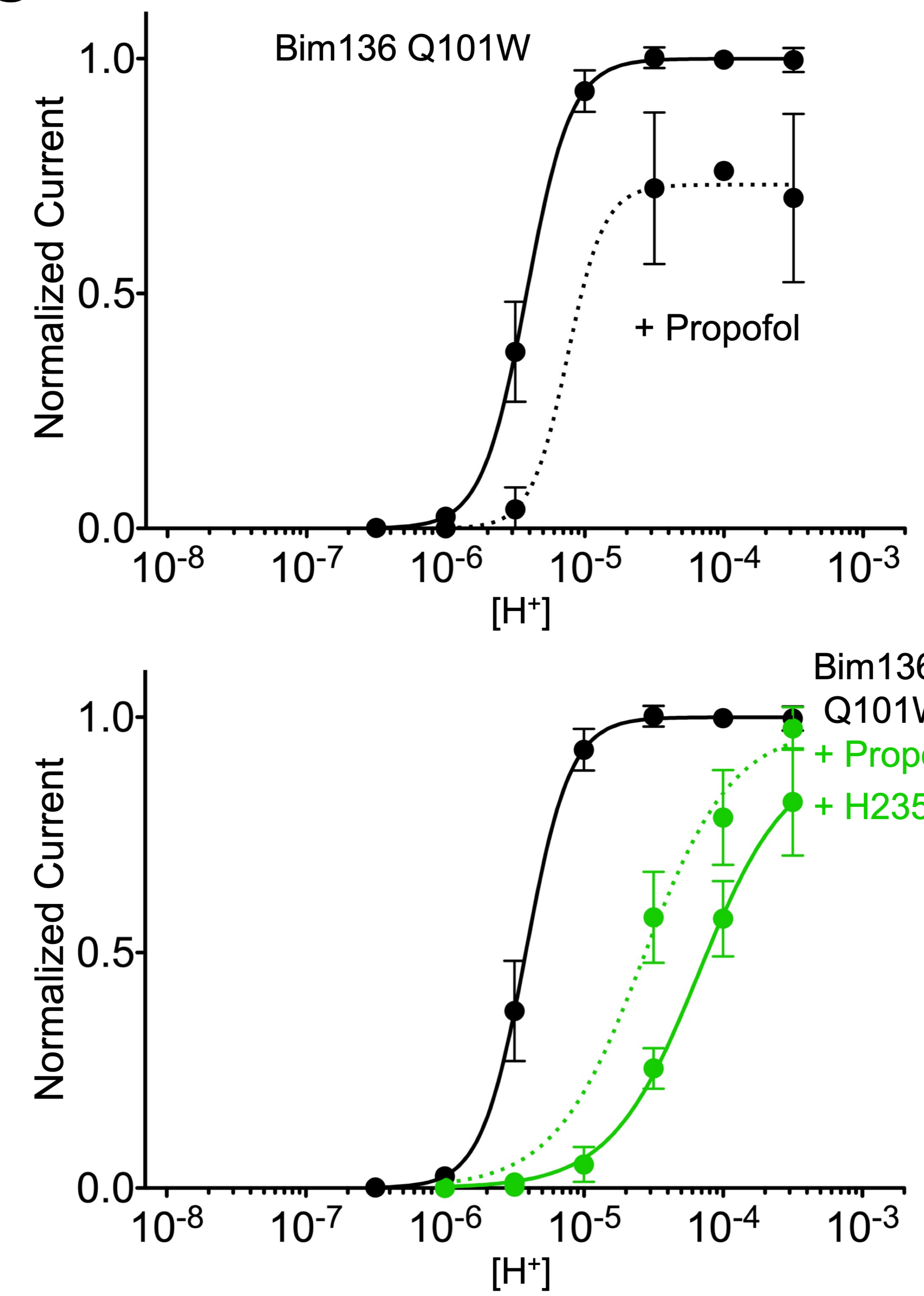
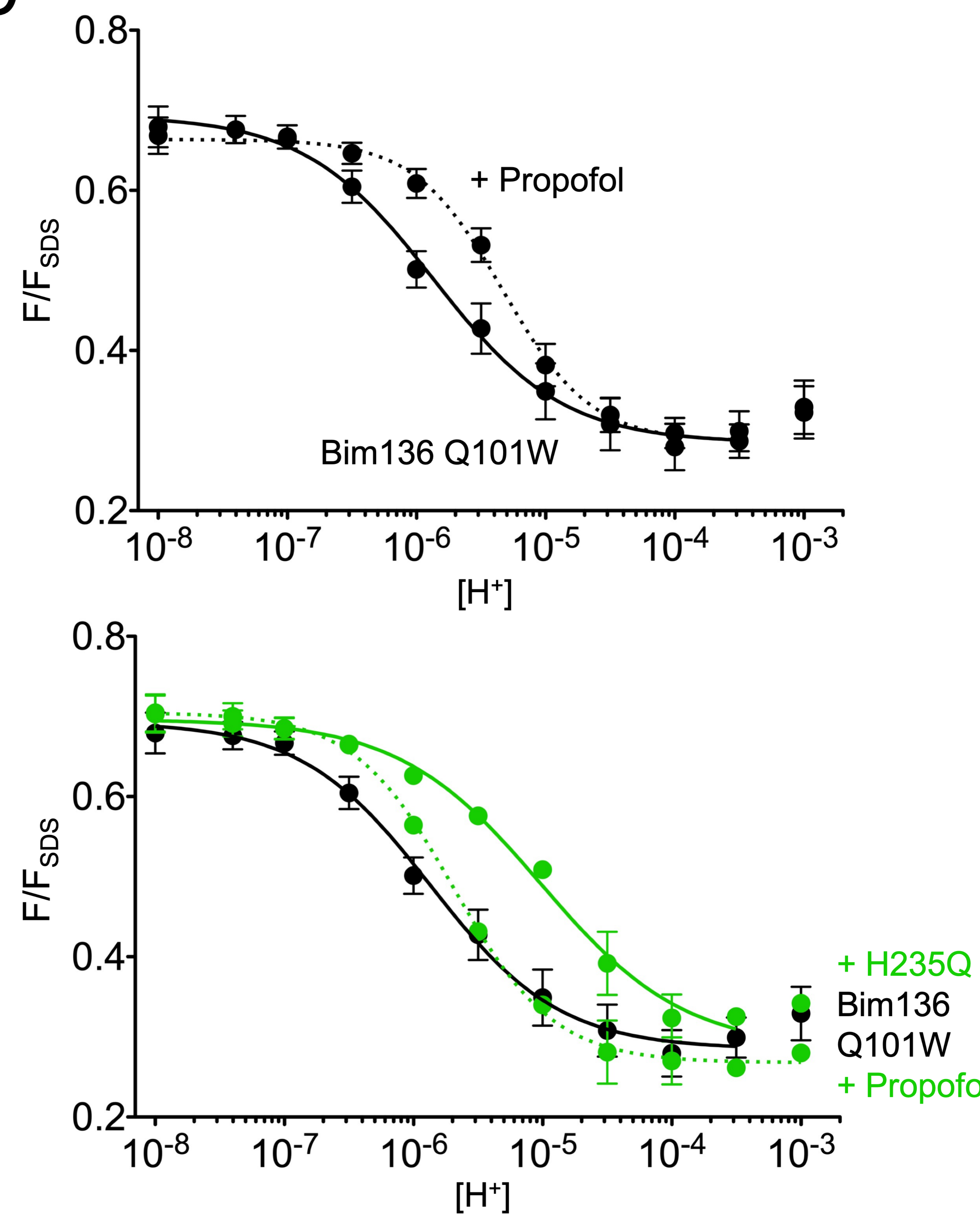


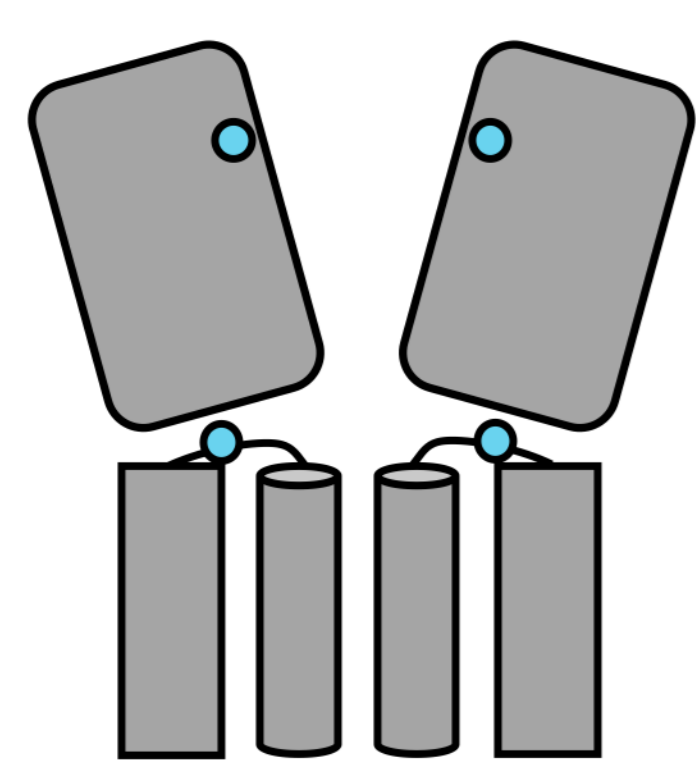
Figure 4

A**B****C****D****Figure 5**

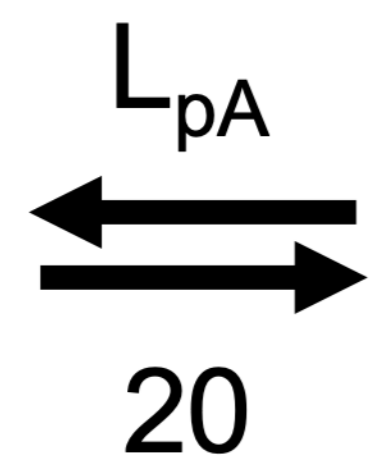
A

$$K_R = 3.6 \times 10^{-6}$$

$$K'_R = 5.0 \times 10^{-5}$$

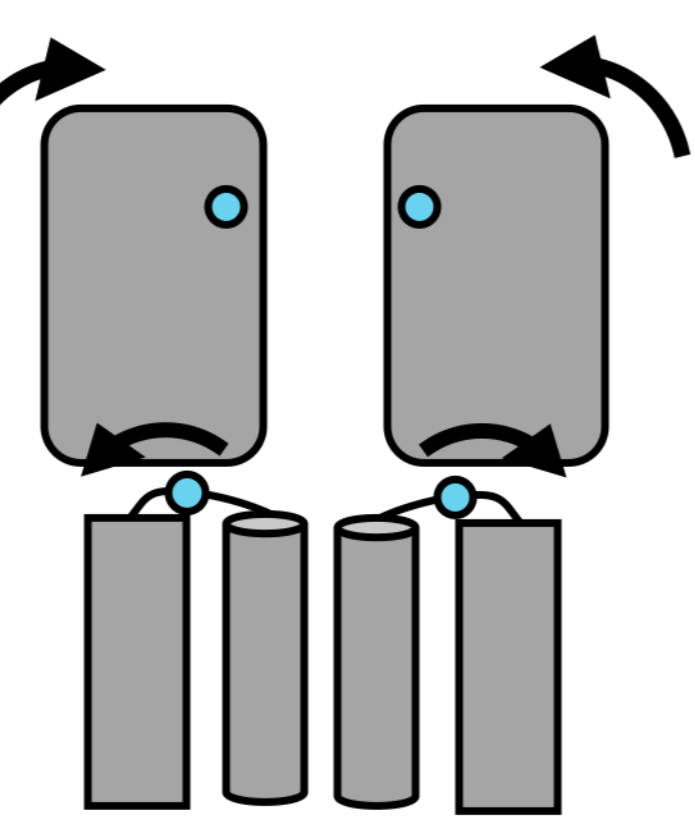


R

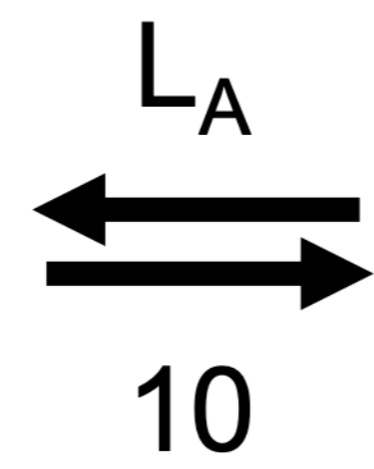


$$K_{pA} = 1.0 \times 10^{-6}$$

$$K'_{pA} = 5.0 \times 10^{-5}$$

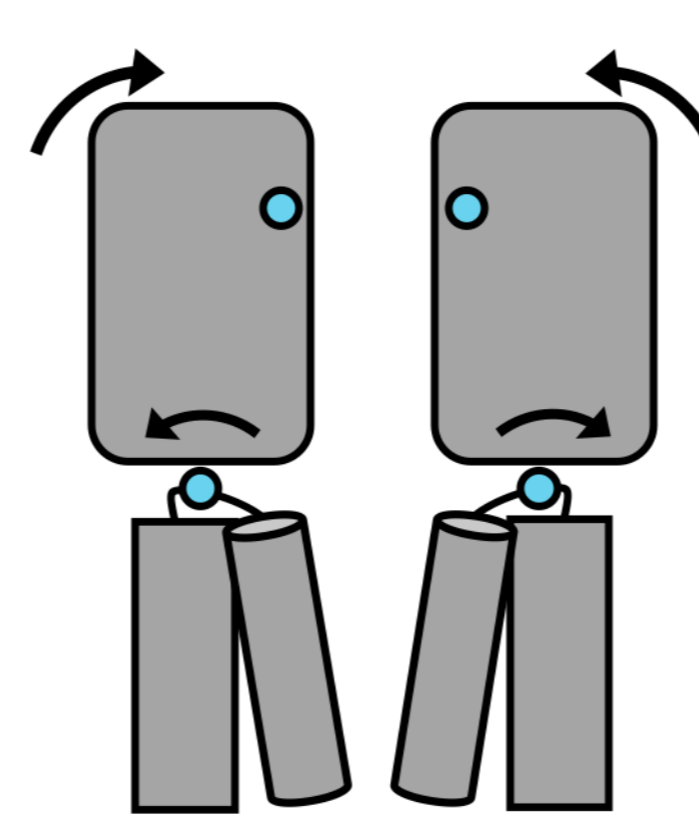


pA



$$K_A = 1.0 \times 10^{-6}$$

$$K'_A = 5.0 \times 10^{-6}$$



A

$$F_{R, \text{Bim136 Q101W}} = 0.70$$

$$F_{R, \text{Bim250 Y197}} = 0.56$$

$$F_{pA, \text{Bim136 Q101W}} = 0.30$$

$$F_{pA, \text{Bim250 Y197}} = 0.92$$

$$F_{A, \text{Bim136 Q101W}} = 0.30$$

$$F_{A, \text{Bim250 Y197}} = 0.92$$

B

$$L_{pA, \text{Bim136-Q101W}} = 20$$

$$L_{A, \text{Bim136-Q101W}} = 10$$

$$L_{pA, \text{Bim136-Q101W-H235Q}} = 140$$

$$L_{A, \text{Bim136-Q101W-H235Q}} = 7000$$

	$L_{pA}/L_{pA, \text{Bim136-Q101W}}$	$L_A/L_{A, \text{Bim136-Q101W}}$
Bim136-Q101W	1	1
+ Y28F	75 000	1
+ E26Q	15	10
+ D32E	2	80
+ E222Q	1.5	40
+ H235Q	7	700
+ Propofol	3	10
	$L_{pA}/L_{pA, \text{Bim136-Q101W-H235Q}}$	$L_A/L_{A, \text{Bim136-Q101W-H235Q}}$
+ H235Q	0.18	0.21
+ propofol		

C

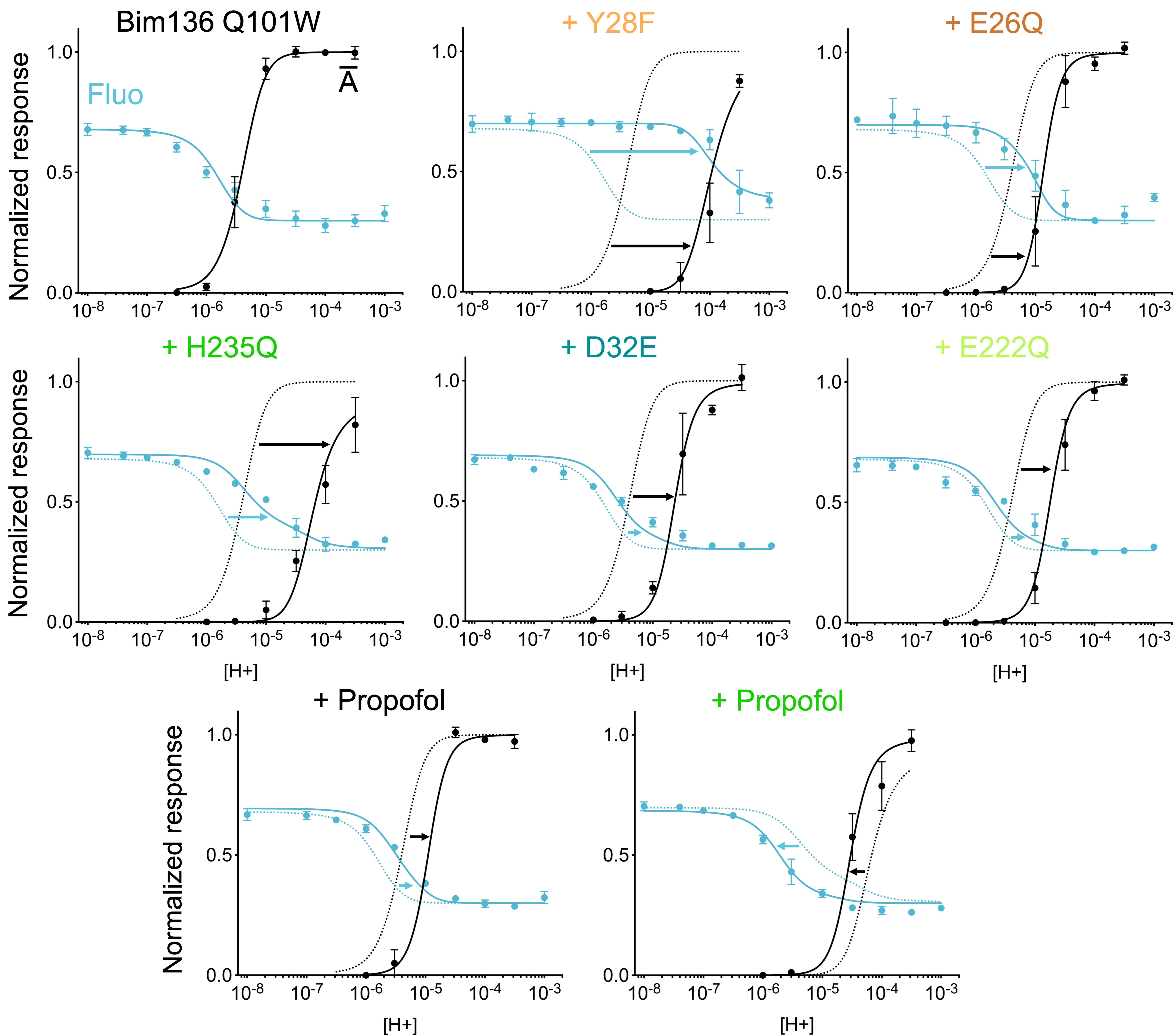
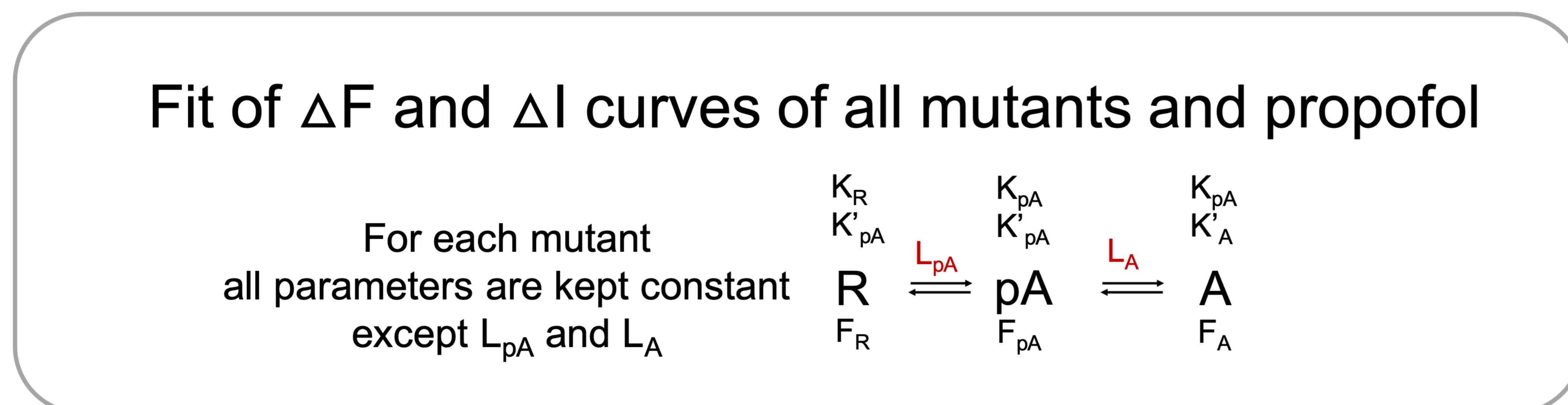
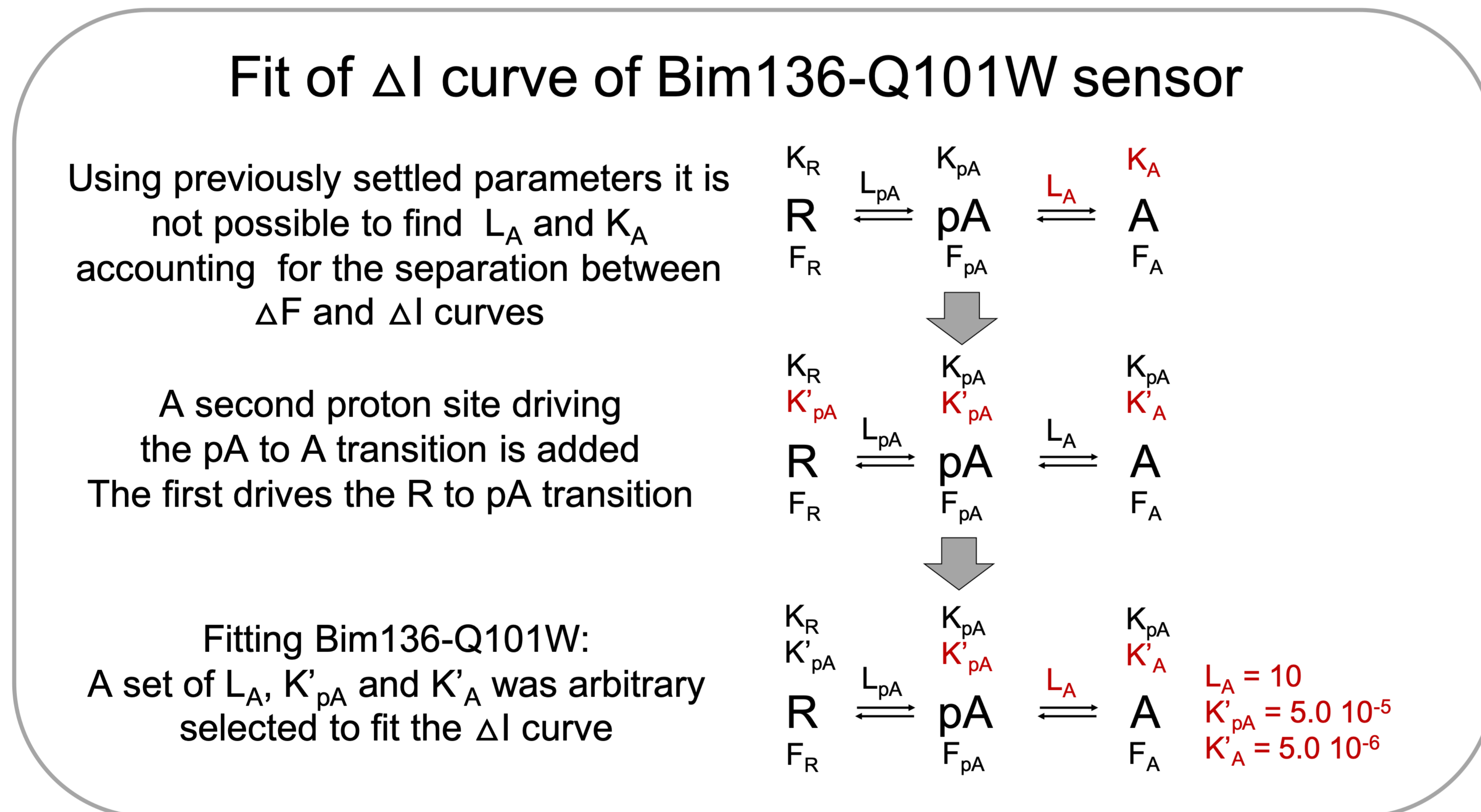
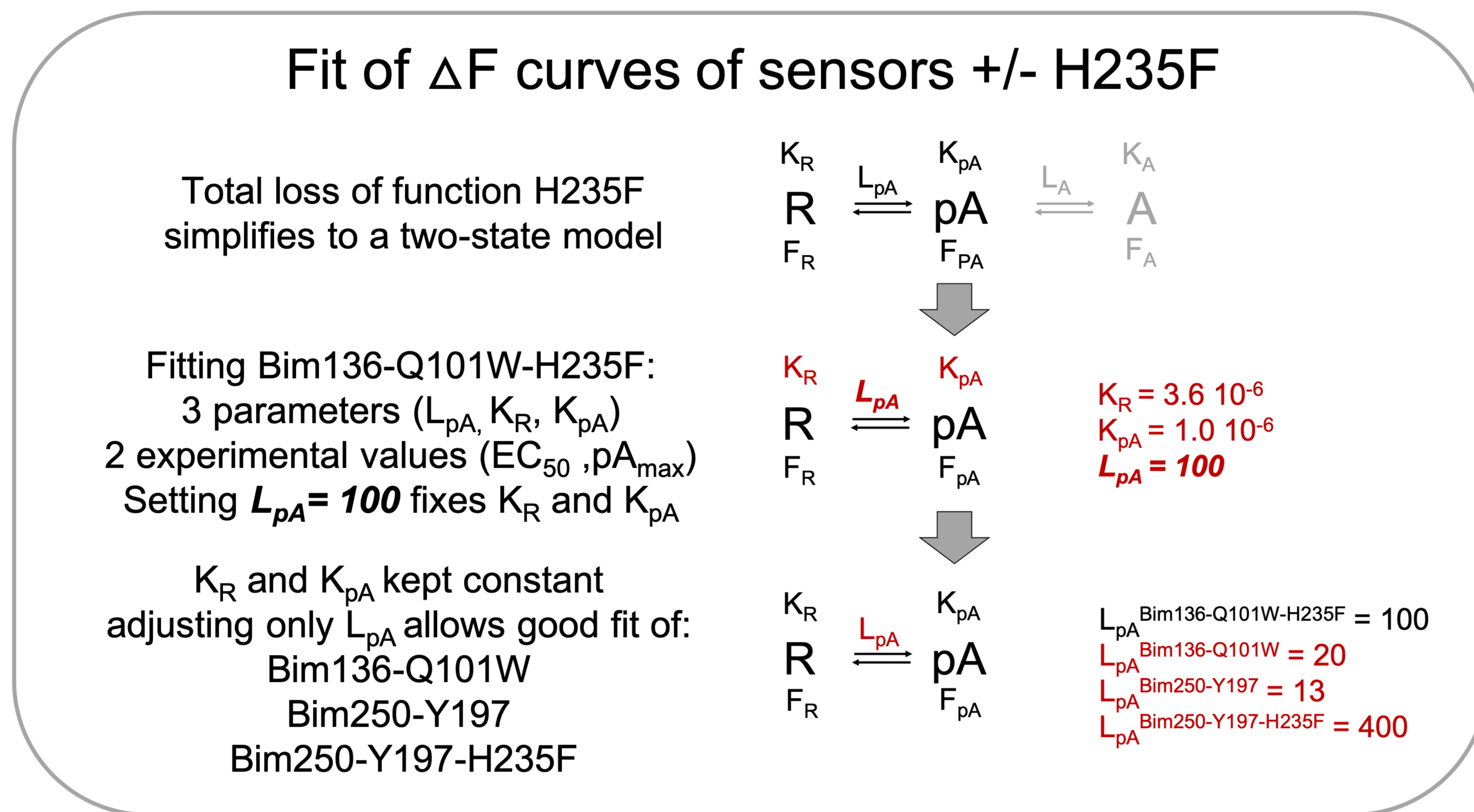
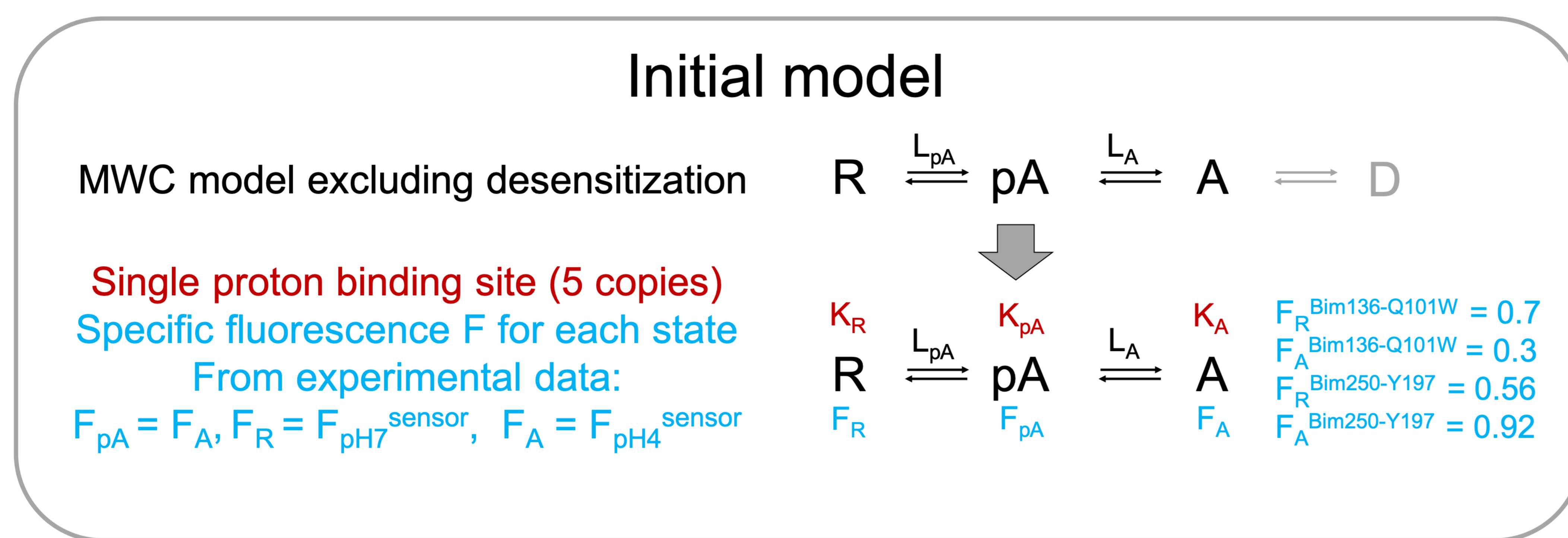


Figure 6



Verify robustness of the effects of mutants on L_A and L_{pA}

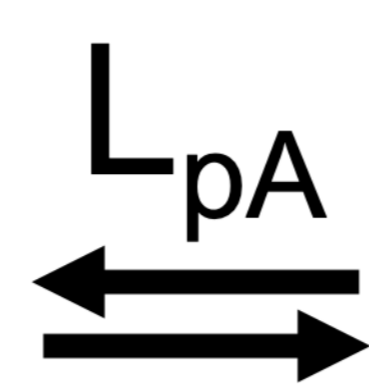
The whole procedure is repeated with, for Bim136-Q101W-H235F, $L_{pA} = 1\ 000$ and $L_{pA} = 100\ 000$

Figure 6 – Supplementary 1

A

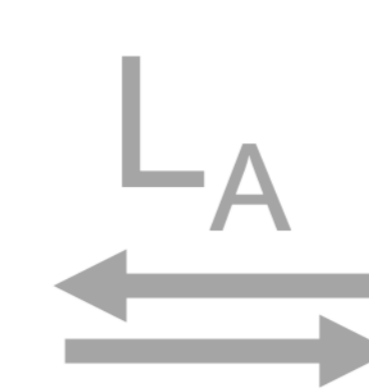
$$K_R = 3.6 \times 10^{-6}$$

R



$$K_{pA} = 1.0 \times 10^{-6}$$

pA



$$K_A = 1.0 \times 10^{-6}$$

A

$$F_R^{\text{Bim136 Q101W}} = 0.70$$

$$F_R^{\text{Bim250 Y197}} = 0.56$$

$$F_{pA}^{\text{Bim136 Q101W}} = 0.30$$

$$F_{pA}^{\text{Bim250 Y197}} = 0.92$$

$$F_A^{\text{Bim136 Q101W}} = 0.30$$

$$F_A^{\text{Bim250 Y197}} = 0.92$$

B

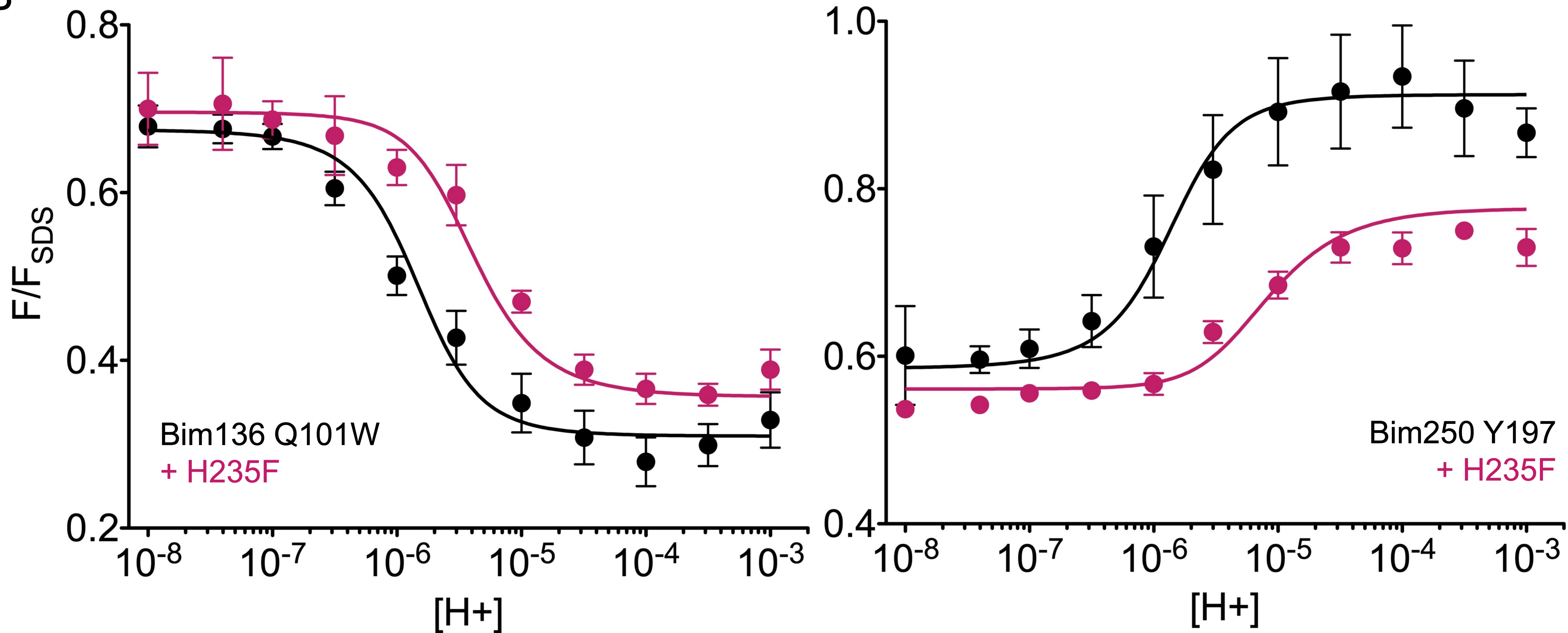


Figure 6 – Supplementary 2

A

$$L_{pA}^{\text{Bim136-Q101W}} = 20$$

$$L_{pA}^{\text{Bim250-Y197}} = 70$$

$$L_A^{\text{Bim136-Q101W}} = 10$$

$$L_A^{\text{Bim250-Y197}} = 300$$

$$L_{pA}/L_{pA}^{\text{Bim136-Q101W}}$$

Bim136-Q101W

+H235F

5

+L157A

50

+L246A

13.5

Bim250-Y197

0.65

$$L_{pA}/L_{pA}^{\text{Bim250-Y197}}$$

Bim250-Y197

+H235F

30.8

+L157A

3.85

+L246A

3.85

$$L_A/L_A^{\text{Bim250-Y197}}$$

 ∞ ∞ ∞

B

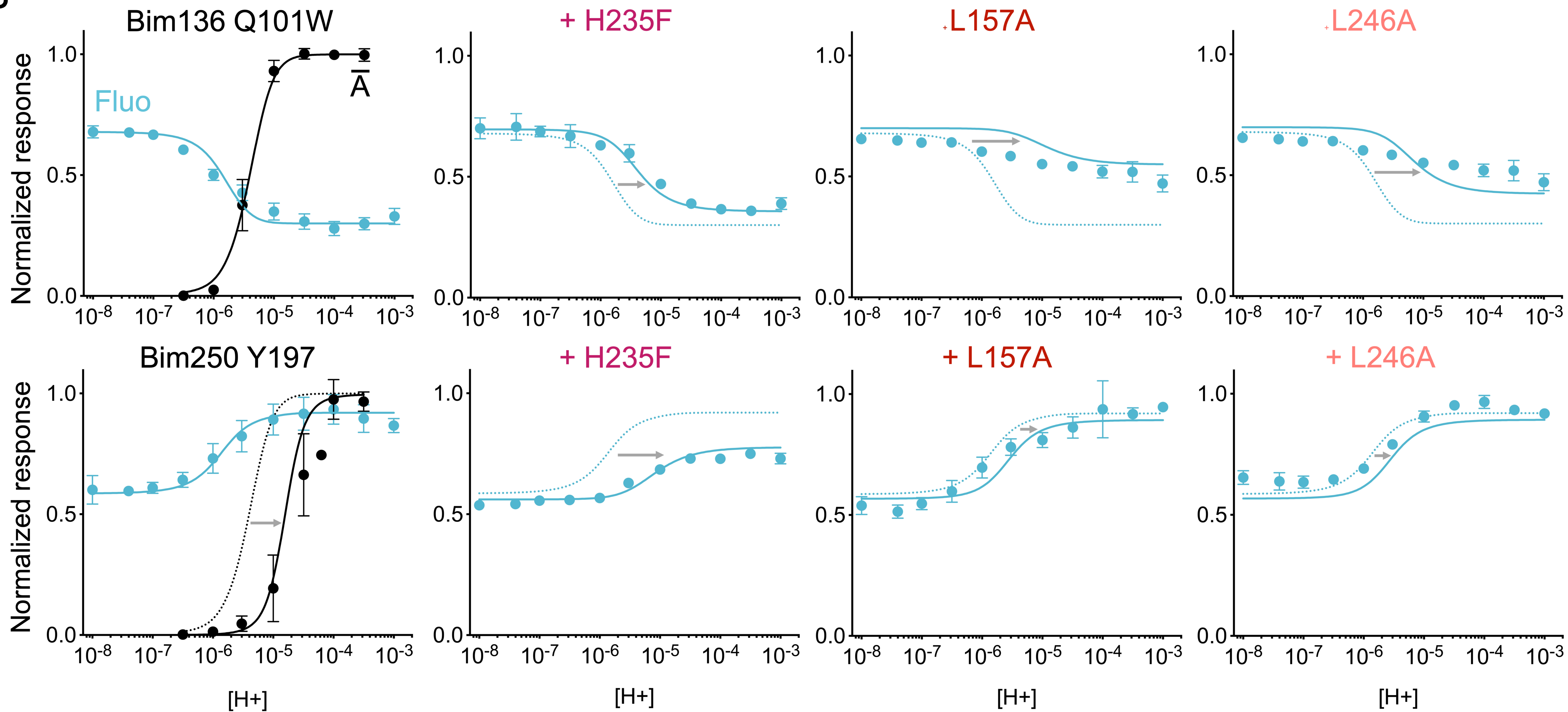
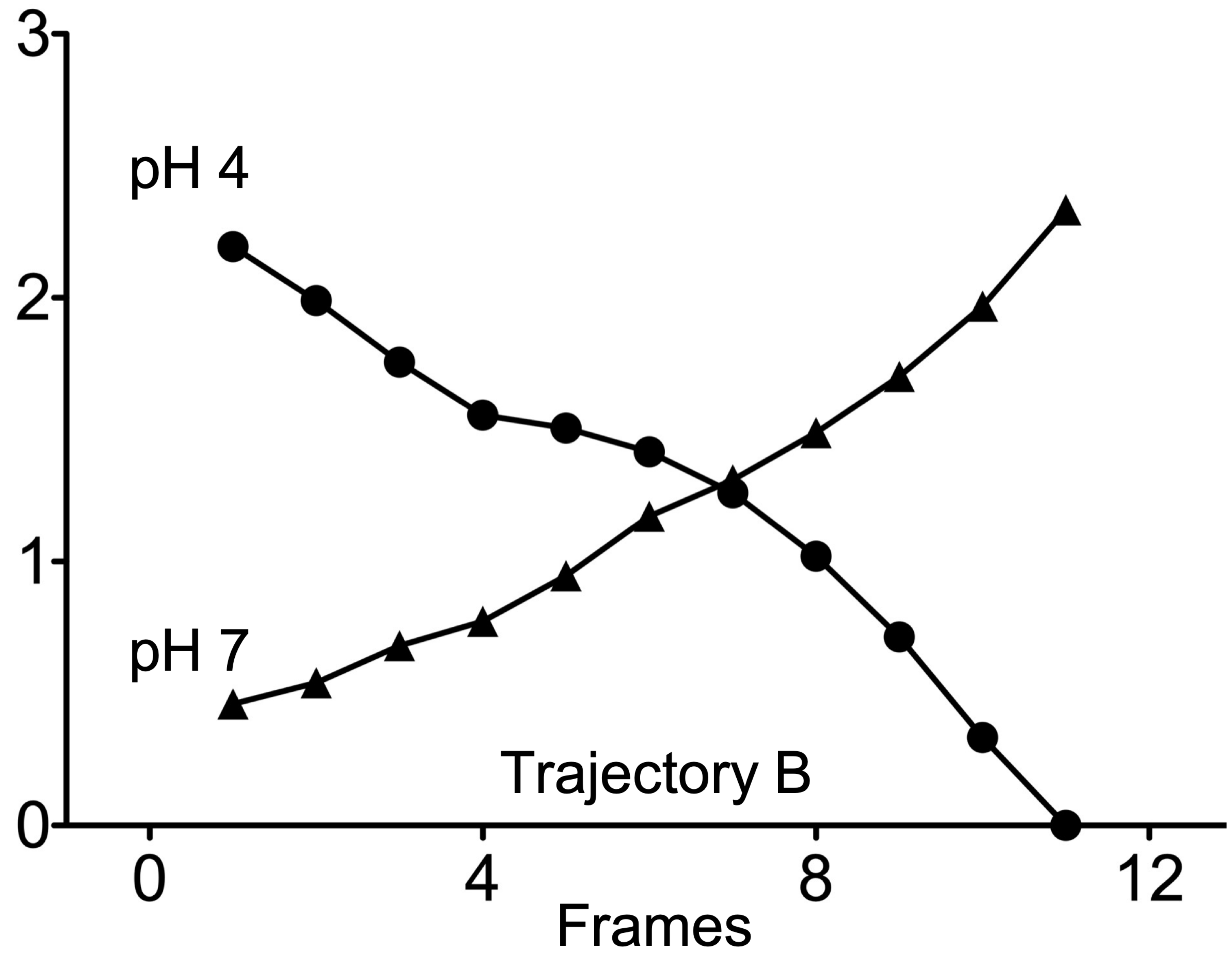
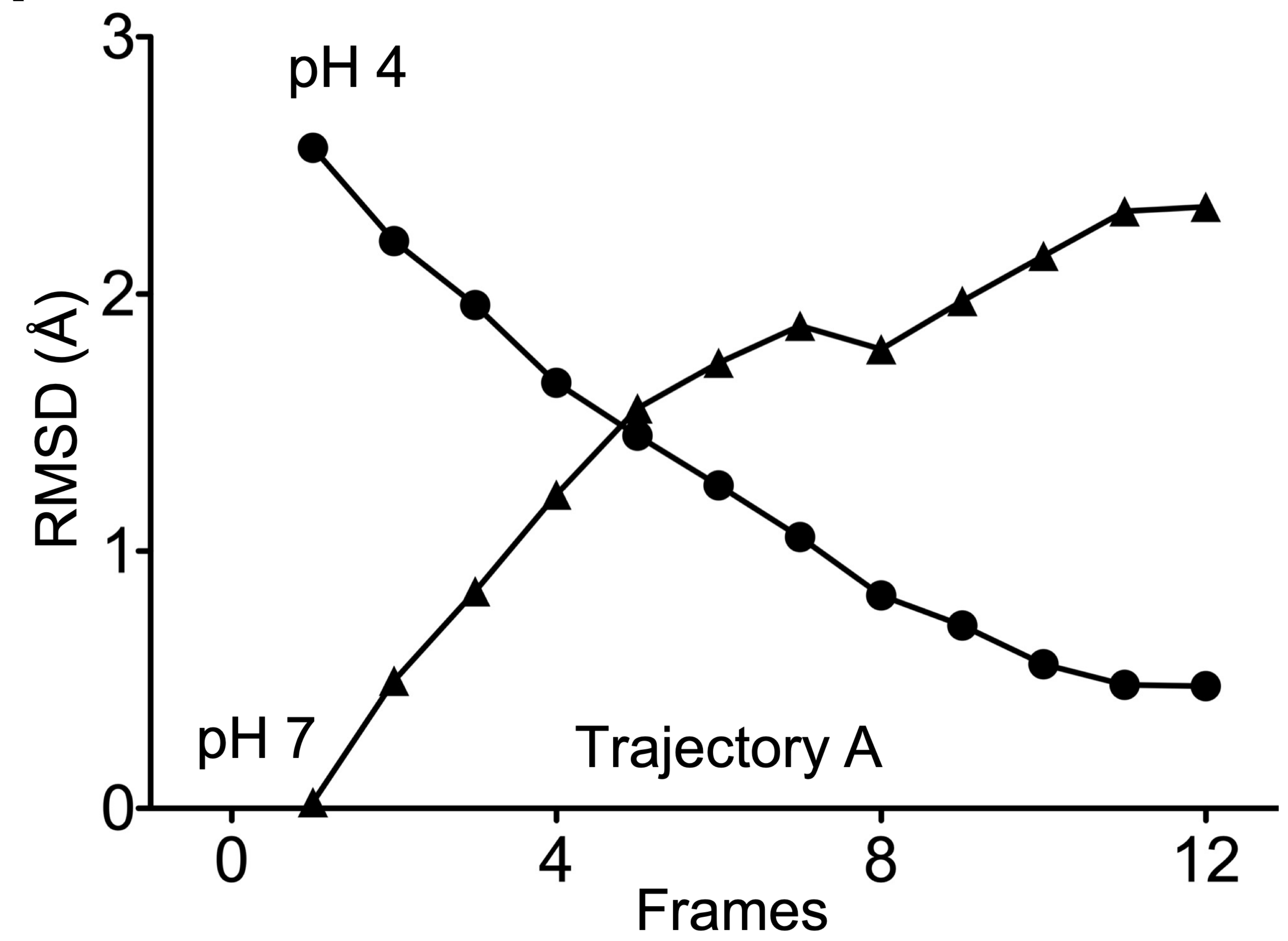
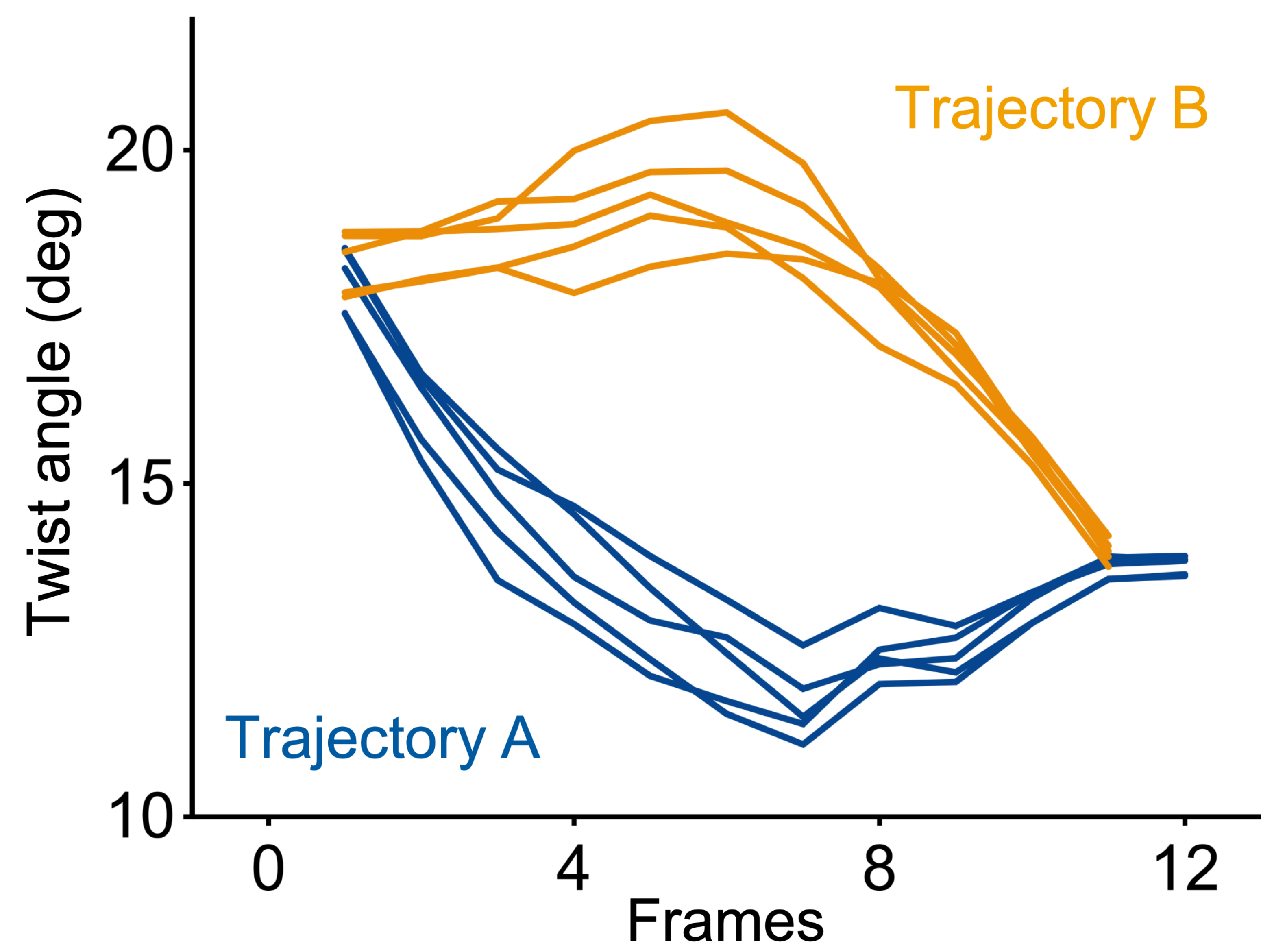
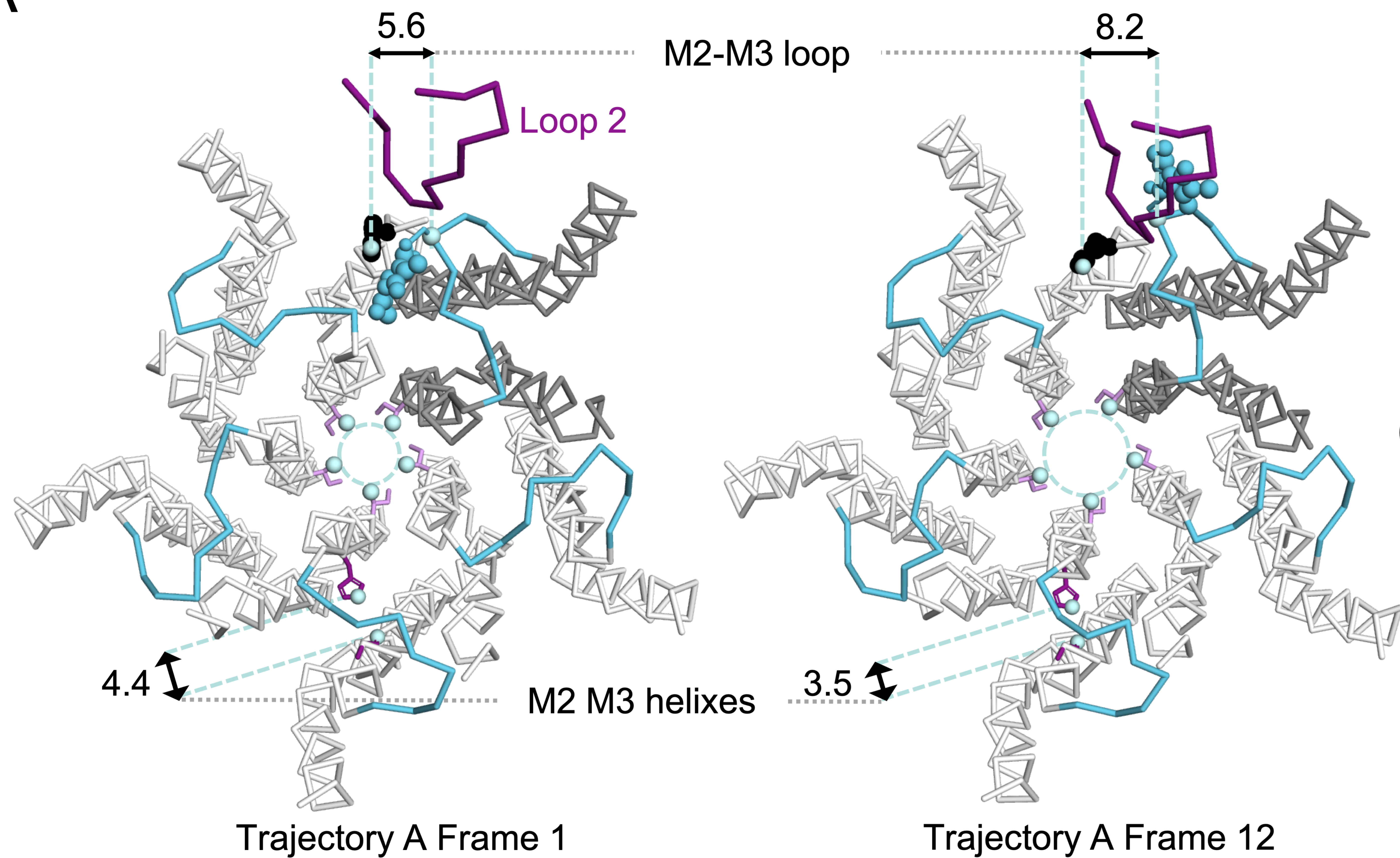
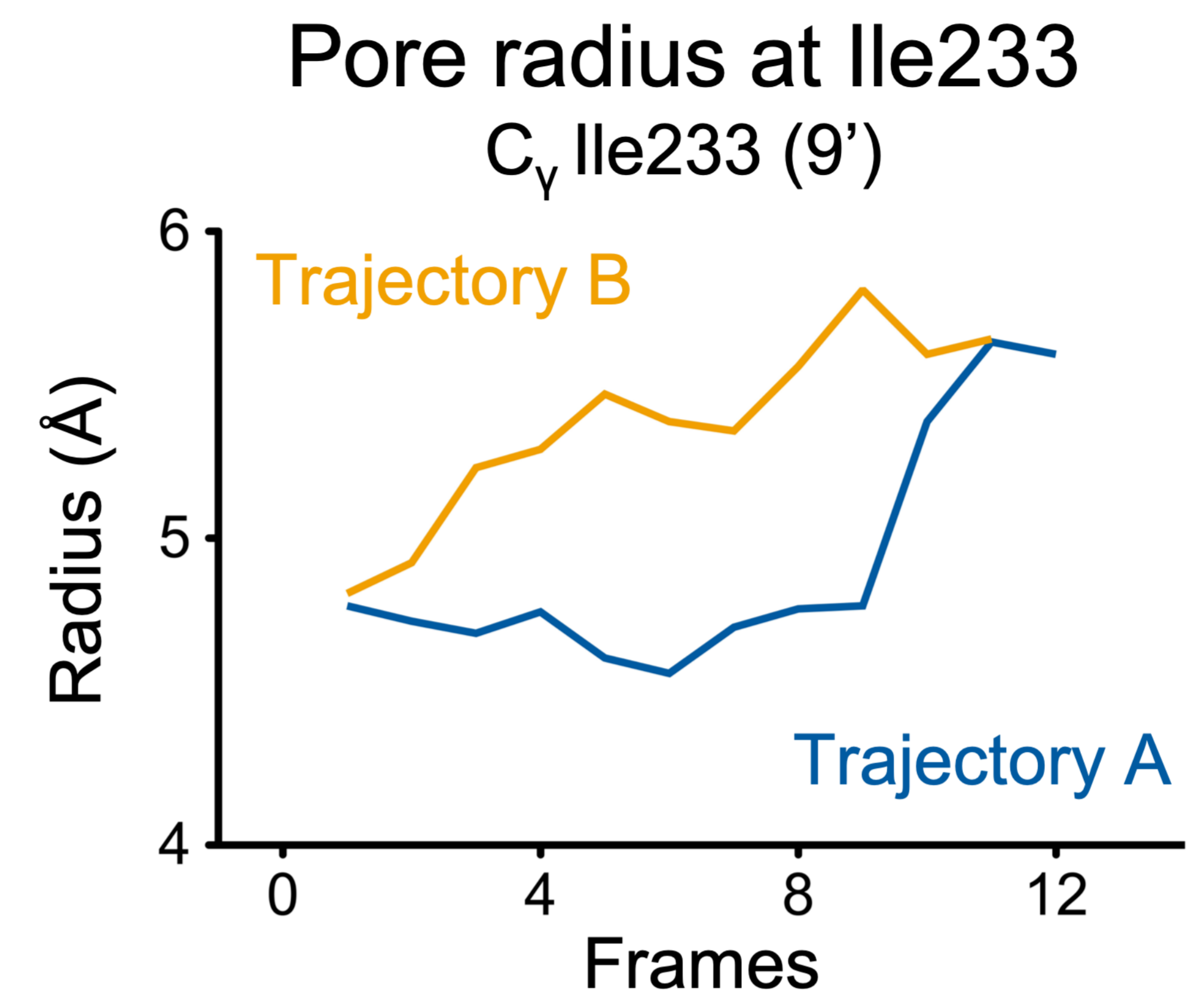
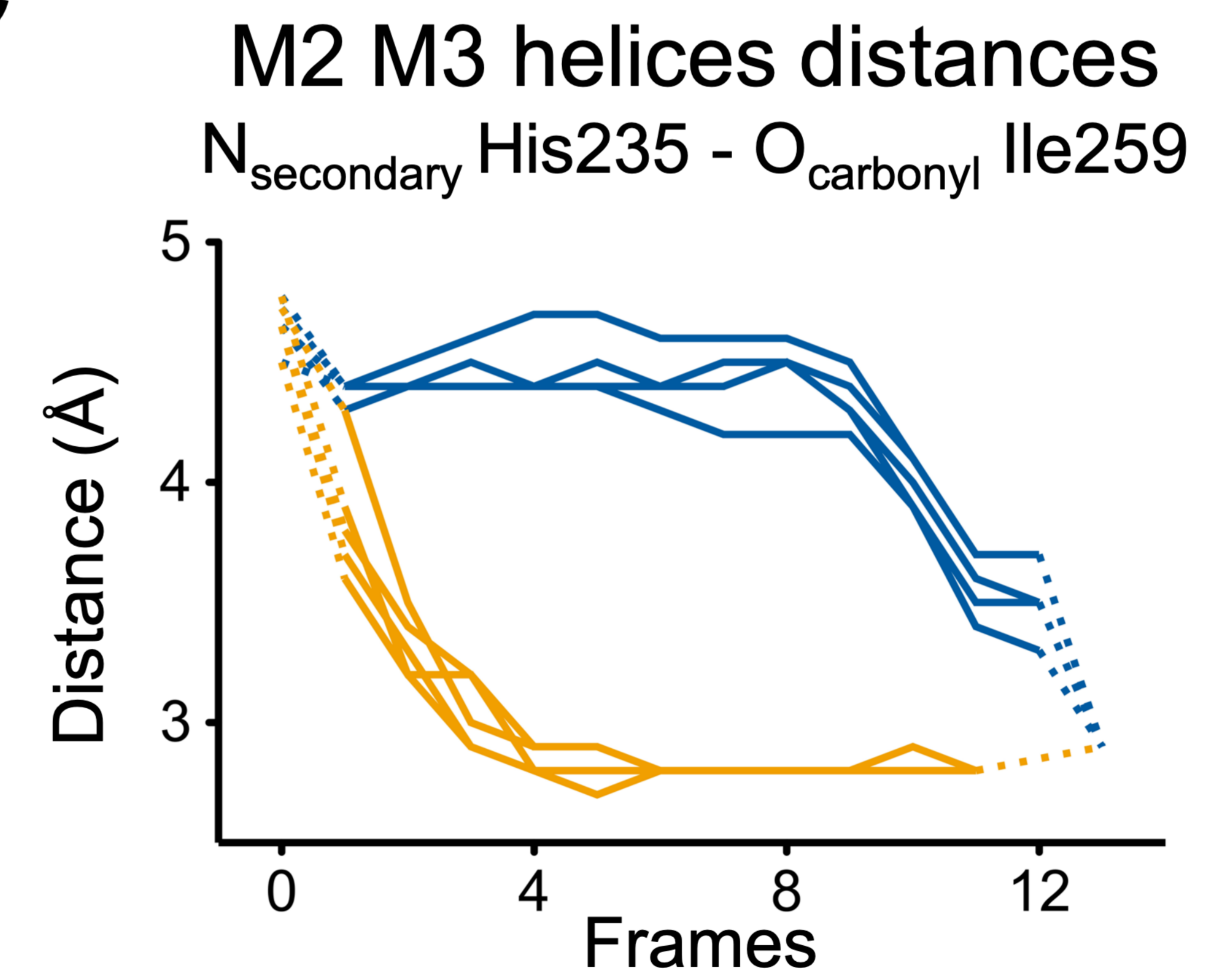
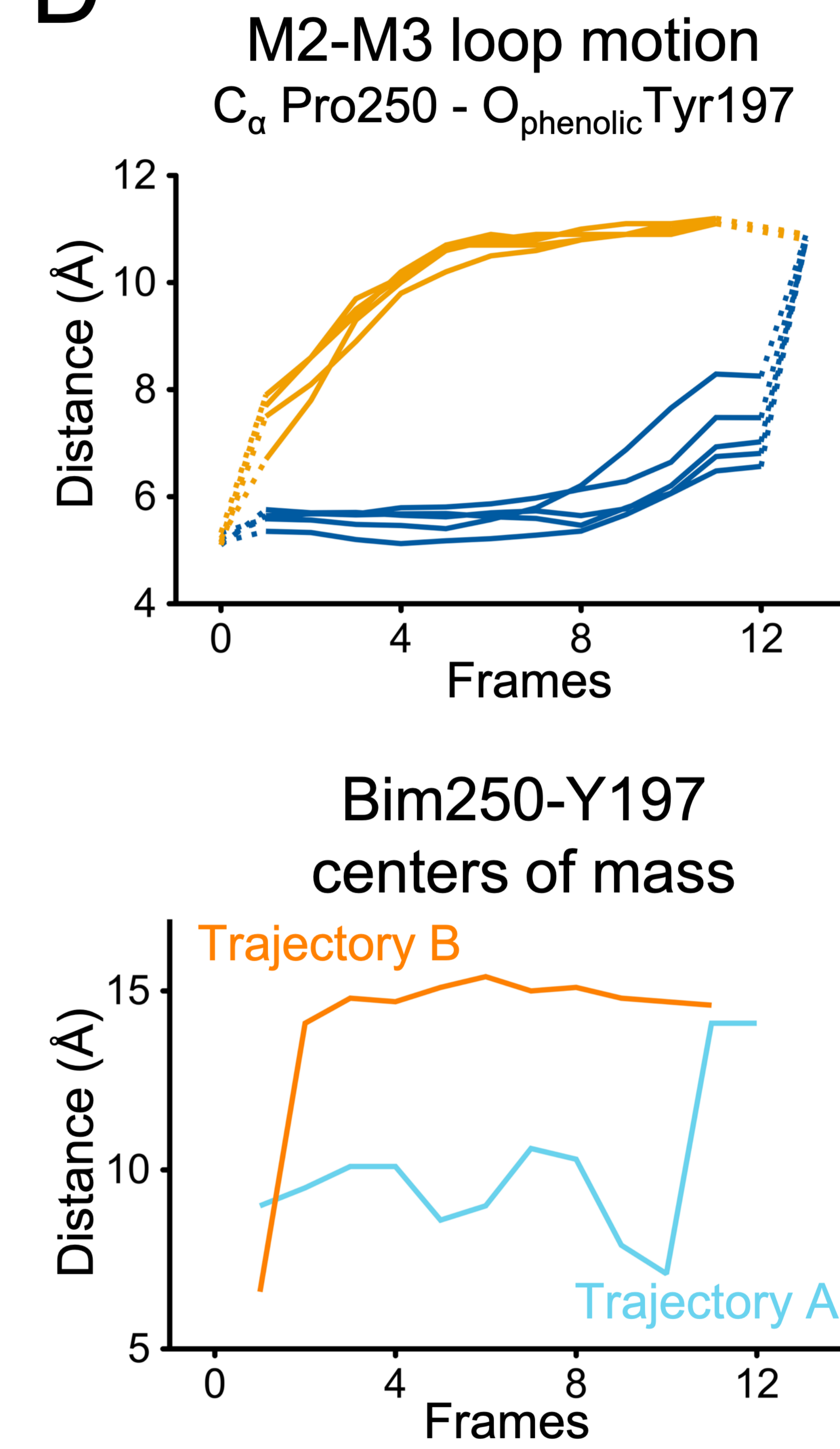


Figure 7

A**B****Figure 8**

A**B****C****D****Figure 9**

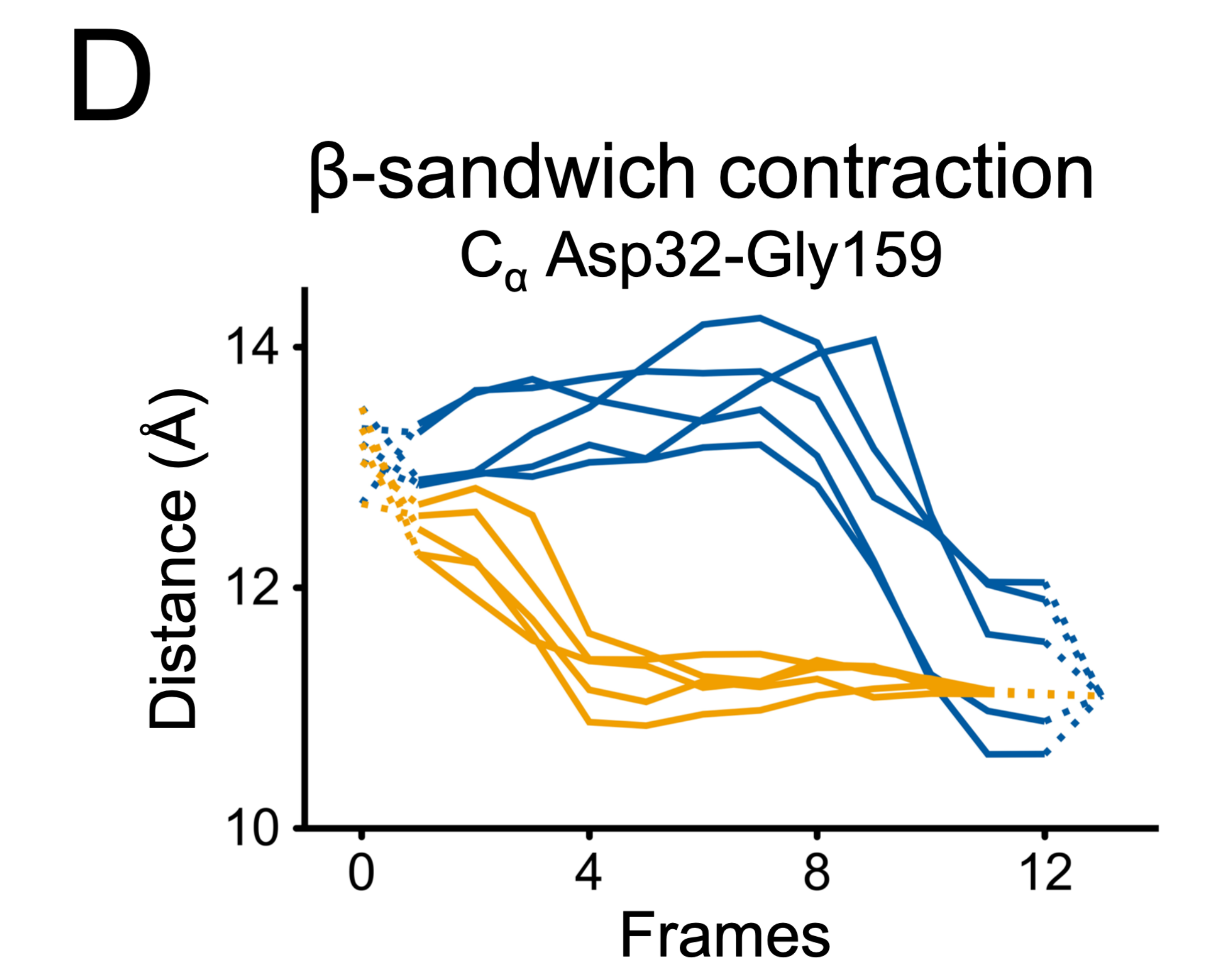
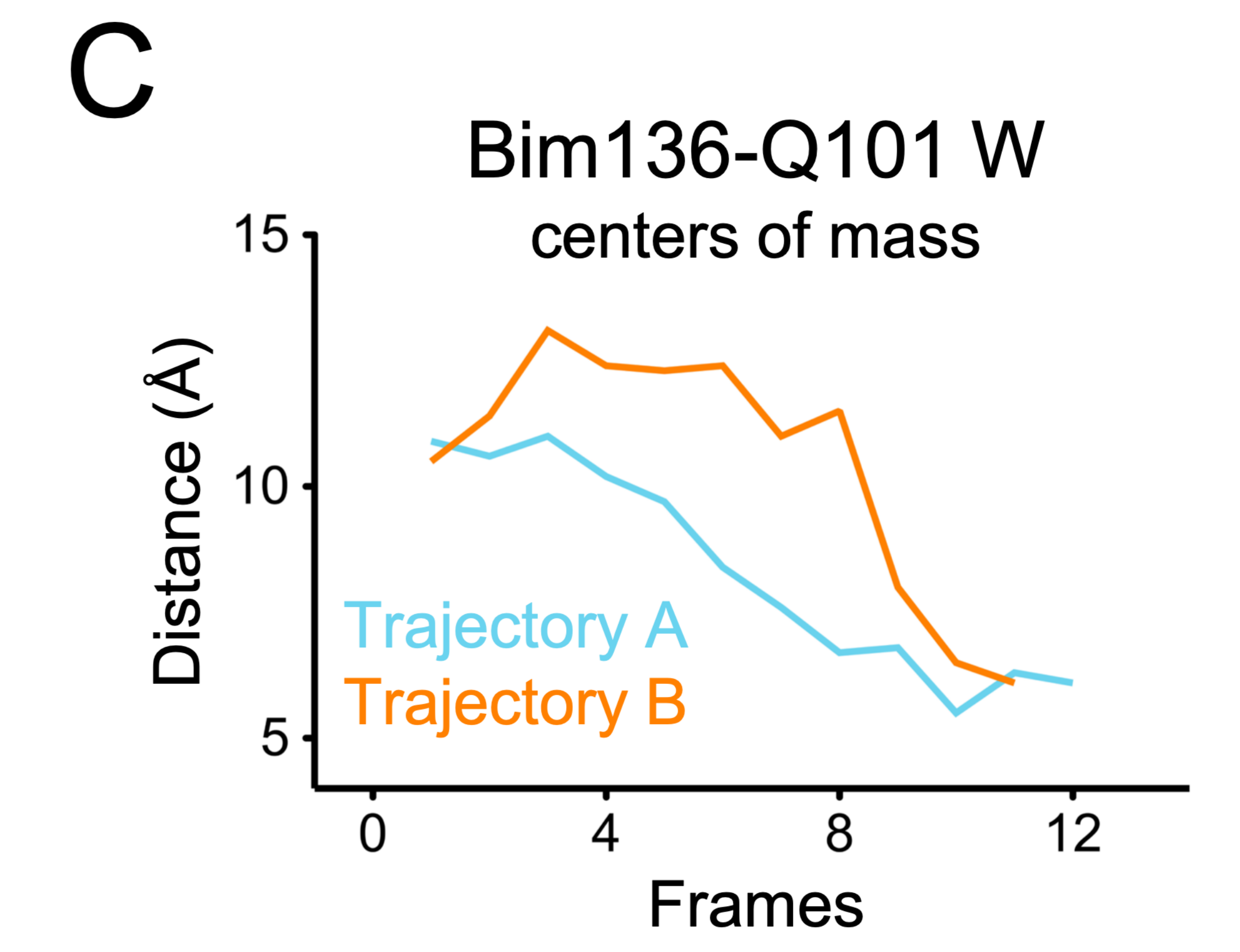
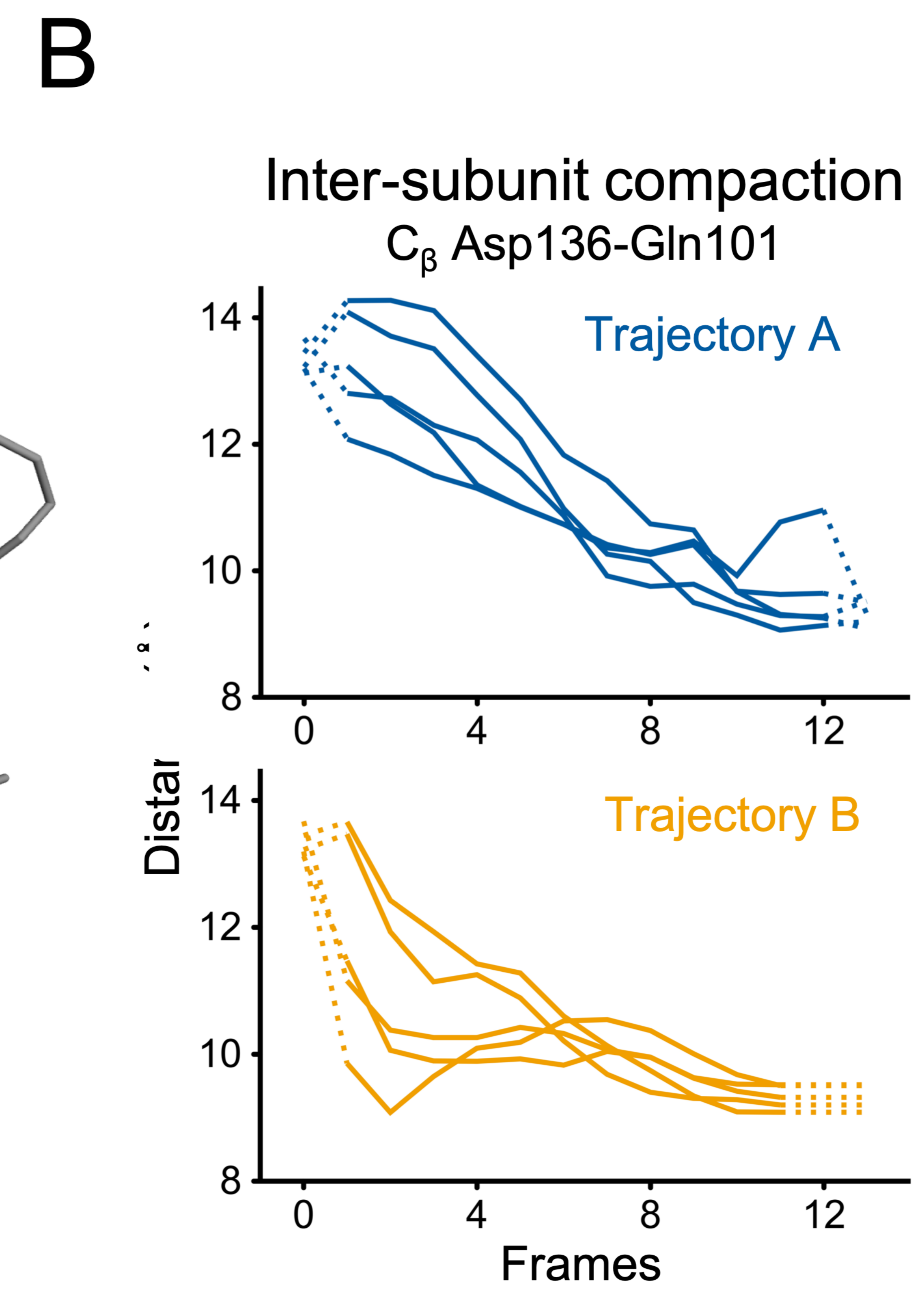
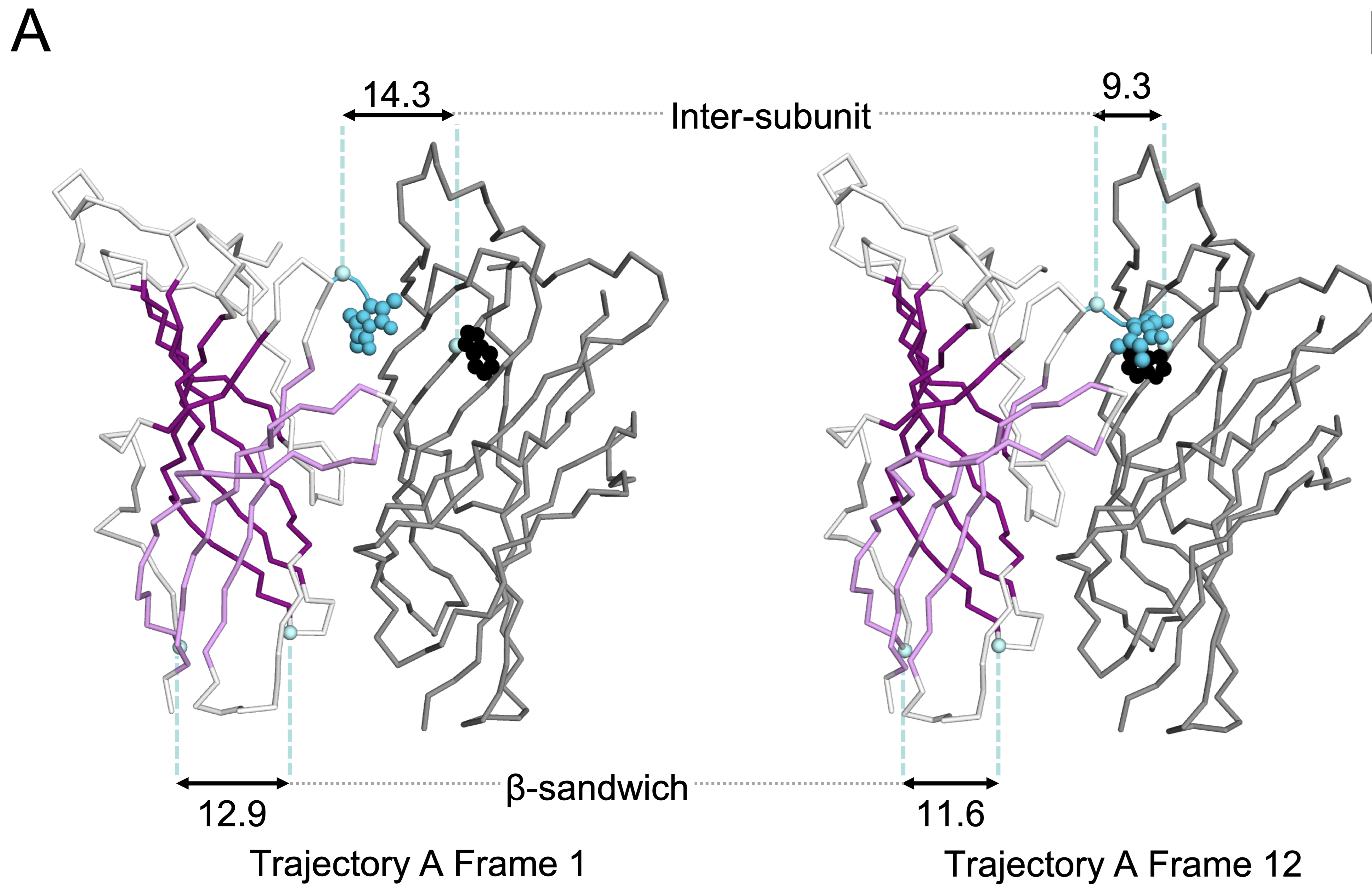


Figure 10

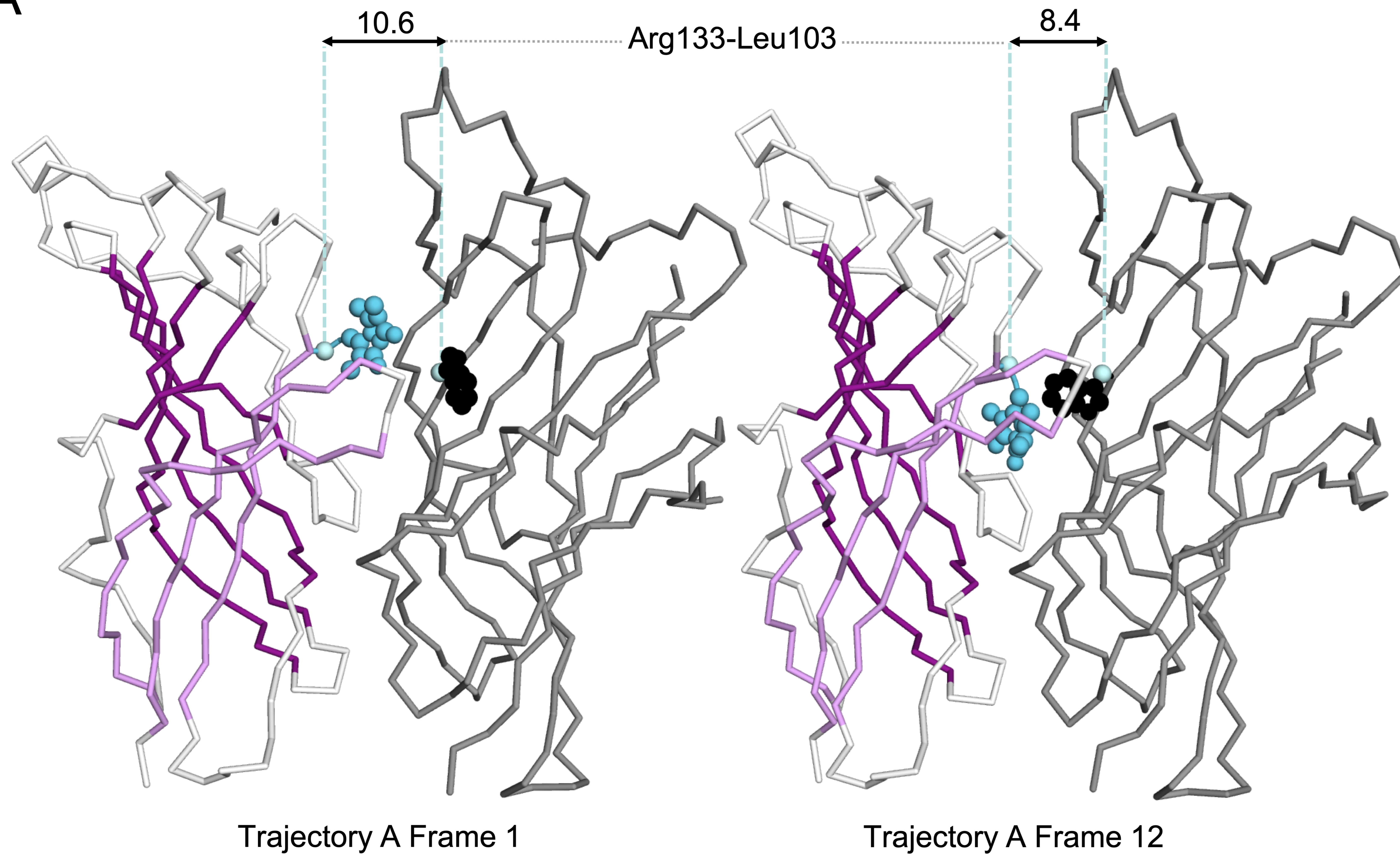
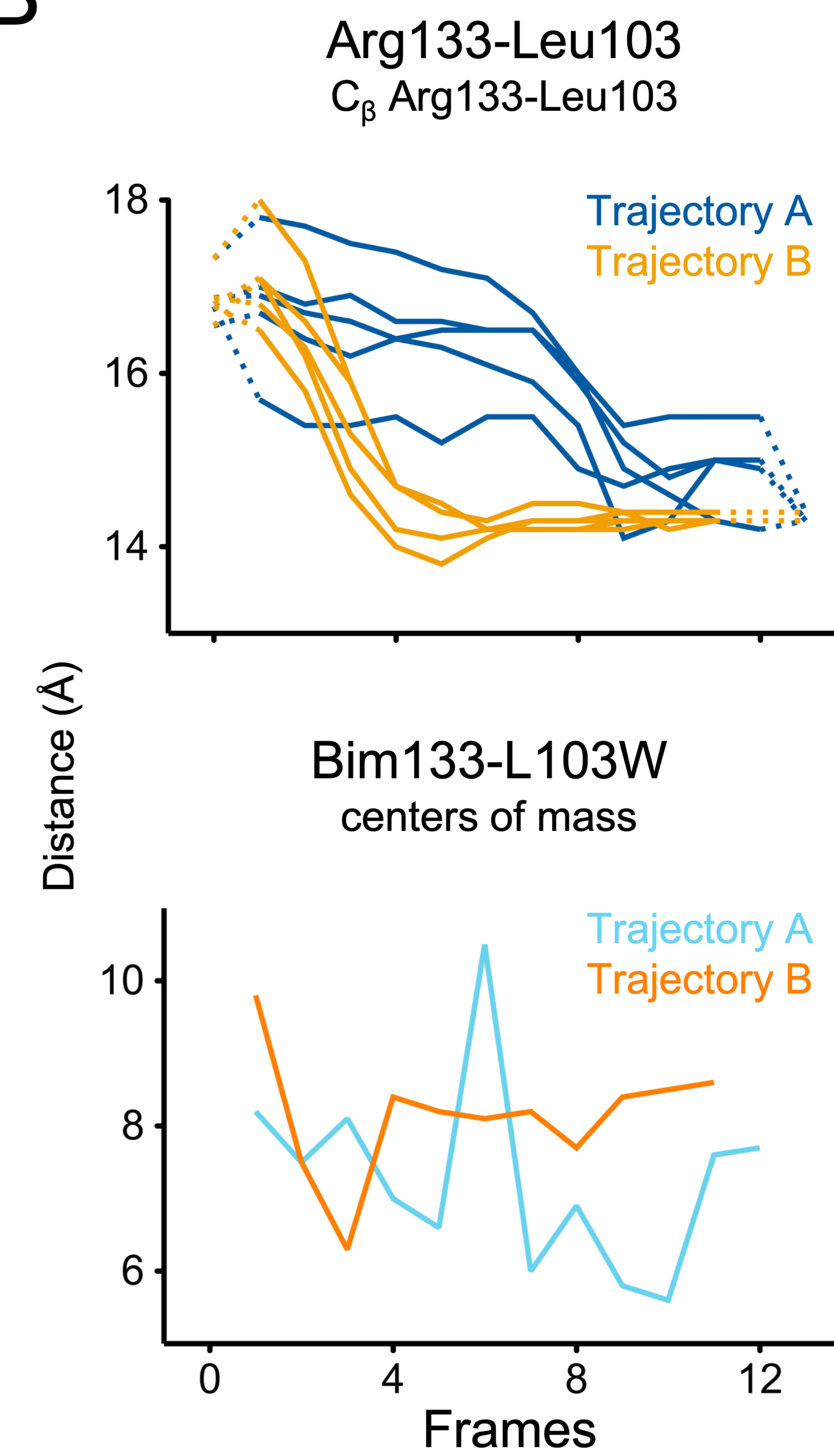
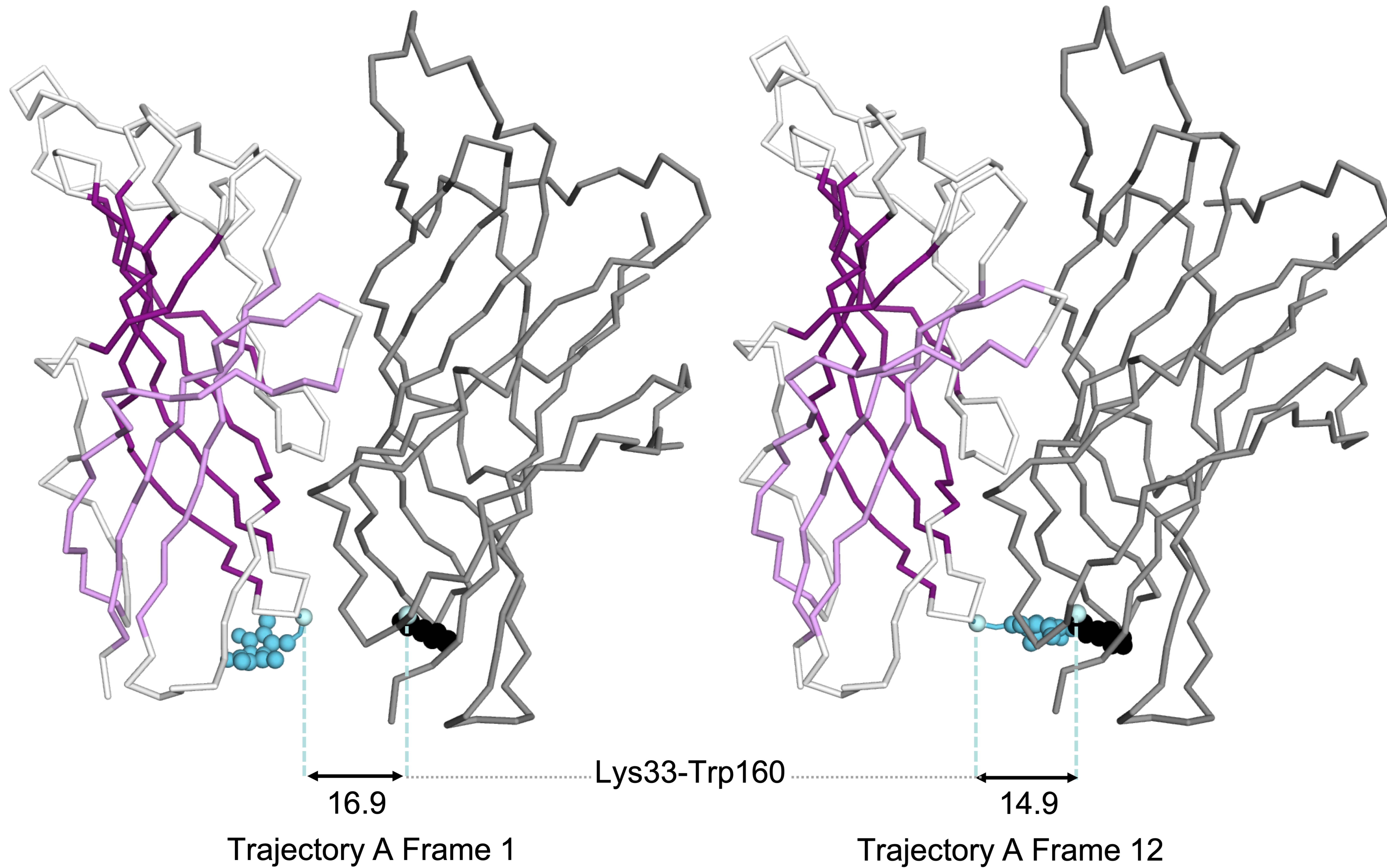
A**B**

Figure 10 – Supplementary 1

A



B

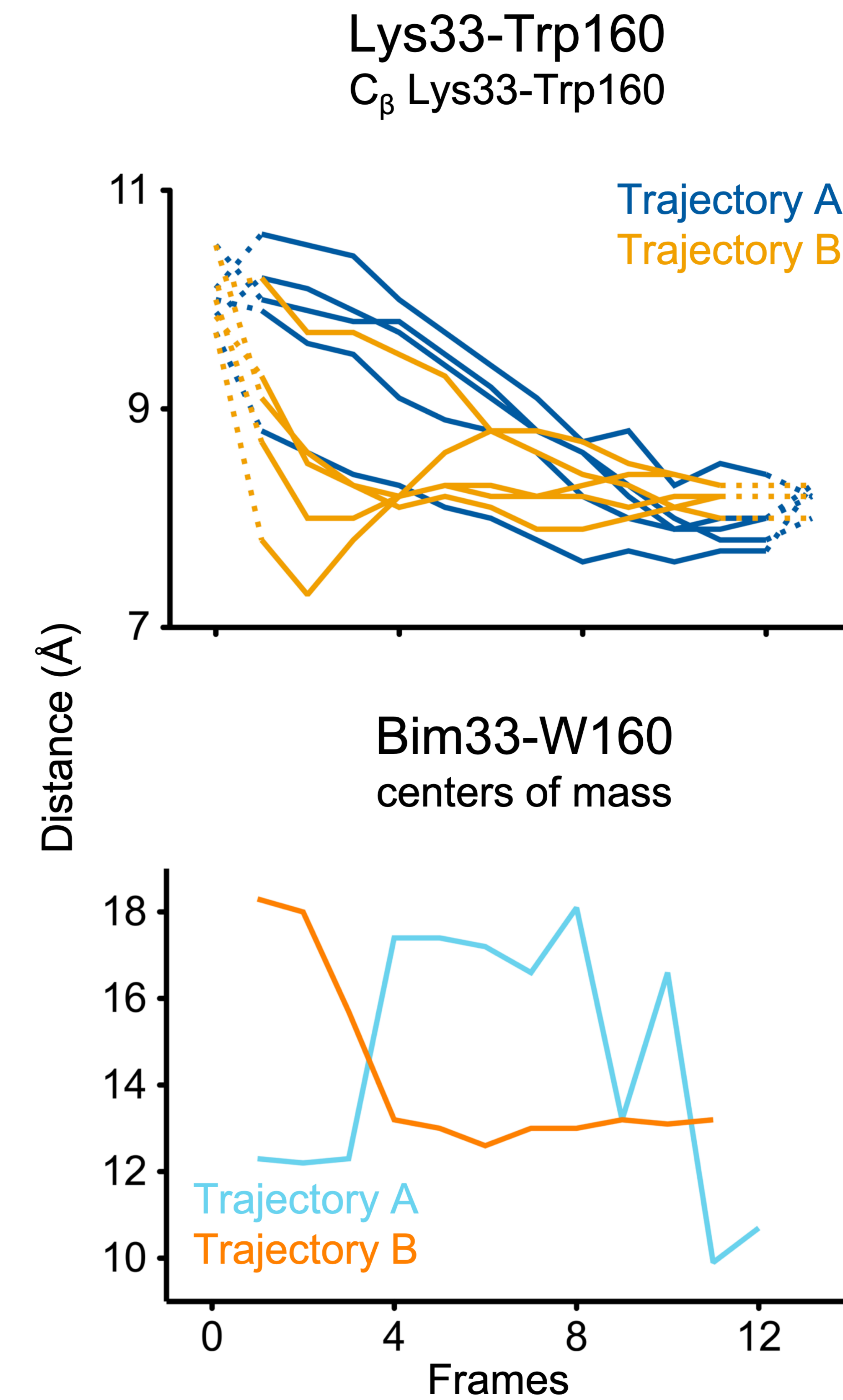


Figure 10 – Supplementary 2

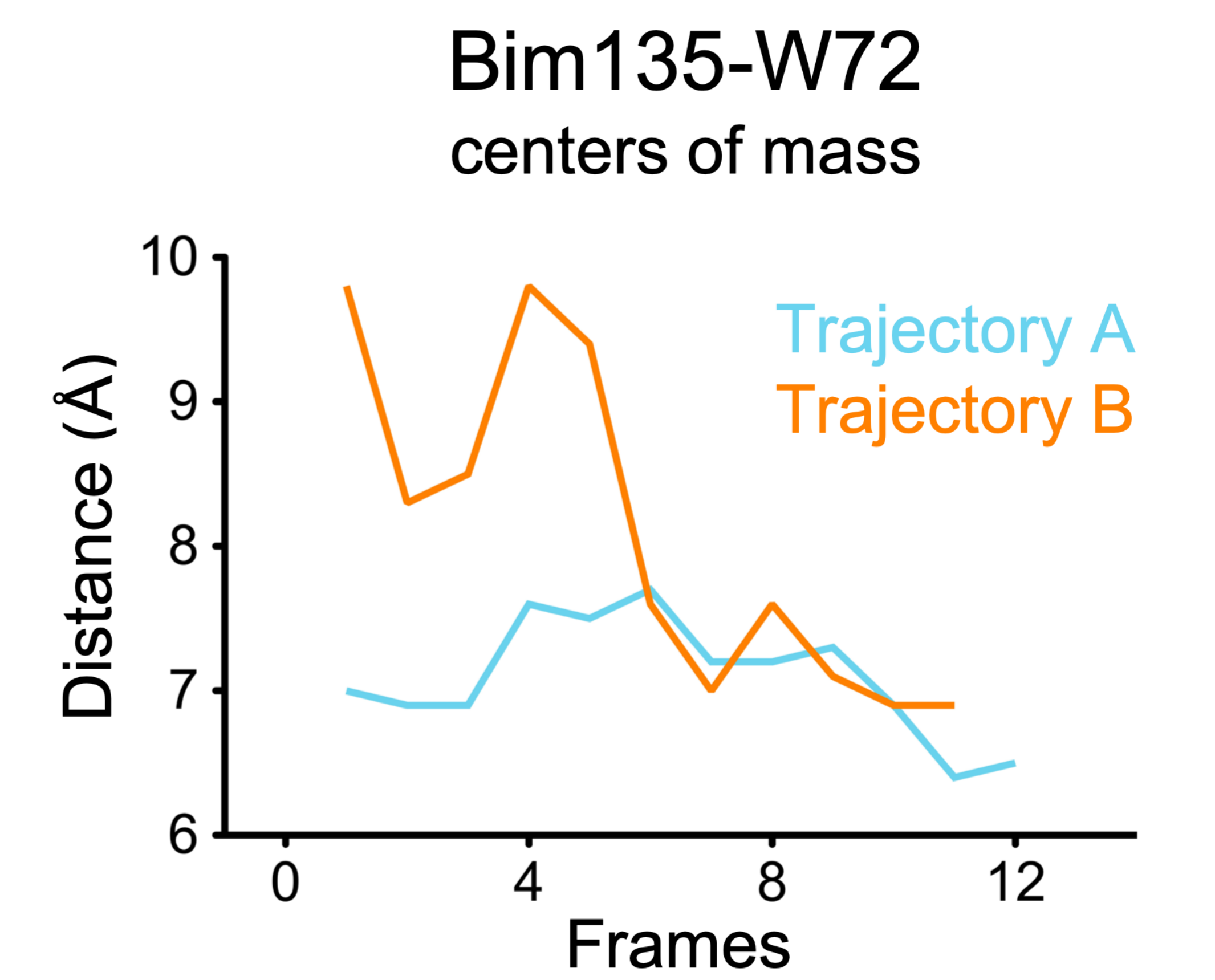
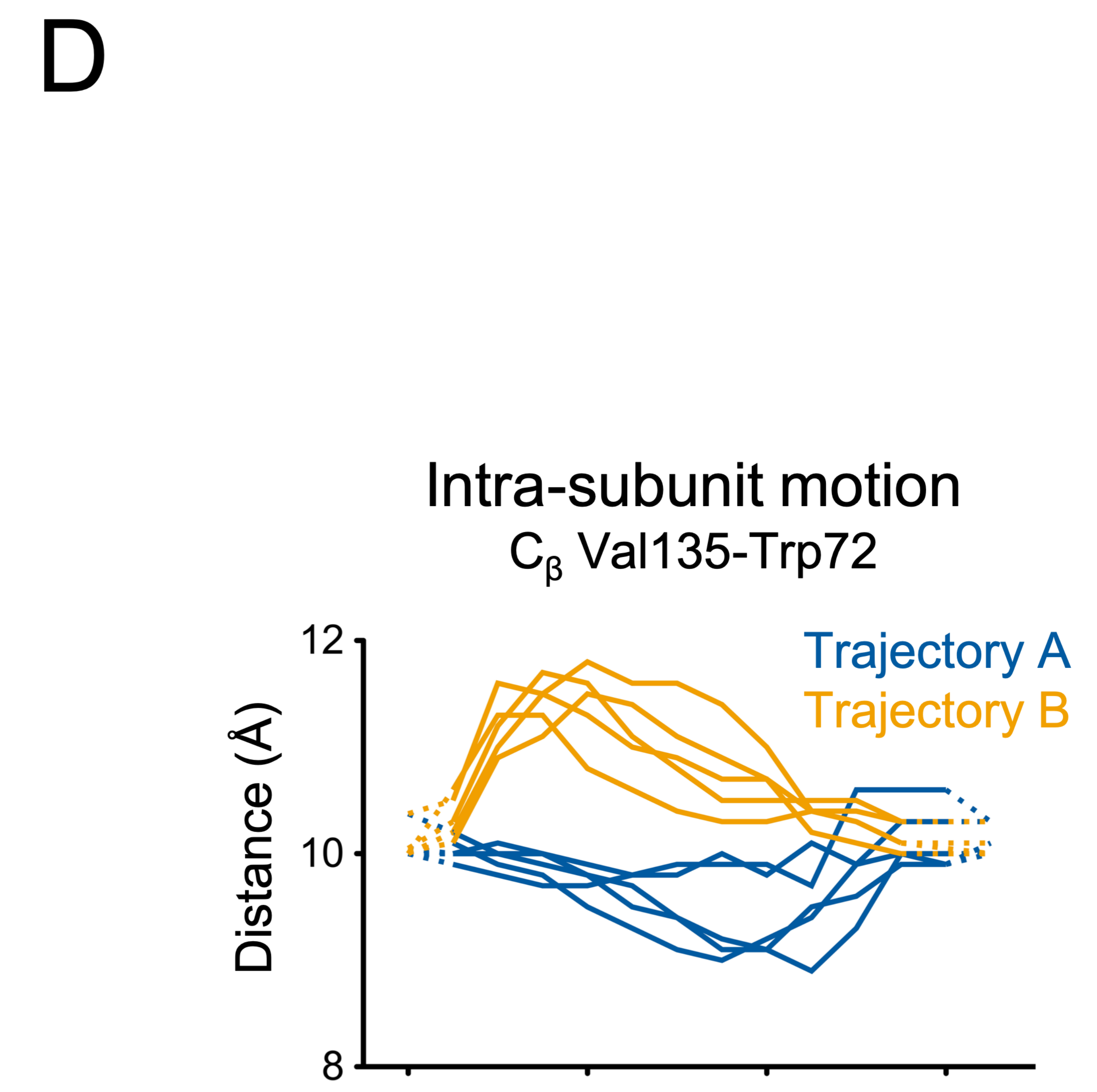
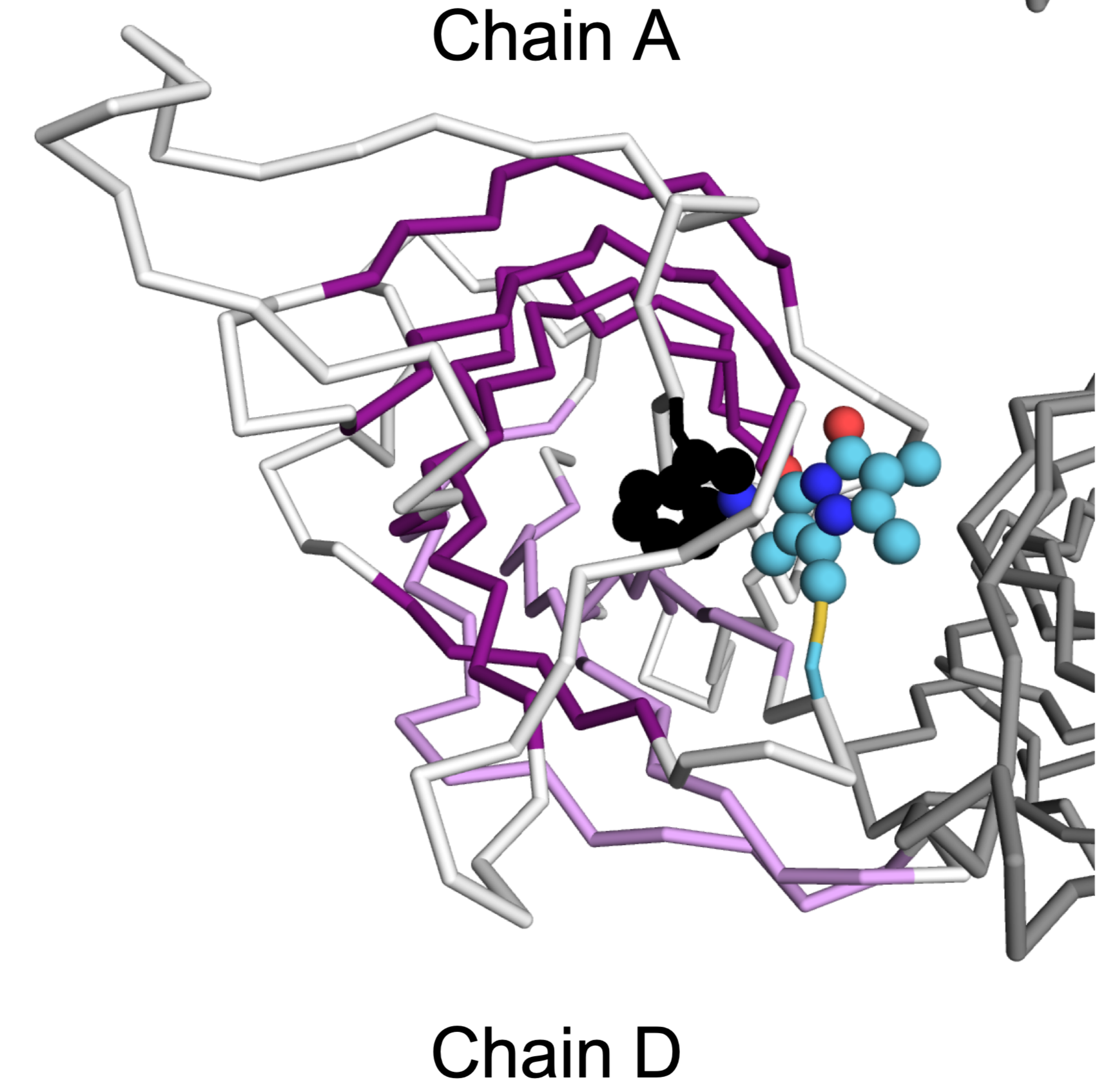
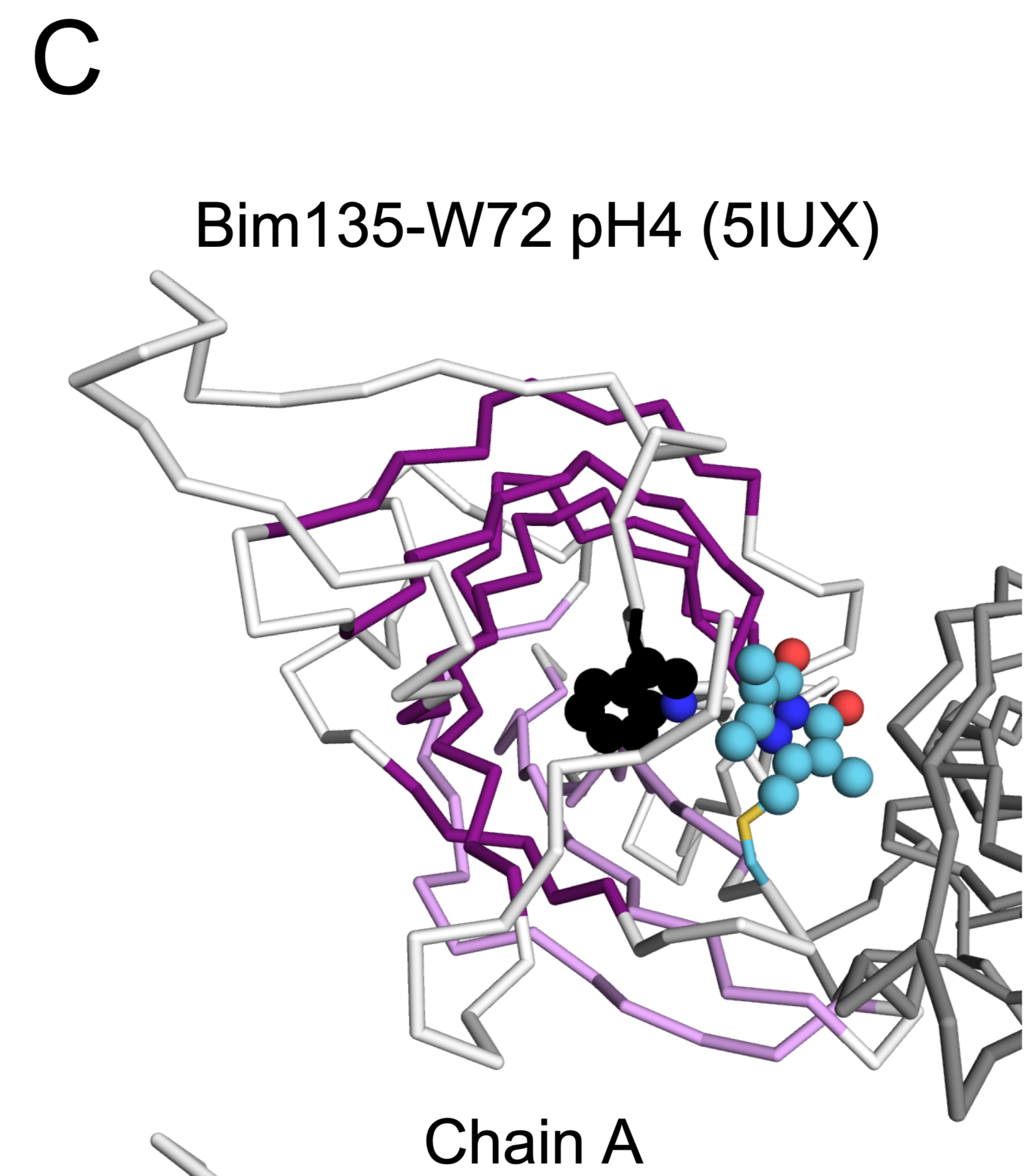
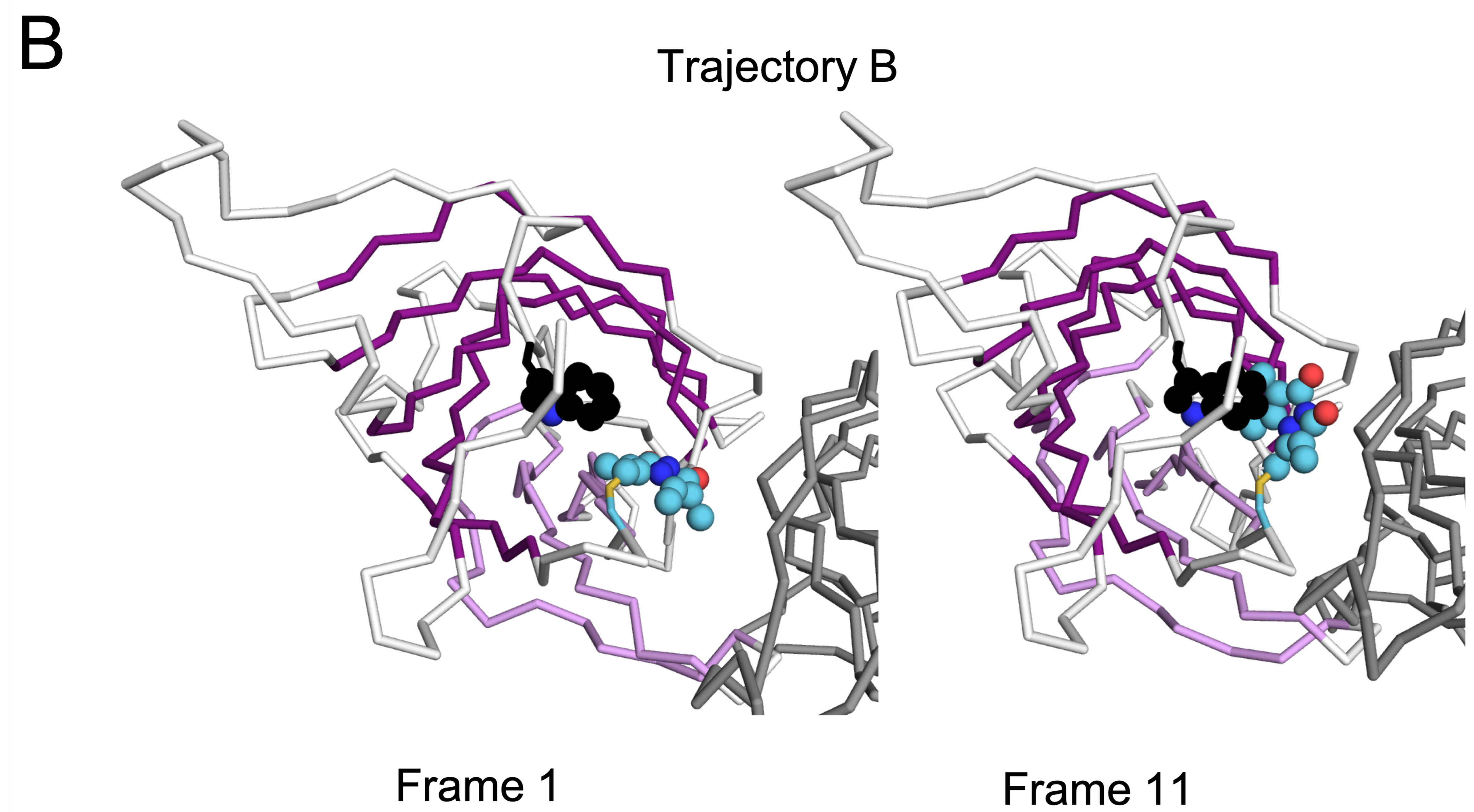
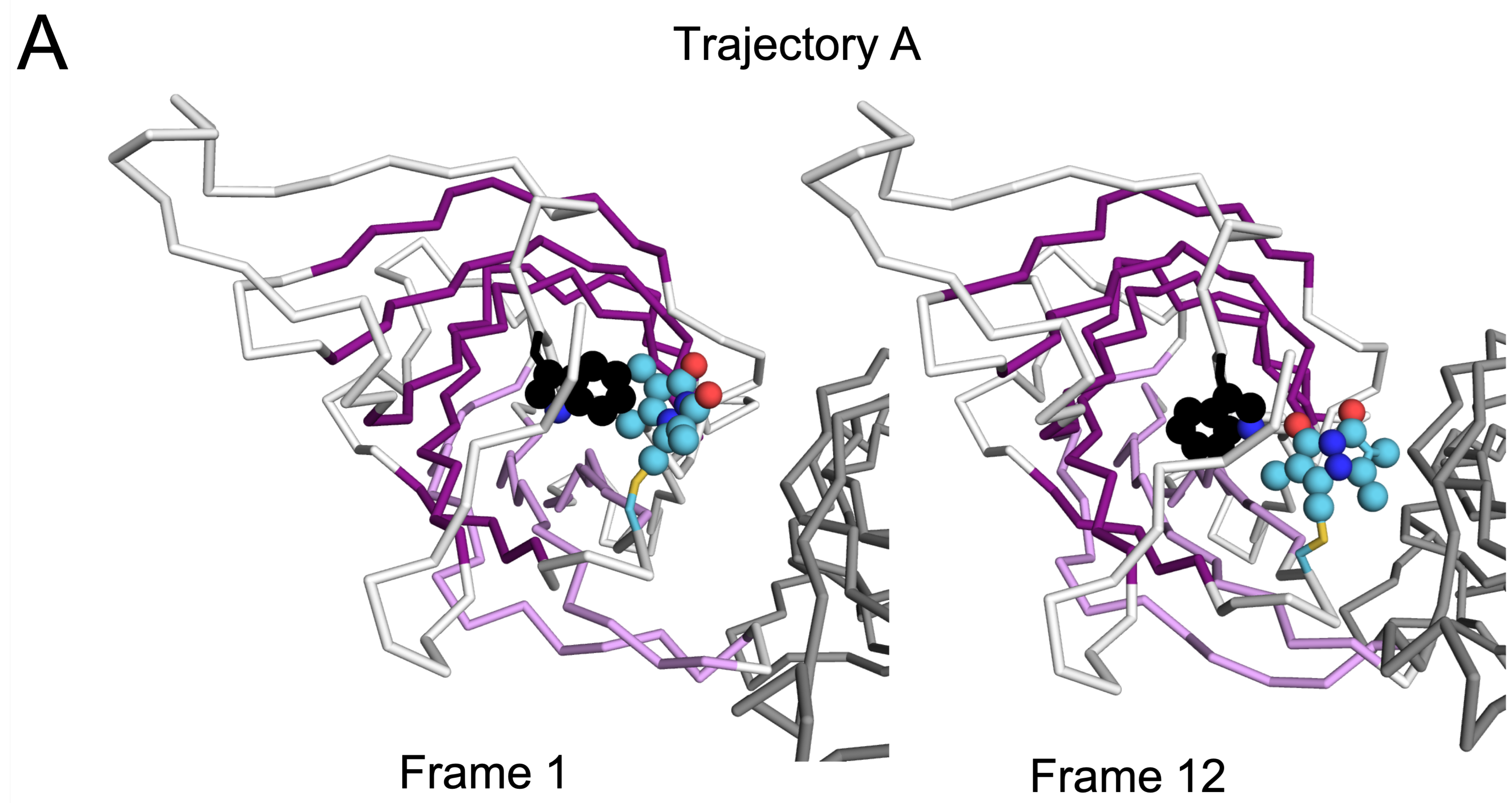


Figure 10 – Supplementary 3

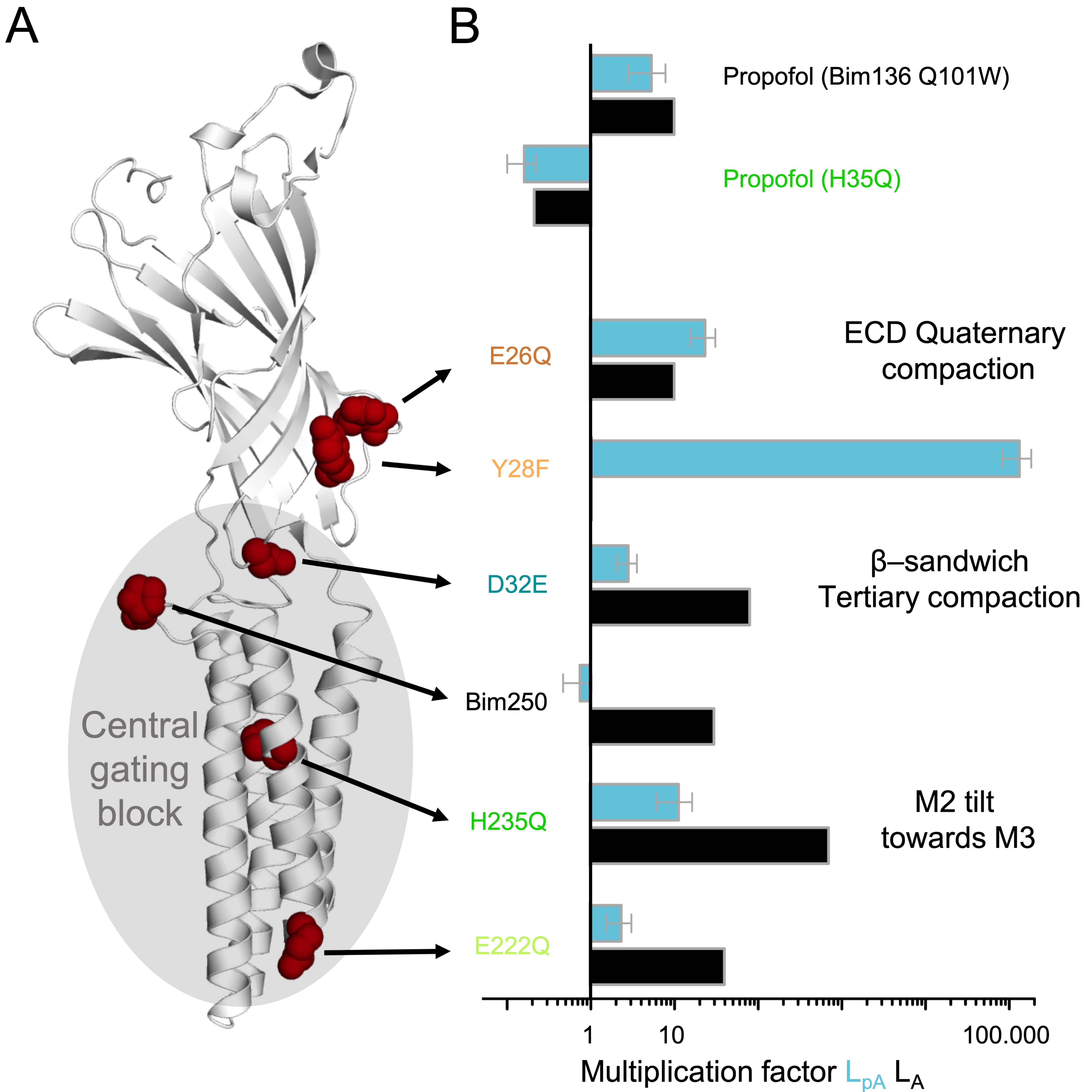


Figure 11